USC
UNIVERSIDADE
DE SANTIAGO
DE COMPOSTELA

INTERNATIONAL DOCTORAL
SCHOOL OF THE USC

Isabel
González Crespo

PhD Thesis

Mathematical models of tumor response in advanced radiotherapy techniques

Santiago de Compostela, 2024

Doctoral Programme in Mathematical Modelling and Numerical Simulation in Engineering and Applied Science

Ph.D. Thesis

MATHEMATICAL MODELS OF TUMOR RESPONSE IN ADVANCED RADIOTHERAPY TECHNIQUES

Isabel González Crespo

Director: Juan Pardo Montero
Director-Tutor: Óscar López Pouso

ESCOLA DE DOUTORAMENTO INTERNACIONAL DA UNIVERSIDADE DE SANTIAGO DE COMPOSTELA

PROGRAMA DE DOUTORAMENTO EN MÉTODOS MATEMÁTICOS E SIMULACIÓN NUMÉRICA EN ENXEÑARÍA E CIENCIAS APLICADAS

SANTIAGO DE COMPOSTELA
2024

Dedications

A meus pais e meu irmán,
por crer sempre en min.

Acknowledgements

En primeiro lugar, quero agradecerlle aos meus directores de tese, Juan e Óscar, a súa guía e consello, o tempo dedicado e a confianza depositada desde que comecei o meu Traballo de Fin de Máster. A Juan, grazas tamén por acompañarme aos congresos, polos cafés de "media mañá" á unha da tarde, e pola paciencia no día a día. Mágoa que non conseguiras que apunte sempre as cousas na libreta. E a Óscar, grazas por ser un gran docente e por achegarme de novo á beleza das formalidades da Matemática.

Grazas a meus pais, Manolo e Marga, por permitirme chegar ata aquí e acompañarme en cada paso; todos os meus logros son tamén vosos. Ao meu irmán, Nico, grazas por estar sempre ao meu lado; espero que te sintas tan orgulloso de min como me sinto eu de ti. Grazas aos meus avós, Faustino, Herminia, Isabel e Manolo, que son un referente de resiliencia e esforzo. En especial á *abuela* Herminia, que se sentou comigo a facer os deberes tantas tardes despois do colexio, grazas por axudarme en todo. Á miña familia ao completo, grazas por apoiarme e desexarme sempre o mellor.

A Ruben, grazas pola comprensión, o apoio e a paciencia inesgotable en cada etapa da tese. O camiño é máis fácil contigo.

Grazas ás miñas amigas, Ana, Isa e Sara, polas risas e os momentos de desconexión; a Susi e Tere, por animarme a seguir desde antes de ser "tres matemáticas"; e a Uxía por escoitarme, estar presente, e mandarme trevos da sorte.

Ás miñas compañeiras e compañeiros do Servizo de Radiofísica e Protección Radiolóxica do CHUS, e ao Grupo de Física Médica e Biomatemáticas do IDIS, grazas por acollerme durante estes anos. En especial a Araceli, Arnau e Julio, polas conversas e os cafés.

Por último, grazas a todas as persoas que formaron parte desta aventura.

November 11, 2024

Additional acknowledgements

The development of this doctoral thesis has been partially funded by FIDIS (*Fundación do Instituto de Investigación Sanitaria de Santiago*) through the "*Predoutorais FIDIS 2021–2024*" call, for which I was awarded a 3-year contract (January 2021–January 2024) within the Medical Physics and Biomathematics Group of IDIS (*Instituto de Investigación Sanitaria de Santiago*).

This work has received financial support from Xunta de Galicia within the project "Optimization and individualization of treatments in advanced radiotherapy techniques" (2022–2026, IN607D2022/02); and the Ministerio de Ciencia e Innovación within the projects "Optimization of the prescription dose and dose/volume limits in the treatment of prostate cancer: an approach from big data" (2023–2025, PID2021), and "Advanced dosimetry for novel radiotherapy approaches in brain tumors (DOSE-BRAIN)" (2022–2025, PLEC2022-009476).

Contents

Derived publications

Presented below is a compendium of publications derived from this thesis:

- I. González-Crespo[1,2], A. Gómez-Caamaño[3], Ó. López Pouso[1,2], J. D. Fenwick[4], and J. Pardo-Montero[1], "A biomathematical model of tumor response to radioimmunotherapy with αPDL1 and αCTLA4," *IEEE/ACM Transactions on Computational Biology and Bioinformatics*, vol. 20, no. 2, pp. 808–21, 2023. DOI: 10.1109/TCBB.2022.3174454.
  Impact factor (JCR 2023): 3.6.
  Category: Mathematics, Interdisciplinary Applications.
  Rank: 16/135 (Q1).
  Contributions: conceptualization, data curation, formal analysis, software implementation, validation, and writing.
  Affiliations:

  [1]Group of Medical Physics and Biomathematics (IDIS)

  [2]Department of Applied Mathematics (USC).

  [3]Department of Radiation Oncology (CHUS).

  [4]Department of Molecular and Clinical Cancer Medicine, Institute of Translational Medicine, University of Liverpool.

  The contents of this article are partially reproduced in Chapter 3.

- I. González-Crespo[1,2], F. Gómez[3], Ó. López Pouso[1,2], and J. Pardo-Montero[1,4], "An in-silico study of conventional and FLASH radiotherapy iso-effectiveness: potential impact of radiolytic oxygen depletion on tumor growth curves and tumor control probability," *Physics in Medicine & Biology*, vol. 69, p. 215016, 2024. DOI: 10.1088/1361-6560/ad8291.
  Impact factor (JCR 2023*): 3.3.
  Category: Radiology, Nuclear Medicine & Medical Imaging.
  Rank: 42/204 (Q1).

Contributions: conceptualization, data curation, formal analysis, software implementation, validation, and writing.

Affiliations:

[1]Group of Medical Physics and Biomathematics (IDIS)

[2]Department of Applied Mathematics (USC).

[3]Department of Particle Physics (USC).

[4]Department of Medical Physics (CHUS).

The contents of this article are partially reproduced in Chapter 4.

*2024 data was not available at the date of finalization of this document.

Resumo

O termo cancro comprende máis de duascentas enfermidades xenéticas distintas, caracterizadas pola aparición de células anormais que se multiplican de maneira incontrolada, levando na maioría dos casos á formación de tumores sólidos. Ademais, poden diseminarse nos tecidos circundantes e chegar a zonas distantes do organismo derivando en tumores metastáticos.

Actualmente, a radioterapia é a técnica máis empregada no tratamento do cancro (en arredor do 60 % dos pacientes segundo a OMS), ben sexa como monoterapia ou en combinación con outras técnicas, tales como a quimioterapia e a cirurxía. Este tratamento consiste en depositar altas doses de radiación sobre o tumor para eliminalo ou minguar a progresión da enfermidade. A radiación causa modificacións no ADN celular derivando en danos letais, que causan a morte directa da célula, ou subletais, que no caso de non ser reparados poden acumularse coa aplicación de fraccións de dose sucesivas levando á morte da célula. Por outra banda, a radioterapia tamén afecta a outros axentes que forman parte do tecido tumoral, como o sistema vascular ou as células do sistema inmune, derivando en mecanismos de morte indirecta.

Desde o desenvolvemento dos primeiros tratamentos de radioterapia a principios do século XX, os numerosos estudos realizados e os sucesivos avances tecnolóxicos permitiron desenvolver tratamentos máis efectivos ao mesmo tempo que reducir os efectos secundarios prexudiciais para os pacientes. Observouse que as células tumorais son máis sensibles ao efecto da radiación que as células normais, xa que a súa taxa de multiplicación acelerada fainas máis susceptibles de recibir dano no seu ADN. Ademais, as células tumorais son menos eficaces á hora de reparar o dano provocado pola radiación debido ás mutacións que sofren. Isto levou ao deseño dos tratamentos de radioterapia convencionais, nos cales a dose total pautada (medida en Gy) divídese en fraccións de dose administradas en días consecutivos (habitualmente 30–40 fraccións cunha fracción diaria de 1,8–2 Gy de luns a venres) ata a finalizar o tratamento. Desta maneira as células normais poden reparar parte do dano non letal ocasionado entre fraccións de dose, mentras que a súa acumulación contribúe á eliminación das células tumorais.

Pouco despois da aparición da radioterapia comezaron a desenvolverse modelos matemáticos co obxectivo de predicir o resultado dos tratamentos, investigar o seu

efecto sobre o tecido tumoral e o tecido san, e asistir na planificación da terapia no ámbito clínico. O modelo lineal-cadrático (*Linear-Quadratic*, LQ) formulouse máis de medio século atrás de maneira paralela en varios traballos. Trátase dunha ecuación sinxela que consta dun termo lineal e outro cadrático, e relaciona a dose de radiación recibida coa fracción de supervivencia celular resultante da súa administración. Esta fórmula obtívose de maneira fenomenolóxica mediante o axuste de datos experimentais *in vitro* e serve para estimar o efecto directo da radiación sobre as células. O modelo involucra dous parámetros, un para cada termo da ecuación, que toman valores específicos para cada tumor, e que se relacionan coa sensibilidade das células ao dano letal e subletal, sendo respectivamente α (lineal) e β (cadrático).

A fracción de supervivencia emprégase para obter outras métricas con aplicación clínica, como a probabilidade de control tumoral (*Tumor Control Probability*, TCP), que permite estimar a probabilidade de que un tratamento de radioterapia elimine completamente o tumor; e a probabilidade de complicación no tecido normal (*Normal Tissue Complication Probability*, NTCP), que serve para calcular a probabilidade de que a dose administrada aporte toxicidade nos tecidos sans.

Un factor que inflúe na supervivencia celular á radioterapia é o estado de osixenación das células. É sabido que os baixos niveis de osixenación (*hipoxia*) están asociados a unha maior resistencia ao dano por radiación. Isto débese tanto a factores biolóxicos como fisicoquímicos. Por un lado, as células hipóxicas empregan certas proteínas chamadas factores inducibles por hipoxia (*Hypoxia Inducible Factors*, HIFs) para promover a súa proliferación. As células tumorais benefícianse deste mecanismo para potenciar a súa progresión. Por outro lado, a presenza de osíxeno ten un papel clave na eliminación das células tumorais, xa que promove a formación de especies reactivas que danan o ADN celular. Polo tanto, a hipoxia é aceptada como un factor que compromete a efectividade dos tratamentos de radioterapia. Para modelar o papel do osíxeno no resultado dos tratamentos, introduciuse o modelo LQ coas razóns de mellora polo osíxeno (*Oxygen Enhancement Ratios*, OERs), que tende á fórmula clásica do modelo LQ en condicións totalmente óxicas.

De acordo con estudos publicados, a introdución da radioterapia hipofraccionada (menor número de fraccións con maiores doses por fracción, arredor de 8–30 Gy) supuxo unha mellora na calidade de vida dos pacientes, aportando maior control tumoral e menos efectos secundarios no tratamento de determinados tipos de cancro. Numerosos estudos levaron a debate a capacidade do modelo LQ para reproducir o efecto dos tratamentos hipofraccionados, apuntando a un fenómeno de saturación do dano para as altas doses por fracción empregadas, froito da reparación do dano subletal. Xurdiron así o modelo lineal-cadrático-lineal (*Linear-Quadratic-Linear*, LQL) e outras formas derivadas do modelo LQ, que incorporan parámetros adicionais para modular o efecto das altas doses na fracción de supervivencia.

Nas últimas décadas xurdiron novas técnicas de radioterapia avanzada para as cales o modelo LQ e as súas variantes son insuficientes. Os novos tratamentos involucran mecanismos de morte celular indirecta, que non resultan unicamente do dano celular

causado pola radiación. É necesario incorporar no modelo o efecto da terapia sobre outros axentes presentes no microambiente tumoral, como as células do sistema inmune, e outros factores que alteran o resultado do tratamento, como os cambios na osixenación durante a súa administración.

Nesta tese preséntanse novos modelos de resposta tumoral a técnicas avanzadas de radioterapia. Por un lado, para o uso combinado de radioterapia e inmunoterapia, coñecido como radioinmunoterapia. Por outro lado, para a radioterapia FLASH, que consiste en empregar taxas de dose máis altas permitindo a administración de maiores doses de radiación en menos tempo de tratamento. Os modelos presentados constrúense tomando como referencia os modelos clásicos mencionados anteriormente.

A inmunoterapia é unha técnica que consiste en potenciar o efecto antitumoral do propio sistema inmunitario do paciente interferindo nalgunha das fases do chamado ciclo inmune do cancro. Este ciclo consta de distintas fases mediante as cales a presenza de axentes nocivos no organismo, como as células tumorais, dá lugar á liberación de sinais específicos (antíxenos) que activan as células T do sistema inmune, encargadas de recoñecer e eliminar o axente contra o cal foron especializadas. O organismo conta con puntos de control inmunitario para evitar unha resposta inmune excesiva, que podería derivar en enfermidades inflamatorias. As células do cancro benefícianse destes mecanismos para evitar a morte inmune manifestando inhibidores dos puntos de control.

O receptor CTLA-4 é un mecanismo de control que interfire na fase de activación das células T. Para a correcta especialización e activación das células T, o ligando CD28, presente na súa superficie, debe unirse co CD80 ou CD86 na superficie das células encargadas de transportar e presentar os antíxenos. Pola contra, co fin de evitar unha sobreactivación, o CD28 pode unirse co receptor CTLA-4 dando lugar a unha célula T inactiva. Para potenciar a activación, desenvolveuse a inmunoterapia con anticorpos inhibidores do CTLA-4 (anti-CTLA4). Nesta terapia, o anticorpo adminístrase de maneira intravenosa e únese co receptor CTLA-4 favorecendo a unión dos ligandos que levan á activación das células T.

O eixe PD-1/PD-L1 constitúe outro punto de control e afecta á identificación das células tumorais por parte das células T xa activadas. O PD-1 é unha proteína que está presente na superficie das células T, e o seu ligando, o PD-L1, maniféstase noutros axentes do microentorno tumoral. Cando estes dous ligandos se unen, a célula T "desactívase". As células tumorais son capaces de manifestar PD-L1 na súa superficie e escapar da acción das células T. As inmunoterapias inhibidoras do PD-1 e o PD-L1 (anti-PD(L)1) adminístranse tamén de maneira intravenosa co obxectivo de favorecer a actividade inmune.

Os primeiros fármacos de inmunoterapia anti-CTLA4 e anti-PD1 aprobáronse para o seu uso clínico nos anos 2011 e 2014, respectivamente. Malia resultar beneficiosos no tratamento do cancro, ofrecen unha mellora limitada en gran parte dos pacientes, xa que a súa efectividade depende do bo funcionamento do propio sistema inmune. Por este motivo, adóitase usar en combinación con outras técnicas como a radiotera-

pia, dando lugar á radioinmunoterapia. Ademais, o uso de radiación dá lugar tanto a efectos inmunosupresivos como inmunoxénicos. Por un lado, dana as células inmunes presentes no tumor, limitando a súa acción. Por outro lado, incrementa a liberación de antíxenos, promovendo unha maior activación de células T. Numerosos estudos experimentais apuntan a que a radioinmunoterapia leva a maiores taxas de control tumoral en comparación co uso das dúas técnicas de maneira independente. Na actualidade, esta técnica combinada continúa sendo investigada de cara a deseñar tratamentos óptimos onde se atope a combinación de ambas terapias que aporte maior beneficio aos pacientes.

O modelo de radioinmunoterapia proposto nesta tese é de tipo mecanicista e compartimental. Describe a dinámica dos principais axentes involucrados na resposta á radioinmunoterapia seguindo o ciclo inmune do cancro: células tumorais non danadas pola radiación ou viables, células tumorais danadas que serán eliminadas, células T activas e antíxenos (ou células presentadoras do antíxeno). Ademais incorpora un submodelo de activación no que participan os antíxenos, as células inmunitarias dispoñibles para ser activadas, as células T activas e as células T bloqueadas polo efecto do PD-1/PD-L1. Este modelo está formado por ecuacións diferenciais ordinarias, con retardos e con impulsos. Aínda que se trata dun modelo compartimental, tense en conta a compoñente espacial de maneira indirecta mediante a distinción de dúas localizacións do organismo que levan a incluír retardos temporais na dinámica das variables consideradas. Por un lado, a liberación de antíxenos, a morte inmune, e o efecto da radioterapia e a inmunoterapia con anti-PD(L)1 ocorren no tumor. Por outro lado, a activación das células T e o efecto da inmunoterapia con anti-CTLA4 dáse nos órganos linfoides. Polo tanto, as ecuacións con retardo empréganse para ter en conta o desprazamento dos antíxenos desde o tumor ata os órganos linfoides, así como das células T activadas facendo o percorrido inverso.

En canto ao efecto dos tratamentos, introdúcense no modelo mediante impulsos nos tempos de administración. Por un lado, a radioterapia modélase mediante o cálculo da fracción de supervivencia. Nos instantes de tratamento, a poboación de células tumorais viables (que aumenta seguindo unha forma loxística para simular a súa multiplicación) vese reducida a unha fracción da mesma, que pasa a formar parte do compartimento de células danadas para ser eliminada progresivamente cunha taxa de morte exponencial. Ao mesmo tempo, considérase que unha certa fracción das células T activas no tumor é eliminada de maneira instantánea. No cálculo da fracción de supervivencia investigáronse tres modelos: o LQ, o LQL e unha variante do LQ. Ademais, estudouse o efecto inmunosupresor da radiación que xorde ao danar a vasculatura tumoral limitando o acceso das células T á zona. Para isto, empregouse un factor modulador no compartimento de células T activas que chegan ao tumor. Por outro lado, a inmunoterapia modélase incluíndo dúas variables máis que describen a concentración dos fármacos anti-CTLA4 e anti-PD(L)1, respectivamente, con taxas de eliminación exponenciais. Estas variables modulan os termos de activación das células T ou da morte inmune das células tumorais.

O modelo de resposta presentado validouse co axuste de datos preclínicos procedentes de dous traballos experimentais publicados. Neles comparouse a evolución de volumes tumorais en poboacións de ratos para distintos grupos: grupo control en ausencia de tratamento, só radioterapia, só inmunoterapia con anti-PDL1 ou anti-CTLA4, e tratamento combinado de radioinmunoterapia co respectivo anticorpo. Para obter os valores dos parámetros do modelo que axustan as medias poboacionais dos distintos grupos, empregouse un algoritmo de optimización (*Simulated Annealing*). Posteriormente, tomando como referencia os valores dos parámetros obtidos do axuste dos volumes preclínicos, leváronse a cabo estudos sobre o calendario de administración da radioimmunoterapia con anti-CTLA4 que maximiza a probabilidade de control tumoral. Nun primeiro estudo fixáronse os días de administración da radioterapia e variáronse os da inmunoterapia. Noutro segundo estudo, fixáronse os días de administración da inmunoterapia e variouse o número de fraccións de dose de radioterapia. Os resultados desta investigación, en liña cos dos traballos experimentais, apuntan a que administrar a inmunoterapia dous días despois de comezar coa radioterapia proporciona maiores taxas de control que comezar o mesmo día ou retrasala catro días, sendo a última a que aporta peores resultados. Con base no estudo realizado, hipotetízase que os retardos temporais asociados aos desprazamentos de antíxenos e células T activas pode ter relevancia á hora de deseñar os tratamentos. Espaciar o inicio da inmunoterapia con respecto á radioterapia pode dar lugar a que o número de células T activas no tumor non se manteña e diminúa o seu efecto terapéutico. Por outro lado, obtívose que para o caso de estudo a radioterapia moderadamente hipofraccionada leva a maiores taxas de control tumoral que os tratamentos convencionais ou extremadamente hipofraccionados.

A radioterapia FLASH consiste na administración da radiación con altas taxas de dose, superiores aos 40 Gy s^{-1} en comparación cos 0.05-0.40 Gy s^{-1} da terapia convencional. Esta terapia cobrou importancia nos últimos anos xa que os estudos preclínicos realizados apuntan a que mantén a efectividade da modalidade convencional aportando menos toxicidade aos tecidos sans veciños. Estudos experimentais en solucións acuosas e outros compostos que imitan as células, así como estudos preclínicos *in vivo*, demostraron que a radioterapia FLASH provoca unha diminución de osíxeno durante o tratamento nos medios irradiados, ao contrario que a convencional, onde este efecto non é observable coa tecnoloxía actual. Este fenómeno pode deberse a que o consumo de osíxeno asociado a taxas de doses baixas se compensa coa continua aportación do sistema vascular tumoral, que resulta insuficiente no caso da radioterapia FLASH. Dado que os niveis reducidos de osíxeno aportan maior resistencia ao dano por radiación, é amplamente aceptado que este efecto causa unha diminución da toxicidade do tratamento no tecido san, así como outros factores de tipo inmune ou fisicoquímico. Pola contra, non está claro por que ese efecto protector non se observa no tumor, o cal levaría a unha menor efectividade coa radioterapia FLASH respecto da convencional. Mentres que diversos estudos atribúen este fenómeno a diferenzas entre os tecidos tumoral e san, como na produción de radicais libres, outros suxiren que

o efecto protector no tumor existe pero non ten evidencia significativa nas pequenas mostras experimentais que se adoitan empregar.

Nesta tese investígase a aparente isoefectividade de ambas terapias prestando atención ao papel do osíxeno como elemento diferenciador. Para elo, inicialmente empregouse un modelo de osixenación obtido da literatura para axustar datos de eliminación de osíxeno en distintas solucións e tumores preclínicos. Este modelo consta dunha ecuación en derivadas parciais de reacción-difusión que describe a dinámica do osíxeno no tecido tumoral, incluíndo o sistema vascular como termo fonte, e as células e a radiación como termos de consumo. Para ter en contra a heteroxeneidade que amosan os tumores en canto ás distribucións de osíxeno, os modelos de osixenación resolvéronse sobre un dominio bidimensional que simula o tecido tumoral cunha distribución aleatoria de capilares que simula o seu sistema vascular. Do mesmo traballo obtívose unha expresión para calcular a fracción de supervivencia asociada á radioterapia FLASH baseada no modelo LQ coa modificación dos OERs.

Ademais, deseñouse un modelo que describe a evolución do volume tumoral despois do tratamento partindo das fraccións de supervivencia obtidas. O modelo de resposta presentado consta de dúas ecuacións diferenciais con impulsos que describen respectivamente a dinámica das células tumorais viables e das células danadas que son eliminadas por efecto do tratamento. Este modelo axustouse a datos experimentais de volumes preclínicos empregando o algoritmo de optimización *Simulated Annealing*. Tomando como referencia os valores óptimos obtidos para os parámetros que describen o modelo, xerouse unha poboación cun gran número de tumores simulados, divididos en grupos control, radioterapia FLASH e radioterapia convencional, e estudáronse as diferenzas en volume e TCP entre os distintos grupos. O estudo suxire, de acordo con experimentos preclínicos, que as diferenzas en volume entre os grupos asignados a ambas terapias non son significativas na maioría dos casos, polo que a radioterapia FLASH podería semellar isoefectiva respecto da convencional.

A continuación, estudouse a isoefectividade en termos da TCP. Fixéronse dous estudos independentes sobre a poboación de tumores simulados para analizar posibles factores que inflúen no control tumoral. Inicialmente asignáronse tres cocientes α/β distintos (3, 10 e 20) para estudar como afecta a radiosensibilidade das células á perda de control tumoral, atopando que a maior diferenza entre as radioterapias FLASH e convencional se dá para tumores con cocientes baixos. Isto pode explicarse á vista da ecuación do modelo LQ coa modificación dos OERs, na cal se ve que o parámetro β (cadrático) engade maior sensibilidade aos cambios de osixenación.

Por outro lado, tomando como referencia o caso para $\alpha/\beta = 10$ Gy, dividiuse a poboación en función da súa osixenación mediana en tres grupos: osixenación baixa (menor de 10 mmHg), media (entre 10 e 20 mmHg) ou alta (maior de 20 mmHg). Obtívose que a maior perda de TCP se dá nos tumores máis osixenados. Pola contra, cando se analiza a supervivencia celular das células para distintos niveis de osíxeno, a maior diferenza entre ambas terapias dáse para osixenacións baixas, arredor dos 2–6 mmHg. Esta aparente contradición está causada pola heteroxeneidade nas osixe-

nacións tumorais. As zonas de baixa osixenación están presentes tamén en tumores "ben osixenados"e son as que marcan a TCP, ao ser as máis resistentes ao tratamento. Dado que as doses necesarias para acadar unha certa TCP coa terapia convencional son menores en tumores ben osixenados, poden resultar insuficientes para eliminar as células que entran en hipoxia como consecuencia da caída de osíxeno durante a terapia FLASH, mentres que as doses máis elevadas asociadas aos tumores óxicos seguen sendo efectivas para as células que sofren dita transición. Polo tanto, é posible que na incorporación da radioterapia FLASH ao ámbito clínico se deban aumentar as doses administradas con respecto á terapia convencional para acadar a mesma efectividade en determinados casos.

En conclusión, esta tese presenta dous modelos matemáticos de resposta tumoral a técnicas de radioterapia avanzada que xurdiron nos últimos anos, a radioinmunoterapia e a radioterapia FLASH. Responde así á necesidade de desenvolver novos modelos para estudar o efecto dos tratamentos e explorar os mecanismos asociados aos mesmos que non son efecto directo do dano celular por radiación. Os modelos clásicos como o LQ e as súas variantes non son suficientes para describir mecanismos de morte indirecta que involucran múltiples axentes do microentorno tumoral ou outros efectos biolóxicos e fisicoquímicos asociados á terapia, non sendo óptimos para a planificación dos tratamentos no ámbito clínico. Os modelos presentados validáronse co seu axuste a datos experimentais e empregáronse para estudar os mecanismos subxacentes á efectividade dos tratamentos. En canto á radioinmunoterapia, os resultados apuntan a que os retardos biolóxicos asociados ao transporte das células T desde os órganos linfoides cara o tumor poden ter un papel relevante na planificación dos tratamentos. Por outro lado, viuse que as curvas de crecemento tumoral poden ser insuficientes para establecer a isoefectividade das radioterapias FLASH e convencional en termos da TCP, de maior interese na práctica clínica. As variacións de osíxeno asociadas á radioterapia FLASH poden derivar nun aumento da fracción de supervivencia tumoral, que non leva a diferencias significativas nas curvas de volume (para os tamaños mostrais empregados nos estudos preclínicos) pero trasládase á TCP, proporcionando taxas de control máis baixas que as da modalidade convencional.

Chapter 1

Introduction

"No one told me there would be math!"
— Bart Simpson, *The Simpsons: Mathlete's Feat.*

Since the inception of radiation as a cancer therapy, mathematical models have emerged as a valuable tool for designing treatments and predicting their outcomes. This thesis aims to present novel mathematical models that may contribute to a better understanding and planning of advanced radiotherapy treatments that have emerged in recent years, such as radioimmunotherapy and FLASH radiotherapy.

This introduction provides a historical overview of the use of radiation in cancer treatment, from its first clinical applications in the early-20th century to the development of more advanced techniques used today. Additionally, this chapter offers insights into classical mathematical models employed since the 1950s, which have assisted oncologists and medical physicists in designing clinical treatments. These models constitute the foundation for developing more complex and suitable mathematical models to describe the effect of novel radiation treatments like radioimmunotherapy and FLASH radiotherapy; these techniques are introduced later in this chapter. In the final section, the motivation and objectives of this thesis are stated.

1.1 Cancer and RadioTherapy (RT)

Cancer is a complex disease that encompasses more than two hundred different genetic diseases that can affect almost any part of the body. A shared characteristic among all of them is the uncontrolled multiplication of abnormal cells, which can spread to surrounding tissue and lead to metastases in distant parts of the organism. The cell cycle of cancer cells is disrupted, allowing old or damaged cells to survive when they should be naturally eliminated, and new cells to form unnecessarily. In most cases, this process causes the formation of solid tumors, except for particular cases such as blood cell cancers (leukemia).

RadioTherapy (RT) is a medical treatment that delivers high radiation doses to kill or damage cancer cells, aiming to eliminate tumors or decrease tumor cell growth. The local administration of X-rays, γ-rays, protons, or electrons through different modalities induces DNA damage, inhibits the cell cycle, and ultimately results in tumor cell death. Radiation damage on cells is usually categorized as lethal when cellular structures are irreparably damaged and the cell is doomed, and sublethal when it is not immediately lethal but can lead to cell death if it is not repaired or accumulates with successive damage.

The biological effects of radiation on cells depend on several factors such as the total delivered dose, the fractionation schedule, or the particular radiosensitivity of cells. Tumor cells are known to be more sensitive to radiation damage than normal cells. The accelerated multiplication rates of tumor cells make them more susceptible to DNA damage. Moreover, the capacity of tumor cells to repair sublethal damage is generally lower due to mutations. These differences between normal and tumor cells to deal with damage repair motivated the design of fractionated treatments that maximize the damage on tumor cells while minimizing the damage on normal cells, allowing for effective repair between fractions of dose.

In clinical practice, RT treatments are commonly planned according to an administration schedule. Typically, doses are divided and administered on consecutive days, from Monday to Friday, until completing the total prescribed dose. Given a radiation dose, D, it is divided in n fractions, $d_i, i = 1 \dots n$, having $D = \sum_{i=1}^{n} d_i$. Conventional treatments are given in 30–40 fractions of 1.8–2 Gy* per fraction, one fraction a day.

Since its inception in the early-20th century, RT has become a pivotal tool to treat cancer. Currently, over half of the patients diagnosed with cancer undergo RT, either alone or in combination with other techniques like chemotherapy and surgery.

*Radiation doses are measured in gray (Gy), which is the unit of measurement in the International System. One gray is equivalent to the absorption of one joule (J) of energy per kilogram (kg) of the irradiated material mass.

1.2 Radiation treatments through time

The history of RT dates back to 1895 when Wilhelm Conrad Röntgen discovered X-rays and the interest in their potential medical applications sparked [1]. Just a year after Röntgen's discovery, Émil Herman Grubbé used X-rays to treat a patient with breast cancer [2]. In 1896, the physicist Antoine Henri Becquerel discovered the phenomenon of radioactivity while studying uranium salts. This finding laid the foundation for understanding the radioactive properties of certain elements. In 1898, the pioneering work of Marie Skłodowska-Curie and Pierre Curie impulsed RT forward when they discovered radium as a radiation source. During that time, there was very little knowledge about the biological effects of radiation and the side effects resulting from its use. Three years later, Becquerel and Curie described the physiologic impacts of radium rays [3].

The first clinical applications of RT were primarily the treatment of skin cancers and benign lesions. In 1913, William David Coolidge developed a new device capable of emitting higher energy X-rays [4], which made it possible to treat deep-seated tumors, marking a significant advancement in cancer care. Nevertheless, due to limited knowledge of RT, its effectiveness in cancer treatment was outweighed by the negative side effects. Subsequent studies led to a better understanding of radiation's nature and optimal dosage administration by the 1920s. During this period, physicians found that fractionating the total dose into smaller doses was more effective in cancer control and resulted in fewer side effects [5].

From 1930 to 1950, the development of more precise radiation machines and techniques significantly enhanced RT in medical practice. The introduction of linear accelerators in the mid-20th century represented a major leap in RT technology [6], although they did not become widespread in clinical practice until the late-20th and early-21th centuries. These machines could generate high-energy X-rays, enabling even more precise and controlled radiation delivery to tumors while sparing healthy surrounding tissues.

In recent decades, the focus of advancements in RT has been on refining treatments to minimize the toxicity experienced by cancer patients while enhancing the effectiveness of radiation on tumors. Novel technologies like Intensity-Modulated RT (IMRT), Image-Guided RT (IGRT), and Volumetric Modulated Arc Therapy (VMAT) have facilitated more accurate delivery of radiation doses, reducing the toxicity of RT treatments in tissues surrounding the tumor.

Furthermore, the emergence of Stereotactic Body RT (SBRT) and Stereotactic Radiation Surgery (SRS) has enabled the administration of high radiation doses in a small number of sessions, leading to hypofractionated RT. These advancements allow for treatments characterized by higher doses per fraction (8–30 Gy) and a reduced number of administration days. Many studies argue that this new approach leads to fewer side effects [7, 8], enhanced local control [9], and a better quality of life for patients as it requires fewer treatment sessions.

Moreover, new RT modalities have become a subject of active investigation, with ongoing clinical trials aimed at further understanding their potential benefits. For example, RadioImmunoTherapy (RIT) in various modalities, such as Immune Checkpoint Inhibitors (ICIs), Chimeric Antigen Receptor (CAR)-T cell therapy, and cancer vaccines; Spatially Fractionated RT (SFRT), including GRID RT, minibeam RT, and microbeam RT; and Ultra-High Dose Rate (UHDR) treatments such as FLASH RT (FLASH-RT).

Over time, RT has evolved into a more interdisciplinary field where various professionals, including oncologists, physicists, biologists, engineers, and mathematicians, collaborate on treatment planning and the exploration of new therapies.

1.3 Mathematical models in RT

Shortly after the inception of RT as a cancer treatment, mathematical models emerged as a valuable tool to investigate the effects of radiation on cells and to estimate the outcome of RT treatments. Since then, radiobiological models have been used to describe the biological effect of radiation on cells and tissues. These models relate physical variables, like the absorbed radiation dose, with biological quantities, such as the survival probability of a cell after being irradiated. In the case of tissues and cell cultures, this probability is named as the Surviving Fraction (SF), denoting the proportion of cells that survive the treatment out of the total. In this context, survival is understood as the capacity of cells to maintain their functionality and, in the case of proliferative cells, their ability to replicate.

Since its early formulations over 50 years ago, the Linear-Quadratic (LQ) model [10] has been the most widely used radiobiological model to describe the biological effects of ionizing radiation on cancer cells and normal tissues, giving a simple expression to obtain the SF from the radiation dose. This model comes from various publications, which over decades independently proposed equivalent expressions to the modern LQ model, introduced later in this section. Researchers observed the resulting SF for different doses in *in vitro* experiments and found a phenomenological expression to reproduce these patterns. Thus, the LQ model is not mechanistic, although it can be related to biological processes of cell death as explained later in this section.

The design of mathematical models to estimate the SF allowed the development of formulas to calculate the likelihood that a RT treatment effectively controls or eliminates a tumor, and causes damage in the surrounding normal tissue, known as the Tumor Control Probability (TCP) and Normal Tissue Complication Probability (NTCP), respectively. The LQ model is widely used in clinical practice to assist in treatment planning, dose optimization, and assessing the risk-benefit profile of RT treatments.

The development of SBRT and SRS in the 1990s led to *hypofractionated* RT, a new modality consisting of less fractionated treatments with high doses per fraction.

Unlike conventional RT, which may involve multiple sessions over several weeks, hypofractionated RT typically completes the treatment in one to five sessions.

Many studies have shown improvement in local control with hypofractionated against conventional RT [9]. Recent studies have argued that high doses trigger indirect mechanisms of cell death related to vascular damage and immune response enhancement [7, 11–20], which may increase the radiation effect. However, there is controversy about the contribution of indirect cell death mechanisms to tumor control rates [21–23]. On the contrary, some studies have attributed high levels of control only to dose escalation [24, 25].

The LQ model has been questioned when describing the radiation effect in hypofractionated RT, as it might not be accurate for large doses per fraction [26–30]. Some experimental studies have shown that at high doses per fraction, the radiation effect is lower than expected when extrapolating the results from low doses per fraction due to an effect of "damage saturation" [26, 31]. Among others, the Linear-Quadratic-Linear (LQL) model [32] has been proposed as an alternative to describing the radiation effect with damage saturation for high doses per fraction. Additionally, new models have been proposed attempting to account for indirect cell death mechanisms such as vascular damage and radiation-induced immune response [33–35].

Despite the valuable contribution of the LQ model and its derived forms in planning RT treatments, two main factors motivate the necessity of developing more complex mathematical models. On the one hand, the current trend in RT is to design increasingly personalized treatments to maximize therapy effectiveness while minimizing side effects based on the specific characteristics of each patient. This consideration makes it necessary to incorporate more patient-specific variables into the models. On the other hand, technological advances in recent decades have led to more advanced RT techniques involving new cell death mechanisms that are not a direct consequence of radiation damage. Thus, novel models must incorporate these new agents.

This section presents mathematical models in RT, such as the LQ model, the LQL model, and other derived expressions, which are the basis for constructing more complex models in RT advanced techniques.

1.3.1 Linear-Quadratic (LQ) model

For a radiation dose, d (Gy), the Linear-Quadratic (LQ) model gives the following expression to calculate the SF:

$$SF(d) = \exp\left(-\alpha d - \beta d^2\right), \tag{1.1}$$

where α (Gy^{-1}) and β (Gy^{-2}) are cell-specific parameters that characterize the radiosensitivity of cells.

The LQ model was initially designed as a phenomenological model based on empirical observations and experimental data. Nevertheless, the α and β parameters were

later interpreted as the biological contribution of two different mechanisms of cell death induced by radiation [36]. On the one hand, the linear parameter, α, quantifies the lethal damage caused by a single incident particle, which is irreparable. On the other hand, the quadratic parameter, β, accounts for the sublethal damage caused by multiple radiation tracks, that is normally reparable unless its accumulation leads to cell elimination. The α/β (Gy) ratio gives the dose at which the linear and quadratic terms contribute equally to cell death. This parameter is paramount in understanding tumor response to dose fractionation. Figure 1.1 shows the resulting SF-dose curves.

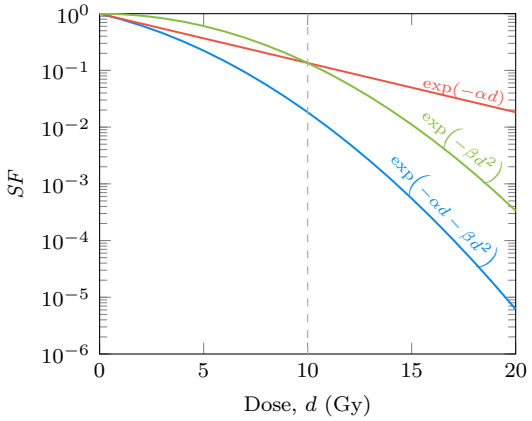

Figure 1.1: Surviving Fraction (SF) versus dose curves obtained from the Linear-Quadratic (LQ) model with parameters $\alpha = 0.20$ Gy^{-1} and $\beta = 0.02$ Gy^{-2}. Along with the SF curve, the linear and quadratic contributions are represented separately. Note that both curves intersect at $\alpha/\beta = 10$ Gy. The vertical axis is on a logarithmic scale.

As previously mentioned, RT treatments are typically scheduled in multiple fractions of dose. Considering time intervals between fractions that allow for the repair of sublethal damage, the impact of each dose fraction can be considered independent. For a cumulative radiation dose, D, delivered in n fractions of dose denoted as $\{d_i, i = 1 \dots n\}$, thus $D = \sum_{i=1}^{n} d_i$, the corresponding SF derived from equation (1.1) is as follows:

$$SF(D) = \prod_{i=1}^{n} \exp\left(-\alpha d_i - \beta d_i^2\right) = \exp\left(\sum_{i=1}^{n} \left(-\alpha d_i - \beta d_i^2\right)\right). \tag{1.2}$$

Assuming that all dose fractions are identical, $d_i = d$, $\forall i = 1 \dots n$, the total radiation dose can be written as $D = nd$, and from the above equation it follows:

$$SF(D) = \exp\left(n\left(-\alpha d - \beta d^2\right)\right) = \exp\left(-\alpha n d - \beta n \left(d\right)^2\right) = \exp\left(-\alpha D - \beta d D\right). \tag{1.3}$$

Due to its simplicity, the LQ model is in most cases the preferred method to characterize the effect of radiation treatments, but it also presents some limitations. This model simplifies the complex biological responses to radiation, which may not be accurate for all situations.

LQ model with OER modification

One factor that has proved to influence cell survival is the oxygenation status of cells. Low oxygen levels (*hypoxia*) may inhibit the proliferation of cells and lead to cell death. However, hypoxia is also associated with enhanced tumor progression and cell radioresistance, motivated by both biological and physico-chemical effects [37–40].

On the one hand, tumor hypoxia and the total absence of measurable oxygen (*anoxia*) are related to the increased malignant phenotype of tumors. The Hypoxia Inducible Factor (HIF) is a protein present in cells that, at low oxygen concentrations, promotes the activation of specific genes that participate in the proliferation of cells to favor cell survival. Cancer cells may benefit from this process to potentiate tumor progression [40].

On the other hand, hypoxia may protect cells from radiation damage. Ionizing radiation interacts with water molecules in the Tumor MicroEnvironment (TME) and promotes the production of high-energy electrons, a process known as *radiolysis*. These electrons interact with other water molecules and produce free radicals (reactive chemical entities with unpaired electrons) that damage cell DNA. The *oxygen fixation damage hypothesis* states that radical-induced damage on cell DNA can be made permanent in the presence of molecular oxygen, leading to irreparable damage [41].

To compensate for the effect of hypoxia in increasing cell survival, the LQ model is modified by introducing the Oxygen Enhancement Ratios (OERs). This concept represents the ratio of the dose required to produce a given biological effect under hypoxic conditions to the dose required under aerobic conditions. The resulting phenomenological model was designed to fit SF–dose curves of *in vitro* experiments with different oxygenation statuses.

The OERs are introduced in equation (1.1) [42], having the LQ model with OER modification:

$$SF(d,p) = \exp\left(-\alpha(p)d - \beta(p)d^2\right), \tag{1.4}$$

where the radiation damage parameters depend on the oxygen partial pressure, p:

$$\alpha(p) = \frac{\alpha_{\text{ox}}}{OER_\alpha}\frac{OER_\alpha p + k_{\text{m}}}{p + k_{\text{m}}}, \tag{1.5}$$

$$\beta(p) = \frac{\beta_{\text{ox}}}{OER_\beta^2}\frac{(OER_\beta p + k_{\text{m}})^2}{(p + k_{\text{m}})^2}, \tag{1.6}$$

being α_{ox} and β_{ox} the α and β parameters under fully aerobic conditions; OER_α and OER_β the maximum oxygen enhancement ratios; and k_m (mmHg) the oxygen partial pressure at which OERs achieve the half-maximum value. The effect of the OERs tends to be zero as the oxygen pressure increases, thus the $\alpha(p)$ and $\beta(p)$ values given by equations (1.5) and (1.6) approximate to α_{ox} and β_{ox}, respectively. Analogously, equation (1.4) tends to equation (1.1) under high oxygen levels. Typically, OER_α and OER_β values are within the range 2.50–3 and k_m is set to 3.28 mmHg [42].

Figure 1.2 shows SF–dose curves obtained for different oxygen statuses together with the response under aerobic conditions obtained through the LQ model.

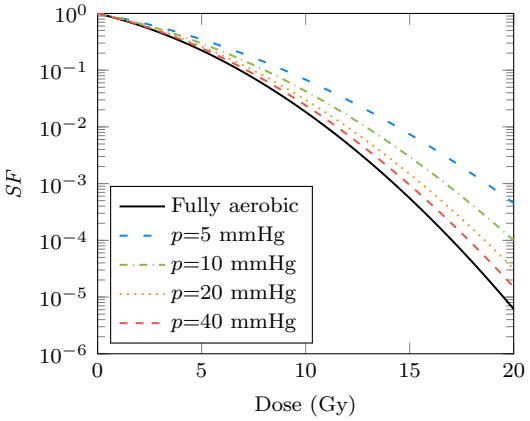

Figure 1.2: Surviving Fraction (SF) versus dose curves obtained from equation (1.4) for different oxygen partial pressures, p, and equation (1.1) under aerobic conditions, with the parameters $\alpha_{ox} = 0.20$ Gy^{-1}, $\beta_{ox} = 0.02$ Gy^{-2}, $OER_\alpha = 2.50$, $OER_\beta = 2.50$ and $k_m = 3.28$ mmHg. The vertical axis is on a logarithmic scale.

1.3.2 Linear-Quadratic-Linear (LQL) model

The Linear-Quadratic-Linear (LQL) model [32] is an extension of the LQ model (1.1) that includes a term that compensates for the LQ underestimation of sublethal damage repair. The SF obtained with the LQL model is given by:

$$SF(d) = \exp\left(-\alpha d - \frac{2\beta}{\gamma^2}\left(\gamma d - 1 + \exp\left(-\gamma d\right)\right)\right), \tag{1.7}$$

where γ (Gy^{-1}) is an extra parameter that modules the slope of the curve.

The above expression results from considering that the repair of sublethal damage, represented by the quadratic term, depends on the delivered dose. Thus, the maximum

effect of radiation is given by the LQ model, but when considering sublethal damage repair, equation (1.1) becomes:

$$SF(d) = \exp\left(-\alpha d - G\beta d^2\right), \tag{1.8}$$

where G is named the *dose protraction factor* [32, 43], given by:

$$G = \frac{2}{d^2}\int_0^\infty \dot{D}(t)dt \int_0^t \exp\left(-\lambda\left(t-t'\right)\right)\dot{D}(t')dt', \tag{1.9}$$

being λ the repair rate, and $\dot{D}$ the dose rate.

For T, the delivery time of the dose d, and a constant dose rate, it follows that $\dot{D} = d/T$ for $0 \leq t \leq T$. Thus, integrating the above expression gives:

$$G = \frac{2\left(\lambda T + \exp\left(-\lambda T\right) - 1\right)}{(\lambda T)^2}, \tag{1.10}$$

that considering $\gamma d = \lambda T$, becomes equation (1.7).

As shown in Figure 1.3, when the dose increases, the calculated SF from the LQL model is higher compared to the LQ model.

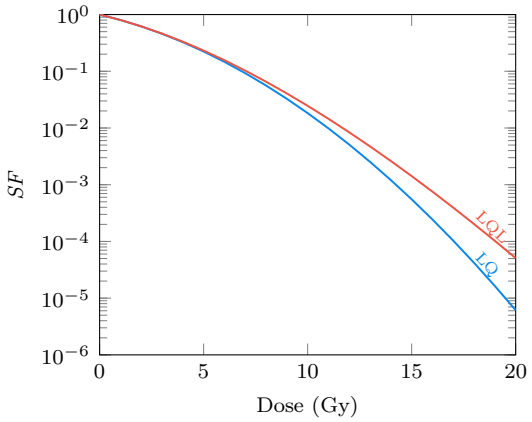

Figure 1.3: Surviving Fraction (SF) versus dose curves obtained from the Linear-Quadratic (LQ) and Linear-Quadratic-Linear (LQL) models with parameters $\alpha = 0.20$ Gy^{-1} and $\beta = 0.02$ Gy^{-2} in both models, and $\gamma = 0.05$ Gy^{-1} in the LQL model. The vertical axis is on a logarithmic scale.

1.3.3 Biologically Effective Dose (BED)

The Biologically Effective Dose (BED) is a concept used to compare the biological effects of different radiation fractionation schemes, taking into account both physical

magnitudes, such as the dose per fraction, d, and the total dose, D; and biological aspects, like the α/β ratio.

Based on the LQ model, the Biologically Effective Dose (BED) is calculated as follows [44, 45]:

$$BED = D\left(1 + \frac{d}{\alpha/\beta}\right). \tag{1.11}$$

Tumors with low α/β ratios are more sensitive to fractionation as shown in Figure 1.4. Thus, these tumors benefit less from increasing the number of fractions.

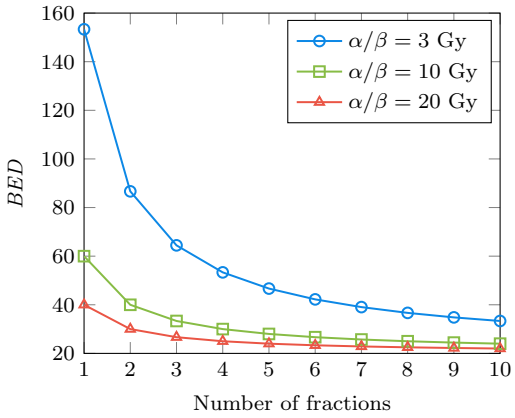

Figure 1.4: Biologically Effective Dose (BED) curves for different α/β ratios obtained from equation (1.11) with a total dose $D = 20$ Gy varying the number of fractions.

Using the BED facilitates the search for optimal treatments that give the desired therapeutic effect while minimizing damage to surrounding healthy tissues. However, two different treatments with the same BED can promote different outcomes due to particular aspects of the TME.

1.3.4 Tumor Control Probability (TCP)

The Tumor Control Probability (TCP) is a concept used to quantify the likelihood that a RT treatment effectively controls or eliminates a tumor.

The most common approach [46] to calculate TCP assumes that a single tumor cell has the potential to proliferate and derive tumor regrowth, known as the *clonogenic cell hypothesis* [47]. Moreover, this model assumes that cells are eliminated randomly and independently, with each cell having a survival probability SF. From the above considerations, TCP is defined as the probability that all tumor cells are eliminated.

Let N be the variable describing the number of cells that survive the treatment, and N_0 be the initial number of cancer cells within a tumor. Considering that N

follows a Poisson distribution with $S = N_0 SF$ as the expected number of surviving cells, it follows:

$$P(N) = \frac{\exp(-S)S^N}{N!}. \tag{1.12}$$

Thus, TCP is given by the probability of having no surviving cells, resulting in:

$$TCP = P(0) = \exp\left(-N_0 SF\right). \tag{1.13}$$

Particularly, the LQ-Poisson methodology to calculate the TCP based on the LQ model (1.1) gives:

$$TCP(d) = \exp\left(-N_0 \exp\left(-\alpha d - \beta d^2\right)\right). \tag{1.14}$$

1.4 Advanced techniques of RT

The technological advances of the last decades enabled the development of new RT modalities that aim at maximizing the radiation effect on tumor cells while decreasing the toxicity on surrounding organs and tissues.

This thesis focuses on two techniques introduced in this section: the combination of RT with ImmunoTherapy (IT), namely RadioImmunoTherapy (RIT), and FLASH-RT.

1.4.1 ImmunoTherapy (IT)

In contrast to traditional cancer treatments such as surgery, chemotherapy, and RT, which directly target the tumor, IT aims to stimulate and enhance the natural ability of the immune system to recognize and eliminate cancer cells [48, 49].

The immune response comprises a sequence of steps where immune cells identify and eliminate foreign harmful agents. In the context of cancer, this process is referred to as the *immune cycle of cancer* [50], detailed later in this section.

In the course of the immune response, the organism relies on regulatory mechanisms known as *immune checkpoints* at different stages of the cycle. These checkpoints prevent excessive immune reactions that may otherwise lead to inflammatory diseases. However, certain tumors exploit them to counteract the immune response and evade anti-tumor defenses. The most extensively studied immune checkpoints are the Cytotoxic T-Lymphocyte Antigen 4 (CTLA-4) receptor, found on the surface of immune cells and playing a role in their activation; and the Programmed Death 1 (PD-1)/Programmed Death-Ligand 1 (PD-L1) pathway, which significantly influences the identification of target cells.

The history of IT dates back to 1891 when Dr. William Coley, considered the father of IT, observed that some cancer patients experienced tumor regression after bacterial infections. Inspired by these findings, he developed a treatment using bacteria which, although showed some success, had limited acceptance by oncologists due

to inconsistent results. While several IT advancements emerged in the latter half of the 20th century, it was not until the 2010s that Immune Checkpoint Inhibitors (ICIs) demonstrated significant success in treating diverse cancers, particularly when combined with RT [51].

The immunity cycle of cancer

The cancer immunity cycle [50] is a recurring process where the immune system identifies and responds to harmful agents within the organism. This complex response involves components of the TME, such as tumor cells, antigens (molecular structures enabling the immune system to discern the presence of cancer cells), and immune cells, like T-cells. Immune cells can directly target and eliminate tumor cells displaying antigens, being a defense mechanism against the development and progression of cancer.

Figure 1.5 illustrates the different phases of the anti-tumor immune response. Initially, the presence of tumor cells promotes the release of antigens, which are different from those released by cells infected with other pathogens (step 1). Then, Antigen Presenting Cells (APCs), particularly Dendritic Cells (DCs) capture these antigens and migrate to lymphoid organs (step 2), where T-cells identify them and become active against the specific presented antigen, triggering the immune response (step 3). Subsequently, activated T-cells migrate towards the tumor (step 4) and infiltrate it (step 5). Finally, T-cells recognize the tumor cells and eliminate them (step 6), resulting in the release of new antigens, thereby initiating the immunity cycle again.

Immune Checkpoint Inhibitors (ICIs)

As previously mentioned, the organism relies on certain mechanisms to regulate the immune response and prevent excessive reactions that could lead to inflammatory diseases. Cancer takes advantage of these mechanisms to evade the anti-tumor immune response. Two examples of scape tactics are the stimulation of CTLA-4 receptor on the surface of T-cells and the PD-1/PD-L1 pathway.

The CTLA-4 receptor is involved in step 3 of the immunity cycle, where T-cells are activated against a specific antigen presented on the surface of APCs. As depicted in Figure 1.6, T-cell activation requires at least two signals [52]. Initially, the T-Cell Receptor (TCR) binds to the antigen sustained in a structure known as Major Histocompatibility Complex (MHC) on the surface of APCs, initiating T-cell activation. Subsequently, the co-stimulatory molecule Cluster of Differentiation (CD)28 must interact with one of its ligands, CD80 or CD86, to complete the activation process.

During the activation procedure, the CTLA-4 receptor matures on the cell surface and competes with CD28 for binding to its ligands. If CTLA-4 binds to CD28, it inhibits T-cell activation, acting as an ICI to prevent premature T-cell overactivation.

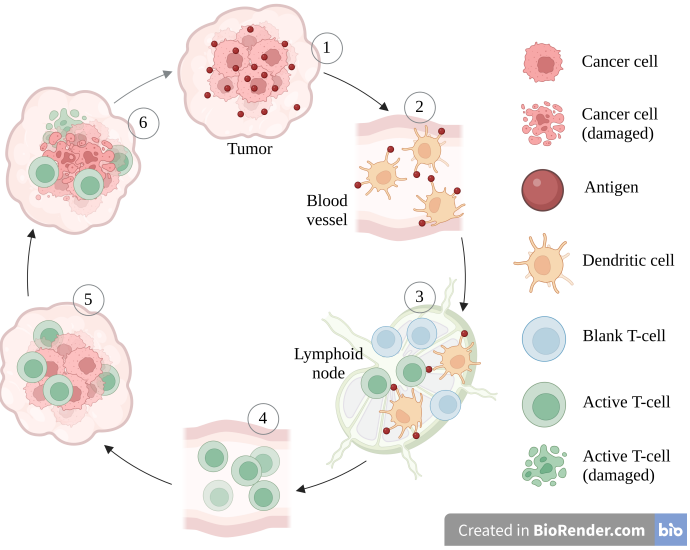

Figure 1.5: Phases of the immunity cycle of cancer response. 1) Tumor cells release antigens; 2) Dendritic Cells (DCs) take antigens to activation sites (lymphoid nodes); 3) T-cells against tumor cells are activated; 4) T-cells migrate towards the tumor and 5) infiltrate it; 6) T-cells attack tumor cells and kill them. [Created in BioRender.com.]

In 2011, *ipilimumab* became the first approved human antibody against the receptor CTLA-4 [52]. Treatments with anti-CTLA-4 (αCTLA4) involve intravenous administration of the antibody, which binds to the CTLA-4 receptor, preventing its interaction with CD28 and promoting T-cell activation.

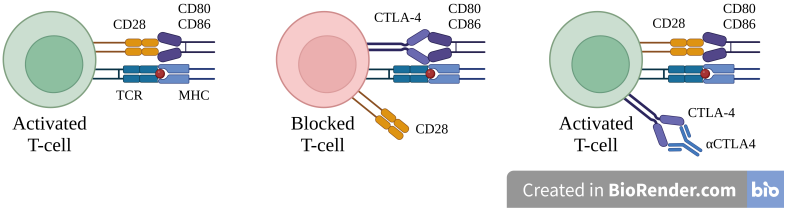

Figure 1.6: Step 3 of the immunity cycle. T-cell activation requires two signals: the binding of T-Cell Receptor (TCR) and the Major Histocompatibility Complex (MHC) sustaining the antigen, and the union of the Cluster of Differentiation (CD), which may be modulated by the Cytotoxic T-Lymphocyte Antigen 4 (CTLA-4) receptor and ImmunoTherapy (IT) with anti-CTLA-4 (αCTLA4). [Created in BioRender.com.]

In contrast, the PD-1/PD-L1 pathway is involved in step 6 of the immunity-cycle, as depicted in Figure 1.7. PD-1 is a protein on the surface of T-cells, and its ligand, PD-L1, is present on the surface of DCs and other cells in the TME. When PD-1 binds to PD-L1, the T-cell becomes "deactivated", serving as another ICI to avoid an excessive immune response. Tumor cells can present PD-L1 on their surface, using it as an escape mechanism [53].

The first anti-PD-1 (αPD1) and anti-PD-L1 (αPDL1) drugs (generally named as anti-Programmed Death-(Ligand) 1 (αPD(L)1)) emerged in the last decade. In 2014, the monoclonal antibodies *nivolumab* and *pembrolizumab* were approved to counteract the PD-1/PD-L1 evasion pathway. Similar to αCTLA4 drugs, αPD(L)1 antibodies are administrated intravenously and bind to their respective ligand to prevent T-cell deactivation.

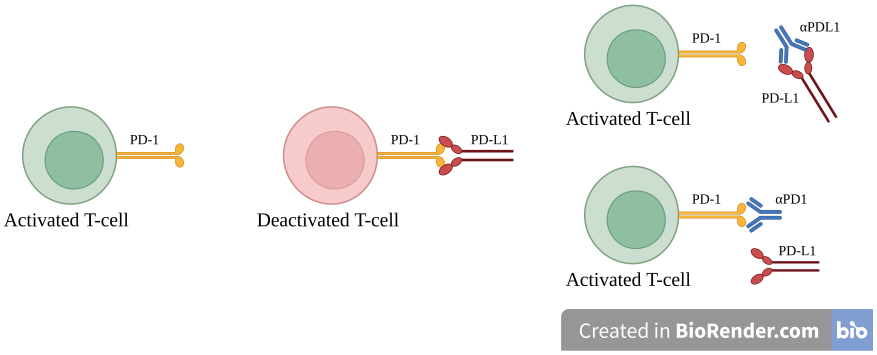

Figure 1.7: Step 6 of the immunity cycle. T-cells detect tumor cells regulated by the Programmed Death 1 (PD-1)/Programmed Death-Ligand 1 (PD-L1) pathway and ImmunoTherapy (IT) with anti-Programmed Death-(Ligand) 1 (αPD(L)1). [Created in BioRender.com.]

1.4.2 RadioImmunoTherapy (RIT)

RT is known to promote an immune anti-tumor response in the organism, although the mechanisms behind this effect are not fully understood. Radiation acts like an *in situ* vaccine that increases the recruiting of T-cells in the tumor site, motivated by the release of specific signals (antigens) [54]. It can even influence an immune response far from the irradiated field, contributing to eliminating metastasic tumors [55]. This phenomenon has been known as the *abscopal effect* since 1953.

Recently, IT has arisen as a promising complement to RT, leading to RIT treatments [56, 57]. In the context of cancer treatment, IT pursues the goal of stimulating or enhancing the immune response to target and eliminate cancer cells. As mentioned

in the previous section, the use of IT drugs with ICIs blocks inhibitory signals in the immune system, allowing T-cells to recognize and attack cancer cells more effectively. Particularly, IT with αCTLA4 and αPD(L)1 drugs enhances the natural anti-tumor response carried by the immune system, improving RT outcomes [18, 58, 59]. However, the success of RIT depends on patient-specific features, like the good behavior of their immune system [58]. Moreover, an excessive immune response can damage normal cells and promote inflammatory diseases, increasing toxicity. For these reasons, RIT continues to be a field of ongoing research.

The synergy between RT and IT

RT not only induces an anti-tumor immune response, which can be enhanced by RIT, but also leads to some immunosuppressive effects. Radiation damages both tumor cells and T-cells present within the tumor at the irradiation time, as well as the vascular system which serves as the infiltration way of immune cells and, if damaged, can lead to hypoxia and radioresistance (although the effect of vascular damage on tumor control has been debated [11, 14, 21–23]).

Hypofractionated RIT has been demonstrated to improve tumor control rates in preclinical experiments compared to the independent use of RT and IT as monotherapies [58, 59]. One of the reasons behind this may be that in conventional RT, when T-cells infiltrate the tumor days after the first RT fraction, the tumor continues to be irradiated, and T-cells are damaged; while in hypofractionated regimens, T-cells that progressively infiltrate the tumor are exposed to fewer radiation fractions. Previous preclinical research has studied the effect of different fractionations on the immune cells, finding that hypofractionated treatments increase T-cell accumulation within the tumor a few days after the first fraction compared to more fractionated procedures [15, 19, 58]. However, this phenomenon must be further investigated.

Finding the combination of both therapies that maximizes their synergistic effect is not straightforward and it is necessary to find new approaches that help in designing optimal treatments. Modeling RIT requires the necessary description of indirect immune-mediated effects and the two-faced effect of radiation as an immunosuppressive (damages circulating T-cells and tumor vasculature) and immunostimulatory factor (increases the recruiting of T-cells in the tumor). Thus, simple models, such as the LQ model and its derived forms presented in the previous sections, are insufficient to explain the complex interactions of radiation and IT drugs with the immunity cycle of cancer. In recent years, some research studies have presented new mathematical models in RIT, attempting to explore the mechanisms behind its effect and to assist in treatment planning [60].

1.4.3 FLASH RadioTherapy (FLASH-RT)

FLASH-RT is a novel treatment strategy that consists of delivering radiation doses at UHDRs, exceeding the 40 Gy s^{-1} instead of the 0.05–0.40 Gy s^{-1} used in conventional RT (conv-RT) [61, 62].

In 1959, Dewey and Boag [63] reported the *FLASH effect* for the first time when comparing the radiation sensitivity to conv-RT and FLASH-RT in bacteria, finding that UHDRs led to lower damage. Similar results were observed later in mammalian cells and preclinical trials [64, 65]. More recent *in vivo* studies have shown the potential of FLASH-RT to maintain the effectiveness of conv-RT on tumors while sparing healthy surrounding tissue [66–74]. Considering these findings, FLASH-RT has emerged as a promising RT modality for future clinical practice.

The biological mechanisms involved in FLASH-RT are very complex [64] and constitute an active field of research. Many studies have suggested that the protective effect of healthy tissue arises from the Radiolytic Oxygen Depletion (ROD) process caused by FLASH irradiation [62, 75–78], which increases cell radioresistance.

As mentioned in Section 1.3.1, it is established that radiation can deplete oxygen in irradiated cells and tissues through the radiolysis of water molecules. The use of UHDRs promotes a quick ROD process in FLASH-RT. On the contrary, in conv-RT, the tumor vascular system continuously resupplies oxygen, preventing observable oxygen depletion. As discussed earlier in this chapter, hypoxic cells may be less responsive to RT, a phenomenon described by the OERs, presented in Section 1.3.1. That is mostly accepted as the reason behind the sparing effect of FLASH-RT in healthy tissues [65]. However, other research works propose that ROD alone is insufficient to fully explain the sparing effect. Instead, they attribute it to other factors like immune effects [61, 79]. The short exposure to radiation in FLASH-RT may significantly reduce the proportion of circulating immune cells that are irradiated and damaged, leading to a more effective immune system capable of repairing radiation-induced damage to normal tissue and contributing to reducing inflammation [65].

Understanding why the protective effect is not observed in tumors remains an ongoing area of research. Some studies suggest that oxygen depletion has a higher protective effect on healthy tissue as tumors generally present lower oxygen levels, limiting the benefits derived from ROD. Nevertheless, other studies propose that additional physicochemical factors may contribute to this phenomenon [61, 65], such as variations in reactive species production between tumor and non-tumor cells [80], the recombination of free radicals [81], or radiation-induced immune effects [79].

In recent years, theoretical work has accompanied experimental studies in an attempt to elucidate the underlying mechanisms of the FLASH effect [81–84].

1.5 Motivation and objectives

Mathematical models have long been paramount in analyzing the response of cells and tissues to radiation. In this regard, the LQ model has been widely used to design novel RT fractionations that have improved effectiveness and toxicity. However, in recent years, new RT techniques have emerged, such as RIT and FLASH-RT. These novel treatments involve cell death mechanisms not directly caused by radiation damage. Therefore, the LQ and LQ-derived models cannot fully describe the treatment outcome. These limitations motivate the development of new mathematical models, such as those presented in this thesis.

The main objective of this work is to develop novel tumor response models in RIT and FLASH-RT that serve to study the mechanisms behind their anti-tumor effect. The specific objectives are:

- To collect experimental data from the literature to validate the proposed models.
- To model the effect of biological delays on RIT, associated with the activation of immune cells and their infiltration within tumor tissue.
- To propose hypotheses regarding the optimal administration schedules for treatments combining RT and IT drugs.
- To model the effect of oxygen depletion during FLASH-RT on the treatment outcome.
- To argue about the circumstances under which FLASH-RT and conventional RT may demonstrate iso-effectiveness in clinical tumor control.

1.6 Outline

The rest of the document is structured as follows:

- Chapter 2 presents the mathematical and computational methods used in chapters 3 and 4 to design new mathematical models in RIT and FLASH-RT.
- Chapter 3 describes the specific methods and the obtained results in RIT.
- Chapter 4 describes the specific methods and the obtained results in FLASH-RT.
- Chapter 5 contains the conclusions of this doctoral thesis.

Chapter 2

Methods and materials

"I am on a curiosity voyage and I need my paddles to travel. These books... these books are my paddles"
— Dustin Henderson, *Stranger Things: The Pollywog.*

This chapter presents the mathematical and computational methods utilized for the development of this thesis. The primary focus is on introducing the mathematical tools used when designing novel tumor response models, the numerical methods employed to obtain solutions for these models, and the optimization algorithms utilized for model validation with experimental data available in the literature.

2.1 Tumor response models

Tumor response models are mathematical frameworks designed to describe the behavior of tumors to therapeutic interventions. In the previous chapter, the LQ (1.1) and LQL (1.7) models were presented as simple empirical expressions to describe tumor response to RT. More complex mechanistic models incorporate factors such as the proliferation of cancer cells, the role of the immune system, and the influence of the treatment on other components of the TME. These models aim to simulate the underlying dynamics of tumor growth, progression, and response to treatment.

As earlier introduced, advanced RT techniques require the development of new tumor response models that can simulate changes in tumor size, cell population dynamics, and overall treatment outcomes over time, being valuable tools to study their effectiveness. This thesis dissertation presents new mechanistic response models in RIT and FLASH-RT based on Ordinary Differential Equations (ODEs), Impulsive Differential Equations (IDEs), Delay Differential Equations (DDEs) and Partial Differential Equations (PDEs).

This section summarizes the theoretical results used in the following chapters to design differential models and obtain their numerical solution.

2.1.1 Impulsive Differential Equations (IDEs)

IDEs describe evolution processes characterized by sudden state changes caused by short-term perturbations that can be considered instantaneous when compared to the characteristic timescales of the problem being modeled.

These equations consist of three main components: a continuous-time differential equation modeling the state of the system between impulses, an impulsive equation describing the impulse jumps, and a jump criterion specifying the events that trigger the state changes.

Definition 1. Given a function $\boldsymbol{f} : B \subset \mathbb{R} \times \mathbb{R}^n \to \mathbb{R}^n$, the following equation is an *Impulsive Differential Equation (IDE)* [85–87]:

$$\begin{cases} \dfrac{d\boldsymbol{x}}{dt}(t) = \boldsymbol{f}(t, \boldsymbol{x}(t)), & \forall t \neq \tau_k, \\ \Delta\boldsymbol{x}(\tau_k) = \boldsymbol{I}_k(\boldsymbol{x}(\tau_k)), & \forall t = \tau_k, \end{cases} \tag{2.1}$$

where τ_k, $k = 1 \dots m$, are the *instants* or *moments of impulse*, $\boldsymbol{I}_k : \mathbb{R}^n \to \mathbb{R}^n$ is the *impulse* or *jump operator* at τ_k, and $\Delta\boldsymbol{x}(\tau_k) = \boldsymbol{x}(\tau_k^+) - \boldsymbol{x}(\tau_k^-)$, being $\boldsymbol{x}(\tau_k^+)$ and $\boldsymbol{x}(\tau_k^-)$ the right and left limits, respectively, of the state at $t = \tau_k$.

The instants of impulse can be fixed or state-dependent. This work concerns only fixed moments, having $\tau_1 < \ldots < \tau_k < \tau_{k+1} < \ldots < \tau_m$.

Definition 2. Let J be an arbitrary interval in $\mathbb{R}$. Then, a function $\boldsymbol{\phi} : J \to \mathbb{R}^n$ is said to be a *solution* of equation (2.1) on the interval J if:

1. $(t, \boldsymbol{\phi}(t)) \in B$ for $t \in J$,
2. $\boldsymbol{\phi}$ is differentiable in J for $t \neq \tau_k$, and satisfies equation (2.1) for all $t \in J$, and
3. $\boldsymbol{\phi}$ is continuous from the left in J, and if $\tau_k \in J$, $\tau_k \neq T$, then $\boldsymbol{\phi}(\tau_k^+) = \boldsymbol{\phi}(\tau_k) + \Delta\boldsymbol{\phi}(\tau_k)$.

Let Ω be a domain in $\mathbb{R}^n$, $J \subset \mathbb{R}$ and $\Delta_k = J \cap (\tau_k, \tau_{k+1}]$. $\mathcal{C}_\tau(J \times \Omega, \mathbb{R}^n)$ denotes the set of functions $\boldsymbol{f} : J \times \Omega \to \mathbb{R}^n$ which are continuous in the sets $\Delta_k \times \Omega$ and for each $\tau_k \in J$, $\tau_k \neq T$ and each $\boldsymbol{x} \in \Omega$ there exists the limit of $\boldsymbol{f}(t, \boldsymbol{y})$ as $(t, \boldsymbol{y}) \to (\tau_k, \boldsymbol{x})$, $t > \tau_k$.

The following theorem [85, 86] states conditions to guarantee the existence and uniqueness of a solution for the Initial Value Problem (IVP):

$$\begin{cases} \dfrac{d\boldsymbol{x}}{dt}(t) = \boldsymbol{f}(t, \boldsymbol{x}(t)), & \forall t \neq \tau_k, \\ \Delta\boldsymbol{x}(\tau_k) = \boldsymbol{I}_k(\boldsymbol{x}(\tau_k)), & \forall t = \tau_k, \\ \boldsymbol{x}(t_0^+) = \boldsymbol{x}_0. \end{cases} \tag{2.2}$$

Theorem 1. *Let $\boldsymbol{f} \in \mathcal{C}_\tau(\mathbb{R} \times \Omega, \mathbb{R}^n)$. Then, for each $(t_0, \boldsymbol{x}_0) \in \mathbb{R} \times \Omega$, there exists $b > t_0$ and a solution $\boldsymbol{x} : (t_0, b) \to \mathbb{R}^n$ of the IVP (2.2) with initial condition $\boldsymbol{x}(t_0^+) = \boldsymbol{x}_0$. Furthermore, if the function $\boldsymbol{f}$ is locally Lipschitz continuous with respect to $\boldsymbol{x}$ in $\mathbb{R} \times \Omega$, then this solution is unique. Besides, if $\boldsymbol{f}$ is globally Lipschitz continuous, then the solution is global.*

2.1.2 Delay Differential Equations (DDEs)

DDEs describe evolution processes for which the state of the system at a given time, t, depends not only on a function evaluated at t but also on the state at previous times.

Definition 3. Given a function $\boldsymbol{f} : \mathbb{R} \times U_1 \times \cdots \times U_{m+1} \to \mathbb{R}^n$, where $U_i \subset \mathbb{R}^n$, $i = 1 \ldots m+1$, the following expression is a *Delay Differential Equation (DDE)*:

$$\frac{d\boldsymbol{x}}{dt}(t) = \boldsymbol{f}(t, \boldsymbol{x}(t), \boldsymbol{x}(t - \tau_1(t)), \ldots, \boldsymbol{x}(t - \tau_k(t)), \ldots, \boldsymbol{x}(t - \tau_m(t))), \tag{2.3}$$

where $\tau_k(t)$, $k = 1 \ldots m$, are called the *time delays*, and m is the order of the DDE.

The time delays can be constant or state-dependent. This work concerns only constant delays, having $0 < \tau_1 < \ldots < \tau_k < \ldots < \tau_m$.

Note that equation (2.3) cannot be cast as an IVP by defining the solution at a unique $t = t_0$. The interval $[t_0 - \tau_m, t_0]$ is called the *initial interval* associated with the initial point t_0 and the DDE (2.3). Thus, the "initial condition" is given by $\boldsymbol{x}(t) = \boldsymbol{\gamma}(t)$ for $t_0 - \tau_m \leq t \leq t_0$, where $\boldsymbol{\gamma} : [t_0 - \tau_m, t_0] \to \mathbb{R}^n$ is called the *initial function* [88].

Definition 4. Suppose constant delays and $\boldsymbol{f} \in \mathcal{C}([t_0, \infty) \times U_1 \times \cdots \times U_{m+1}, \mathbb{R}^n)$, where $U_i \subset \mathbb{R}^n$, $i = 1 \ldots m+1$. Set $T > t_0$, and let J be either $[t_0, T)$, $[t_0, T]$, or $[t_0, \infty)$. Then, a function $\boldsymbol{\phi} : [t_0 - \tau_m, t_0] \cup J \to \mathbb{R}^n$ is said to be a *solution* of equation (2.3) on the interval J if:

1. $\boldsymbol{\phi}$ is continuous, and
2. $\boldsymbol{\phi}$ is continuously differentiable in J and satisfies equation (2.3) for all $t \in J$.

The following theorem [88] states conditions to guarantee the existence and uniqueness of a solution for the IVP:

$$\begin{cases} \dfrac{d\boldsymbol{x}}{dt}(t) = \boldsymbol{f}(t, \boldsymbol{x}(t), \boldsymbol{x}(t-\tau_1), \ldots, \boldsymbol{x}(t-\tau_k), \ldots, \boldsymbol{x}(t-\tau_m)), \ \forall t > t_0, \\ \boldsymbol{x}(t) = \boldsymbol{\gamma}(t), \ \forall t \in [t_0 - \tau_m, t_0]. \end{cases} \tag{2.4}$$

Theorem 2. *Suppose constant delays and $\boldsymbol{f} \in \mathcal{C}([t_0, \infty) \times U_1 \times \cdots \times U_{m+1}, \mathbb{R}^n)$, where $U_i \subset \mathbb{R}^n$, $i = 1 \ldots m+1$. Then, if $\boldsymbol{f}$ is globally Lipschitz continuous with respect to $\boldsymbol{x}$, and $\boldsymbol{\gamma} \in \mathcal{C}([t_0 - \tau_m, t_0], \mathbb{R}^n)$, the IVP (2.4) possesses a unique solution on $[t_0, \infty)$ Besides, if $\boldsymbol{f}$ is locally Lipschitz continuous, the solution is local.*

2.1.3 Numerical solution: forward Euler method

The forward Euler method [89] is usually employed to obtain the numerical solution of ODEs when they cannot be solved analytically or their analytical solution is complicated to calculate.

Let $\boldsymbol{f} : J \times \Omega \to \mathbb{R}^n$ be a given function, $J = [a, b] \subset \mathbb{R}$, $\Omega \subset \mathbb{R}^n$, and an initial condition $\boldsymbol{x}(a) = \boldsymbol{x}_0$, $\boldsymbol{x}_0 \in \mathbb{R}^n$. Given the following IVP:

$$\begin{cases} \dfrac{d\boldsymbol{x}}{dt}(t) = \boldsymbol{f}(t, \boldsymbol{x}(t)), \quad \forall t \in J, \\ \boldsymbol{x}(a) = \boldsymbol{x}_0, \end{cases} \tag{2.5}$$

and a discretization of J: $\{t_0 = a, t_1, \ldots, t_i, \ldots, t_l = b\}$, $i \in \mathbb{N}$, with $l+1$ nodes and fixed step size $\Delta t = t_{i+1} - t_i$, the forward Euler algorithm approximates the solution at each $(t_i, \boldsymbol{x}_i)$, $\boldsymbol{x}_i \coloneqq \boldsymbol{x}(t_i)$, as:

$$\begin{cases} \boldsymbol{x}_0, \\ \boldsymbol{x}_{i+1} = \boldsymbol{x}_i + \Delta t \ \boldsymbol{f}(t_i, \boldsymbol{x}_i), \quad 0 \leq i < l-1. \end{cases} \tag{2.6}$$

The forward Euler method presents certain limitations, particularly in stiff equations where it can be numerically unstable, unless the step size is chosen to be extremely small [90]. Moreover, it presents a slower convergence to the solution compared to others, such as Runge-Kutta and linear multistep methods. However, its simplicity reduces the implementation complexity of algorithms for solving IDEs and DDEs. The following chapters include stability studies to qualitatively compare the obtained solution using different time steps, ensuring the reliability of the numerical method when necessary.

Forward Euler method to solve IDEs

When solving IDEs, the impulse operators, $\boldsymbol{I}_k$ in equation (2.1), only apply at the impulse instants τ_k, so the numerical method behaves differently only at the jump moments (note that the impulse instants must be included as discretization nodes). The performance of the forward Euler algorithm is given by the following steps [87]:

Step 1: For all t_i, algorithm (2.6) is used until achieving an impulse instant.

Step 2: When found $t_i = \tau_k$, it is calculated the left limit $\boldsymbol{x}(\tau_k^-)$ through algorithm (2.6), and the jump operator is applied to obtain the right limit $\boldsymbol{x}(\tau_k^+)$.

Step 3: The previous steps are repeated until the final time is reached.

Forward Euler method to solve DDEs

The scheme of the forward Euler method applied to first-order DDEs, given by equation (2.3) for $m = 1$, is derived from algorithm (2.6), having [91]:

$$\begin{cases} \boldsymbol{x}_i = \boldsymbol{\gamma}(i\Delta t), & -j \leq i \leq 0, \\ \boldsymbol{x}_{i+1} = \boldsymbol{x}_i + \Delta t \ \boldsymbol{f}(t_i, \boldsymbol{x}_i, \boldsymbol{x}_{i-j}), & 0 \leq i < l-1, \end{cases} \tag{2.7}$$

where Δt is chosen so that the delay is an integer multiple of it, $\tau_1 = j\Delta t$, $j \geq 1$. This algorithm can be readily generalized to the case with a finite number of constant time delays.

2.2 Tumor oxygenation model

As mentioned in the previous chapter, oxygen plays a relevant role in tumor response to RT treatments, and it might be of paramount importance when modeling the outcomes of FLASH-RT, due to oxygen fluctuations because of the related ROD process.

Based on previous works [84, 92], this section presents a mathematical model to describe oxygen distribution in tumor tissue and the steps followed to obtain the

numerical solution of the oxygenation problem. Typically, tumor oxygenation is modeled by a reaction-diffusion PDE, which takes account of the oxygen supply through the vascular system and metabolic consumption by tumor cells. Furthermore, in the context of FLASH-RT, an additional consumption term associated with ROD is considered. The resulting oxygenation problem is addressed using the Finite Element Method (FEM) after defining the geometry of the problem and establishing initial and boundary conditions.

2.2.1 Mathematical model

Oxygen partial pressure, p, in tumor and healthy tissue is typically modeled by the following reaction-diffusion equation:

$$\frac{\partial p}{\partial t}(t, \boldsymbol{x}) = D_{\mathrm{O}_2} \Delta p(t, \boldsymbol{x}) - g(p(t, \boldsymbol{x})), \tag{2.8}$$

where $(t, \boldsymbol{x})$ are the temporal-spatial coordinates, Δ the Laplacian operator with respect to $\boldsymbol{x}$, D_{O_2} the oxygen diffusion coefficient and g a consumption term resulting from the addition of cellular metabolic activity [37, 93–96] and ROD [84], $g = g_{\mathrm{met}} + g_{\mathrm{ROD}}$, defined later in Sections 2.2.5 and 2.2.6, respectively.

2.2.2 Geometry of the problem

Tumors present a vascular network of capillaries that provide cells with oxygen and other nutrients needed to carry on their metabolic activity. The Vascular Fraction (VF) is defined as the fraction of the total tissue occupied by blood vessels. Following the work of Díaz-Botana [92], the VF is assumed to be homogeneous within the tumor, and oxygen distribution is described by a representative voxel (three-dimensional equivalence of a pixel) of tumor tissue. Moreover, to simplify the computational complexity of simulating oxygenation on three-dimensional vascular networks, the problem is simplified to a two-dimensional domain, which is a good surrogate of the three-dimensional problem for particular vascular networks [93]. Nevertheless, it must be noted that this approximation can miss some effects derived from the chaotic nature of tumor vascularity, as the two-dimensional simplification assumes parallel capillaries of equal length.

Following the previous considerations, the oxygenation problem is defined on a $1{\times}1$ mm^2 pixel with inner circles, representing tumor tissue and its vascular system, as shown in Figure 2.1. Capillaries are randomly located within the pixel following the next steps for the placement of each circle:

Step 1: Obtain the coordinates of the center using a uniform distribution.

Step 2: Assign a diameter characterized by a lognormal distribution obtained from the literature [97] and detailed in Table 2.1.

Step 3: Verify that the capillary is entirely within the pixel. Otherwise, reject it and return to Step 1.

Step 4: Verify that the capillary fits the minimum inter-vessel distance given in Table 2.1 with the previously positioned capillaries. Otherwise, reject it and return to Step 1.

These steps are repeated until the cumulative area occupied by capillaries reaches a given VF.

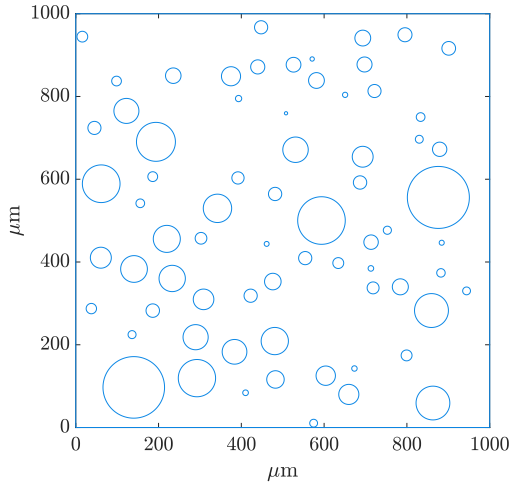

Figure 2.1: Example of a two-dimensional tumor domain. Geometry for the numerical simulation of the oxygenation problem. The inner circles represent blood capillaries of the tumor vascular system. This geometry corresponds to a VF $v_f = 0.14$.

	Size (μm)
Mean diameter	64.5
Standard deviation	58.0
Minimum diameter	0.9
Maximum diameter	161.9
Minimum inter-vessel distance	19.3

Table 2.1: Characteristics of the vascular vessels within the tumor, corresponding to experimental measurements of capillaries in the center of colorectal tumors [97]. Mean and standard deviation refer to the lognormal distribution.

2.2.3 Initial and boundary conditions

Imposing initial and boundary conditions, the following oxygenation problem is defined on a two-dimensional domain Ω with boundary $\Gamma = \Gamma_{\text{cap}} \sqcup \Gamma_{\text{out}}$:

Problem 2.1. *Find* $p : [t_0, t_f] \times \Omega \to [0, p_{\text{cap}}]$ *such that:*

$$\begin{cases} \dfrac{\partial p}{\partial t}(t, \boldsymbol{x}) = D_{O_2} \Delta p(t, \boldsymbol{x}) - g(p(t, \boldsymbol{x})), & \forall (t, \boldsymbol{x}) \in [t_0, t_f] \times \Omega, \\ p(t_0, \boldsymbol{x}) = p_0(\boldsymbol{x}), & \forall \boldsymbol{x} \in \Omega, \\ p(t, \boldsymbol{x}) = p_{\text{cap}}, & \forall (t, \boldsymbol{x}) \in [t_0, t_f] \times \Gamma_{\text{cap}}, \\ \dfrac{\partial p}{\partial \boldsymbol{n}}(t, \boldsymbol{x}) = 0, & \forall (t, \boldsymbol{x}) \in [t_0, t_f] \times \Gamma_{\text{out}}, \end{cases}$$

where p_0 *is the partial pressure at* t_0*. On the outer boundary of the domain,* Γ_{out}*, zero-flux Neumann conditions were imposed, while Dirichlet conditions with* $p = p_{\text{cap}}$ *were set on the capillary walls,* Γ_{cap}*.*

Although real tumors present heterogeneous values on the partial pressure for different capillaries, a constant $p_{\text{cap}} = 40$ mmHg is the typical value used in the literature [37, 84, 94, 95]. Similarly, oxygen diffusion properties are not homogeneous within tumor tissue, however a constant diffusion coefficient $D_{O_2} = 2 \times 10^3$ μm^2 s^{-1} is usually accepted [94, 95].

2.2.4 Numerical solution: FEM

In this study, the oxygenation problem 2.1 was solved by the FEM using a MATLAB (The Mathworks Inc., Natick, MA) solver from the Partial Differential Equation Toolbox (version 3.9 (R2022b)). This section presents the theoretical framework for the application of the FEM. The fundaments of the use of the FEM for time-dependent problems can be found in the literature [98].

Equation (2.8) can be turned into its integral form by constructing the weak formulation. Let v be a test function in the space $\mathcal{V} = \{v \in H^1(\Omega)/v|_{\Gamma_{\text{cap}}} = 0\}$. Multiplying equation (2.8) by v, it follows:

$$\frac{\partial p}{\partial t}(t, \boldsymbol{x}) v(\boldsymbol{x}) = D_{O_2} \Delta p(t, \boldsymbol{x}) v(\boldsymbol{x}) - g(p(t, \boldsymbol{x})) v(\boldsymbol{x}).$$

Then, integrating the above equation over Ω yields:

$$\int_\Omega \frac{\partial p}{\partial t}(t, \boldsymbol{x}) v(\boldsymbol{x}) d\Omega = \int_\Omega D_{O_2} \Delta p(t, \boldsymbol{x}) v(\boldsymbol{x}) d\Omega - \int_\Omega g(p(t, \boldsymbol{x})) v(\boldsymbol{x}) d\Omega,$$

where the Green's theorem can be applied to the second term, obtaining:

$$\int_\Omega \frac{\partial p}{\partial t}(t,\boldsymbol{x})v(\boldsymbol{x})d\Omega = -\int_\Omega D_{\mathrm{O}_2}\nabla p(t,\boldsymbol{x})\cdot\nabla v(\boldsymbol{x})d\Omega + \int_\Gamma D_{\mathrm{O}_2}\frac{\partial p}{\partial \boldsymbol{n}}(t,\boldsymbol{x})v(\boldsymbol{x})d\Gamma - \int_\Omega g(p(t,\boldsymbol{x}))v(\boldsymbol{x})d\Omega.$$

Also notice that, as $v = 0$ on Γ_{cap} and $\frac{\partial p}{\partial \boldsymbol{n}} = 0$ on Γ_{out}, it follows:

$$\int_\Gamma D_{\mathrm{O}_2}\frac{\partial p}{\partial \boldsymbol{n}}(t,\boldsymbol{x})v(\boldsymbol{x})d\Gamma = \int_{\Gamma_{\mathrm{cap}}} D_{\mathrm{O}_2}\frac{\partial p}{\partial \boldsymbol{n}}(t,\boldsymbol{x})v(\boldsymbol{x})d\Gamma_{\mathrm{cap}} + \int_{\Gamma_{\mathrm{out}}} D_{\mathrm{O}_2}\frac{\partial p}{\partial \boldsymbol{n}}(t,\boldsymbol{x})v(\boldsymbol{x})d\Gamma_{\mathrm{out}} = 0.$$

Then, for D_{O_2} constant, it results:

$$\int_\Omega \frac{\partial p}{\partial t}(t,\boldsymbol{x})v(\boldsymbol{x})d\Omega = -D_{\mathrm{O}_2}\int_\Omega \nabla p(t,\boldsymbol{x})\cdot\nabla v(\boldsymbol{x})d\Omega - \int_\Omega g(p(t,\boldsymbol{x}))v(\boldsymbol{x})d\Omega.$$

From the previous considerations, the oxygenation problem 2.1 can be redefined as the following variational problem:

Problem 2.2. *Find a function $p(t,\cdot)$ for $t \in [t_0, t_{\mathrm{f}}]$ on $\mathcal{V} = \{v \in H^1(\Omega)/v|_{\Gamma_{\mathrm{cap}}} = 0\}$ such that $p(t_0,\boldsymbol{x}) = p_0(\boldsymbol{x})$, and $\forall v \in \mathcal{V},\ t \in (t_0, t_{\mathrm{f}})$:*

$$\int_\Omega \frac{\partial p}{\partial t}(t,\boldsymbol{x})v(\boldsymbol{x})d\Omega + D_{\mathrm{O}_2}\int_\Omega \nabla p(t,\boldsymbol{x})\cdot\nabla v(\boldsymbol{x})d\Omega + \int_\Omega g(p(t,\boldsymbol{x}))v(\boldsymbol{x})d\Omega = 0.$$

The notation can be simplified by defining $p(t,\cdot) = p(t)$ and introducing the scalar product in $L^2(\Omega)$, and the bilinear form $a(v,w)$ for $v, w \in \mathcal{V}$ as:

$$\langle v, w\rangle_{L^2(\Omega)} = \int_\Omega v(\boldsymbol{x})w(\boldsymbol{x})d\Omega,$$

$$a(v,w) = \int_\Omega \nabla v(\boldsymbol{x})\cdot\nabla w(\boldsymbol{x})d\Omega.$$

Moreover, as neither Ω nor v depends on t, it follows:

$$\int_\Omega \frac{\partial p}{\partial t}(t,\boldsymbol{x})v(\boldsymbol{x})d\Omega = \frac{d}{dt}\int_\Omega p(t,\boldsymbol{x})v(\boldsymbol{x})d\Omega.$$

Thus, the weak formulation in Problem 2.2 is rewritten as: find $p : [t_0, t_{\mathrm{f}}] \to \mathcal{V}$ such that $p(t_0) = p_0$ and $\forall v \in \mathcal{V}, t \in (t_0, t_{\mathrm{f}})$:

$$\frac{d}{dt}\langle p(t), v\rangle_{L^2(\Omega)} + D_{\mathrm{O}_2}a(p(t), v) + \langle g(p(t)), v\rangle_{L^2(\Omega)} = 0.$$

Regarding the discretization in the spatial coordinate, to apply the FEM the infinite-dimensional space $\mathcal{V}$ is approximated by a finite-dimensional subspace $\mathcal{V}_h$, so it is sufficient to find $p_h : [t_0, t_\mathrm{f}] \to \mathcal{V}_h$ such that $p_h(t_0) = p_{0,h}$, where $p_{0,h} \in \mathcal{V}_h$ is an approximation of the initial solution p_0, and $\forall v_h \in \mathcal{V}_h, t \in (t_0, t_\mathrm{f})$:

$$\frac{d}{dt}\langle p_h(t), v_h\rangle_{L^2(\Omega)} + D_{\mathrm{O}_2} a(p_h(t), v_h) + \langle g(p_h(t)), v_h\rangle_{L^2(\Omega)} = 0.$$

Let $\{\phi_i\}_{1\leq i\leq N}$ be a basis for the finite-dimensional space $\mathcal{V}_h$. Then, the approximate solution and initial condition can be written as:

$$p_h(t) = \sum_{i=1}^{N} P_i^h(t)\,\phi_i, \quad p_{0,h} = \sum_{i=1}^{N} P_i^{0,h}(t)\,\phi_i,$$

where $P^h = (P_i^h)_{1\leq i\leq N}$ and $P^{0,h} = (P_i^{0,h})_{1\leq i\leq N}$ are the coordinates vectors of p_h and $p_{0,h}$, respectively.

Subsequently, values of $(P_i^h)_{1\leq i\leq N}$ and $(P_i^{0,h})_{1\leq i\leq N}$ must be found, such that $P_j^h(t_0) = P_j^{0,h}$ for $1 \leq j \leq N$, and:

$$\sum_{i=1}^{N}\langle\phi_i,\phi_j\rangle_{L^2(\Omega)}\frac{dP_i^h(t)}{dt} + D_{\mathrm{O}_2}\sum_{i=1}^{N} a(\phi_i,\phi_j)P_i^h(t) + \langle g\left(\sum_{i=1}^{N} P_i^h(t)\phi_i\right),\phi_j\rangle_{L^2(\Omega)} = 0.$$

Introducing the mass matrix, $\mathcal{M}_h$, and stiffness matrix, $\mathcal{K}_h$, defined by:

$$(\mathcal{M}_h)_{i,j} = \langle\phi_i,\phi_j\rangle_{L^2(\Omega)}, \quad (\mathcal{K}_h)_{i,j} = a(\phi_i,\phi_j),$$

for $1 \leq i, j \leq N$, the weak formulation is equivalent to the system:

$$\begin{cases} \mathcal{M}_h\dfrac{dP^h}{dt}(t) + D_{\mathrm{O}_2}\mathcal{K}_h P^h(t) + b^h(t) = 0, \quad \forall t \in (t_0, t_\mathrm{f}), \\ P^h(t_0) = P^{0,h}, \end{cases}$$

being:

$$b^h(t) = \langle g\left(\sum_{i=1}^{N} P_i^h(t)\phi_i\right),\phi_j\rangle_{L^2(\Omega)}.$$

Lastly, the problem is fully discretized in time-space by using a finite difference method, such as the forward Euler scheme (2.6), having:

$$\mathcal{M}_h\frac{P^{h,k+1} - P^{h,k}}{\Delta t} + D_{\mathrm{O}_2}\mathcal{K}_h P^h(t^k) + b^h(t^k) = 0,$$

where Δt is the time step of the temporal discretization for the interval $[t_0, t_\mathrm{f}]$.

The FEM is characterized by three elements: a partition/triangulation of the domain Ω, τ; a set of points obtained from the partition named *nodes*, Σ; and the basis functions $\{\phi_i\}_{1\leq i\leq N}$.

A partition τ divides Ω in a finite number, N, of subdomains, T_i, such as $\forall T_i \in \tau$:

- T_i is closed and its interior set $\mathring{T}_i \neq \varnothing$ is connected.
- The boundary is Lipschitz continuous.
- $\overline{\Omega} = \cup_{T_i\in\tau} Ti$.
- If $T_i \neq T_j$, then $\mathring{T}_i \cap \mathring{T}_j = \varnothing$.
- The intersection of two elements is a common vertex or edge.

The MATLAB mesh generator was used to obtain a partition of triangles. Each vertex of the triangles is a node, b_i, and the pair (τ, Σ), where $\Sigma = \{b_i\}_{1\leq i\leq N}$, is the mesh of finite elements. Furthermore, the basis functions were constructed by using first-order finite Lagrange elements, verifying:

- Each ϕ_i is continuous and bounded.
- There is a basis function for each node.
- $\phi_i(b_j) = \delta_{ij}$, being δ the Kronecker delta, i.e., 1 if $i = j$ and 0 otherwise.
- The restriction of each ϕ_i to the element T_i is a first-order polynomial.

2.2.5 Modeling of metabolic oxygen consumption

The oxygen consumption rate due to cellular metabolic activity in equation (2.8) is usually modeled following the Michaelis-Menten kinetics form [93]:

$$g_{\text{met}}(p(t,\boldsymbol{x})) = g_{\max}\frac{p(t,\boldsymbol{x})}{k + p(t,\boldsymbol{x})}, \tag{2.9}$$

where $g_{\max}$ is the maximum oxygen metabolic cosumption rate, and k is the oxygen pressure for half-maximum metabolic consumption rate. Typically, parameter values are set to $g_{\max} = 15$ mmHg and $k = 2.5$ mmHg, based on experimental studies [94].

For the geometry depicted in Figure 2.1, the steady-state solution of the oxygenation problem 2.1 with the consumption term given by equation (2.9) is shown in Figure 2.2.

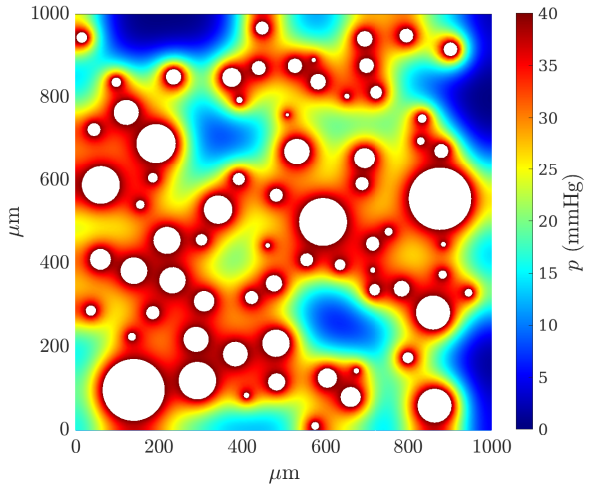

Figure 2.2: Steady-state solution of the oxygenation problem 2.1 with the consumption term given by equation (2.9) for the tumor geometry shown in Figure 2.1.

2.2.6 Modeling of Radiolytic Oxygen Depletion (ROD) in conv-RT and FLASH-RT

As mentioned in the previous chapter, radiation promotes oxygen depletion caused by the radiolysis of water molecules. Many studies have investigated oxygen depletion patterns both with conv-RT and FLASH-RT in different solutions simulating cellular compounds [99–101]. These works suggest that the depleted oxygen depends on the initial oxygen partial pressure and shows a pronounced curvature in the depletion pattern as the oxygen pressure approaches zero. Besides, Cao *et al.* [78] conducted *in vivo* experiments and found that oxygen depletion does not depend on the radiation dose rate at UHDRs within the 50–300 Gy s^{-1} range, but only on the radiation dose.

In this context, previous works [84, 100] have proposed a Michaelis-Menten kinetics to describe ROD as:

$$g_{\mathrm{ROD}}(p(t,\boldsymbol{x})) = \frac{D}{T}\frac{G_0\ p(t,\boldsymbol{x})}{k_{\mathrm{ROD}} + p(t,\boldsymbol{x})}, \tag{2.10}$$

where D (Gy) is the radiation dose, T (s) the total time of irradiation, G_0 (mmHg Gy^{-1}) the radiolytic consumption rate, and k_{ROD} (mmHg) the oxygen pressure for half-maximum oxygen depletion.

As mentioned in the previous chapter, ROD has not been observed in *in vivo* experiments with conv-RT, as the tumor vascular system continuously resupplies oxygen, preventing measurable oxygen depletion at conventional dose rates.

The left panel of Figure 2.3 shows oxygen depletion curves for both conventional (0.1 Gy s^{-1}) and UHDRs (100 Gy s^{-1}) at different oxygen statuses obtained by solving Problem 2.1 with metabolic and radiolytic consumption terms, respectively given by equations (2.9) and (2.10). As discussed, oxygen remains constant during conv-RT, while it is progressively eliminated in FLASH-RT. Moreover, the right panel of Figure 2.3 shows the transition of the oxygenation histogram belonging to Figure 2.1 from the beginning to the end of delivering 20 Gy with FLASH-RT (100 Gy s^{-1}).

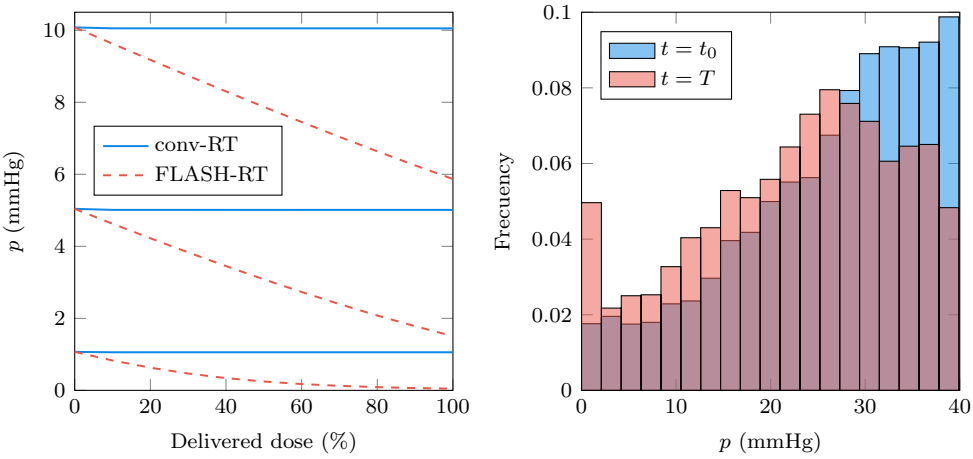

Figure 2.3: Oxygen depletion during conventional RT (conv-RT) (0.1 Gy s^{-1}) and FLASH-RT (100 Gy s^{-1}) for a delivered dose of 20 Gy and the geometry depicted at Figure 2.1. The left panel shows the depletion curves for both modalities at different initial oxygen partial pressures, p. The right panel shows the change in oxygenation histograms from the beginning ($t = t_0$) to the end ($t = T$) of FLASH-RT. These results were obtained by using the parameter values given in previous sections, along with $G_0 = 0.25$ mmHg Gy^{-1} and $k_{\mathrm{ROD}} = 1$ mmHg.

In this context, the oxygenation problem 2.1 in FLASH-RT is as follows:

Problem 2.3. *Find* $p : [t_0, t_f] \times \Omega \to [0, p_{\mathrm{cap}}]$ *such that:*

$$\begin{cases} \dfrac{\partial p}{\partial t}(t, \boldsymbol{x}) = D_{\mathrm{O}_2} \Delta p(t, \boldsymbol{x}) - g_{\mathrm{met}}(p(t, \boldsymbol{x})) - g_{\mathrm{ROD}}(p(t, \boldsymbol{x})), & \forall (t, \boldsymbol{x}) \in [t_0, t_f] \times \Omega, \\ p(t_0, \boldsymbol{x}) = p_0(\boldsymbol{x}), & \forall \boldsymbol{x} \in \Omega, \\ p(t, \boldsymbol{x}) = p_{\mathrm{cap}}, & \forall (t, \boldsymbol{x}) \in [t_0, t_f] \times \Gamma_{\mathrm{cap}}, \\ \dfrac{\partial p}{\partial \boldsymbol{n}}(t, \boldsymbol{x}) = 0, & \forall (t, \boldsymbol{x}) \in [t_0, t_f] \times \Gamma_{\mathrm{out}}, \end{cases}$$

where $g_{\mathrm{met}}(p)$ *and* $g_{\mathrm{ROD}}(p)$ *are given by equations (2.9) and (2.10), respectively.*

Problem 2.3 is a particular case of a semilinear parabolic problem with mixed boundary conditions. The existence of a unique solution for these types of systems has been studied in the classical literature [102].

Because of the reasons mentioned before, in conv-RT, the oxygenation problem can be simplified to its steady-state form, ignoring the effect of ROD:

Problem 2.4. *Find* $p : \Omega \to [0, p_{\text{cap}}]$ *such that:*

$$\begin{cases} D_{\text{O}_2} \Delta p(\boldsymbol{x}) = g_{\text{met}}(p(\boldsymbol{x})), & \forall \boldsymbol{x} \in \Omega, \\ p(\boldsymbol{x}) = p_{\text{cap}}, & \forall \boldsymbol{x} \in \Gamma_{\text{cap}}, \\ \dfrac{\partial p}{\partial \boldsymbol{n}}(\boldsymbol{x}) = 0, & \forall \boldsymbol{x} \in \Gamma_{\text{out}}, \end{cases}$$

where $g_{\text{met}}(p)$ *is given by equation (2.9).*

2.2.7 Implementation details

Building on the work of Díaz-Botana [92] in conv-RT, a MATLAB code was developed to calculate the numerical solution of the oxygenation problems 2.3 and 2.4. Particularly, the original code was updated to remove deprecated functions from previous MATLAB versions (such as `initmesh` and `refinemesh` to generate the mesh, and `pdenonlin` to solve the problem) and adapt it to the R2022b version, and expanded to include the effect of ROD in FLASH-RT.

Firstly, the geometry of the problem is created through a user-defined function `createGeometry` that takes as input: the VF, the side length of the squared domain, and the parameters given in Table 2.1 to generate the capillaries. This function follows the steps given in Section 2.2.2 and gives as output the decomposed geometry matrix and a vector with the radius of the capillaries. The decomposed geometry matrix contains a representation of the geometry in terms of disjointed minimal regions constructed by the `decsg` MATLAB algorithm. In this case, each column in the matrix belongs to a line or circle edge segment.

Then, the MATLAB function `createpde` is used to create a model object that contains information about the PDE which defines the problem: number of equations, geometry, mesh, and boundary conditions. The generated geometry is associated with a one-equation model object through the MATLAB function `geometryFromEdges`, which requires as inputs the model object and the decomposed geometry matrix. Subsequently, the MATLAB function `generateMesh` creates the mesh to apply the FEM. In this thesis, the minimum and maximum length of mesh edges were constrained within the range 1–10 μm. Besides, the geometric order of the finite elements was specified to be linear, i.e., the nodes are the vertex of the triangles. Further analysis of the mesh suitableness to solve the oxygenation problem is presented in Appendix A. Listing 2.1 shows the code to perform the above process, where `geom` is

a vector containing the parameter values to create de geometry, previously detailed; `dl` is the decomposed geometry matrix; and `R` is the radius vector.

```
%Create geometry
[dl, R] = createGeometry(geom);
%Create PDE model
model = createpde;
%Assign geometry to model
geometryFromEdges(model,dl);
%Create mesh
generateMesh(model,'Hmin',1,'Hmax',10,'GeometricOrder','linear');
```

Listing 2.1: Code to create the geometry of the problem, the PDE model object, and the mesh.

Once the geometry and the mesh are created, the boundary and initial conditions are defined in the PDE model object. Regarding the boundary conditions, the minimal regions in the decomposed geometry matrix must be assigned to the outer or the capillary boundary. The corresponding columns in `dl` are respectively stored in the vectors `id_out` and `id_cap`. Zero-flux Neumann conditions are imposed in line edges and Dirichlet conditions with $p = 40$ mmHg are set on circle segments by using the MATLAB function `applyBoundaryCondition`, as shown in Listing 2.2.

```
%Set Neumann conditions on the outer boundary
applyBoundaryCondition(model,'neumann','Edge',id_out,'g',0,'q',0);
%Set Dirichlet conditions on the capillary walls
applyBoundaryCondition(model,'dirichlet','Edge',id_cap,'u',40);
```

Listing 2.2: Code to set the boundary conditions to solve Problems 2.3 and 2.4.

To solve Problem 2.3, the initial condition is set to $p_0(t_0) = \mathbf{0}$ through the MATLAB function `setInitialConditions`, as shown in Listing 2.3.

```
%Set initial condition
setInitialConditions(model, 0);
```

Listing 2.3: Code to set the initial condition to solve Problem 2.3.

Finally, the MATLAB functions `specifycoefficients` and `solvepde` are used to set the PDE coefficients and solve Problems 2.3 and 2.4, as respectively shown in Listings 2.4 and 2.5.

```
%Specify coefficients: m*d^2p/d^2t + d*dp/dt - c*Lap(p) + a*p = f
aa = @(loc,st) acoeffun(loc,st,D,G0,T,k_ROD,g_max,k);
specifyCoefficients(model,'Face',1,'m',0,'d',1,'c',D,'a',aa,'f',0);
sol = solvepde(model,tlist);
```

```
function acoef = acoeffun(loc,st,D,G0,T,k_ROD,g_max,k)
    p = st.u;
    acoef = g_max*(1./(p+k)) + D/T*G0*(1./(p+k_ROD));
end
```

Listing 2.4: Code to define the PDE and solve Problem 2.3.

```
%Specify coefficients: m*d^2p/d^2t + d*dp/dt - c*Lap(p) + a*p = f
aa = @(loc,st) acoeffun(loc,st,g_max,k);
specifyCoefficients(model,'Face',1,'m',0,'d',0,'c',D,'a',aa,'f',0);
sol = solvepde(model);
```

```
function acoef = acoeffun(loc,st,g_max,k)
    p = st.u;
    acoef = g_max*(1./(p+k));
end
```

Listing 2.5: Code to define the PDE and solve Problem 2.4.

2.3 Model fitting and evaluation

This section summarizes some tools used in the process of fitting mathematical models to experimental data for validation. In this study, the Weighted Sum of Squared Differences (WSSD) was used to quantify the error of the fits of presented models to experimental data from the literature. Furthermore, the Akaike Information Criterion (AIC) was employed to compare models and select the best balance between its complexity (number of parameters) and the goodness-of-fit to the data. Lastly, the Simulated Annealing (SA) optimization algorithm was used to identify the best-fitting parameters for each model.

2.3.1 Measurement of the error in model fitting

The WSSD was used as a metric to assess the differences between predicted values and observed data. For a collection of n experimental data points $\{y_i, i = 1 \dots n\}$, the predicted values $\{\hat{y}_i, i = 1 \dots n\}$, and the experimental uncertainties, $\{z_i, i = 1 \dots n\}$, the WSSD is:

$$WSSD = \sum_{i=1}^{n} \frac{(\hat{y}_i - y_i)^2}{z_i^2}. \tag{2.11}$$

A smaller WSSD indicates a better fit of the model to the data.

2.3.2 Akaike Information Criterion (AIC)

The AIC is used to compare models by evaluating their complexity and goodness-of-fit to observed data. This methodology ranks models according to the likelihood of the fit, L, and the number of free parameters, k. The model with the lower AIC is considered to be the best-fitting model. It is calculated as follows:

$$AIC = -2\log(L) + 2k. \tag{2.12}$$

When the number of observed data points, n, is small compared to the number of parameters in the model, the AIC with sample size correction [103] is preferred:

$$AIC = -2\log(L) + 2k + \frac{2k(k+1)}{n-k-1}. \tag{2.13}$$

This variation is particularly useful to avoid potential bias in model selection. The correction term penalizes models with a large number of parameters relative to the sample size, preventing overfitting or selecting overly complex models.

2.3.3 Simulated Annealing (SA) algorithm

The SA algorithm [104] was utilized to fit tumor response models to preclinical data of tumor volume evolution after RT treatments. The SA is a stochastic optimization technique that approximates the global optimum and can escape sub-optimal solutions in non-convex problems. This algorithm simulates the annealing process in metallurgy, where a material is slowly cooled to minimize its energy and achieve a stable state. Similarly, in the context of this research, SA iteratively and stochastically explores the parameter space, allowing the algorithm to escape local optima and converge towards the global optimal parameters that best describe the experimental data.

Consider $f_{\boldsymbol{p}} = f(p_1, \ldots, p_k)$ the expression that describes the state of a system through a vector of k parameters $\boldsymbol{p} = (p_1, \ldots, p_k)$. The following optimization problem can be formulated:

Problem 2.5. *Find the best-fitting parameters, $\boldsymbol{p}_{\mathrm{b}}$, which minimize a fitting function, $c(\boldsymbol{p})$, which is interpreted as the cost of the solution $\boldsymbol{p}$.*

Given an initial vector of parameter values, $\boldsymbol{p}^{(0)}$, the SA iteratively generates new candidates for best-fitting parameters, $\boldsymbol{p}^{(j)}$ through a *neighboring function*. A variable, T, known as the temperature, is used to obtain progressively smaller perturbations as the algorithm converges to a solution. Thus, given an initial temperature, T_0, its value is iteratively decreased according to a step, $\Delta_{\mathrm{T}} \in (0, 1)$, i.e., $T^{(j+1)} = \Delta_{\mathrm{T}} T^{(j)}$.

A *fitting function*, for example, that given in equation (2.11), is computed to obtain the cost of new candidates $c\left(\boldsymbol{p}^{(j)}\right)$. New candidates are accepted as a new state, $(\tilde{\boldsymbol{p}}, \tilde{c})$, under certain circumstances. On the one hand, if the cost is lower than the current

one, $\left(\boldsymbol{p}^{(j)}, c\left(\boldsymbol{p}^{(j)}\right)\right)$ is accepted as the new state. On the other hand, to escape local minima and explore a broader region of the solution space, the SA algorithm also accepts non-optimal solutions under a certain *survival probability*, S, which becomes lower as T decreases:

$$S\left(\boldsymbol{p}^{(j)}, T^{(j)}\right) = \exp\left(\frac{\tilde{c} - c\left(\boldsymbol{p}^{(j)}\right)}{T^{(j)}}\right). \tag{2.14}$$

This process is repeated until solving Problem (2.5) according to a selected *stopping criteria*. In this study, a maximum number of iterations, n_{T}, was set. Moreover, for each iteration $j = 1 \dots n_{\mathrm{T}}$, n_{it} subiterations were performed with the same T. In the end, only optimal solutions can be accepted as best-fitting parameters, $\boldsymbol{p}_{\mathrm{b}}$.

New candidates for best-fitting parameters are generated by perturbating the current state $\tilde{\boldsymbol{p}}$. On each iteration, one of the optimal parameters, $\tilde{p}_k$, is randomly selected and perturbated through the neighboring function:

$${p_k}^{(j)} = \tilde{p}_k \left(1 + r\sqrt{T^{(j)}/T_0}\right), \tag{2.15}$$

where $r \in (-a, a)$, for $a < 1$ given, is obtained from the uniform distribution.

Figure 2.4 shows the flowchart of the SA algorithm, detailed in the next steps:

Step 1: Set the initial temperature, T_0; the maximum number of iterations for the stopping criteria, n_{T}; and the initial parameter values $\boldsymbol{p}^{(0)}$.

Step 2: Initialize $j = 1$ ($j = 1 \dots n_{\mathrm{T}}$), $T^{(j)} = T_0$.

Step 3: Obtain $c\left(\boldsymbol{p}^{(0)}\right)$, for example from equation (2.11).

Step 4: Initialize $\tilde{\boldsymbol{p}} = \boldsymbol{p}^{(0)}$, $\tilde{c} = c\left(\boldsymbol{p}^{(0)}\right)$, $\boldsymbol{p}_{\mathrm{b}} = \boldsymbol{p}^{(0)}$ and $c_{\mathrm{b}} = c\left(\boldsymbol{p}^{(0)}\right)$.

Step 5: Generate a new candidate to best-fitting parameters, $\boldsymbol{p}^{(j)}$, by using equation (2.15), and compute $c\left(\boldsymbol{p}^{(j)}\right)$.

Step 6: If $c\left(\boldsymbol{p}^{(j)}\right) < c_{\mathrm{b}}$, then update $\boldsymbol{p}_{\mathrm{b}} = \boldsymbol{p}^{(j)}$ and $c_{\mathrm{b}} = c\left(\boldsymbol{p}^{(j)}\right)$.

Step 7: If $c\left(\boldsymbol{p}^{(j)}\right) < \tilde{c}$, then update $\tilde{\boldsymbol{p}} = \boldsymbol{p}^{(j)}$ and $\tilde{c} = c\left(\boldsymbol{p}^{(j)}\right)$, and go to Step 9. Otherwise, continue with Step 8.

Step 8: Being $r' \in (0, 1)$ obtained from a uniform distribution and $S\left(\boldsymbol{p}^{(j)}, T^{(j)}\right)$ the survival probability given by equation (2.14); if $r' < S\left(\boldsymbol{p}^{(j)}, T^{(j)}\right)$, then update $\tilde{\boldsymbol{p}} = \boldsymbol{p}^{(j)}$ and $\tilde{c} = c\left(\boldsymbol{p}^{(j)}\right)$.

Step 9: Update $T^{(j+1)} = \Delta_{\mathrm{T}} T^{(j)}$ and $j \to j + 1$.

Step 10: Check the stopping criteria: if $j > n_{\mathrm{T}}$, then finish the algorithm; otherwise, go back to Step 5.

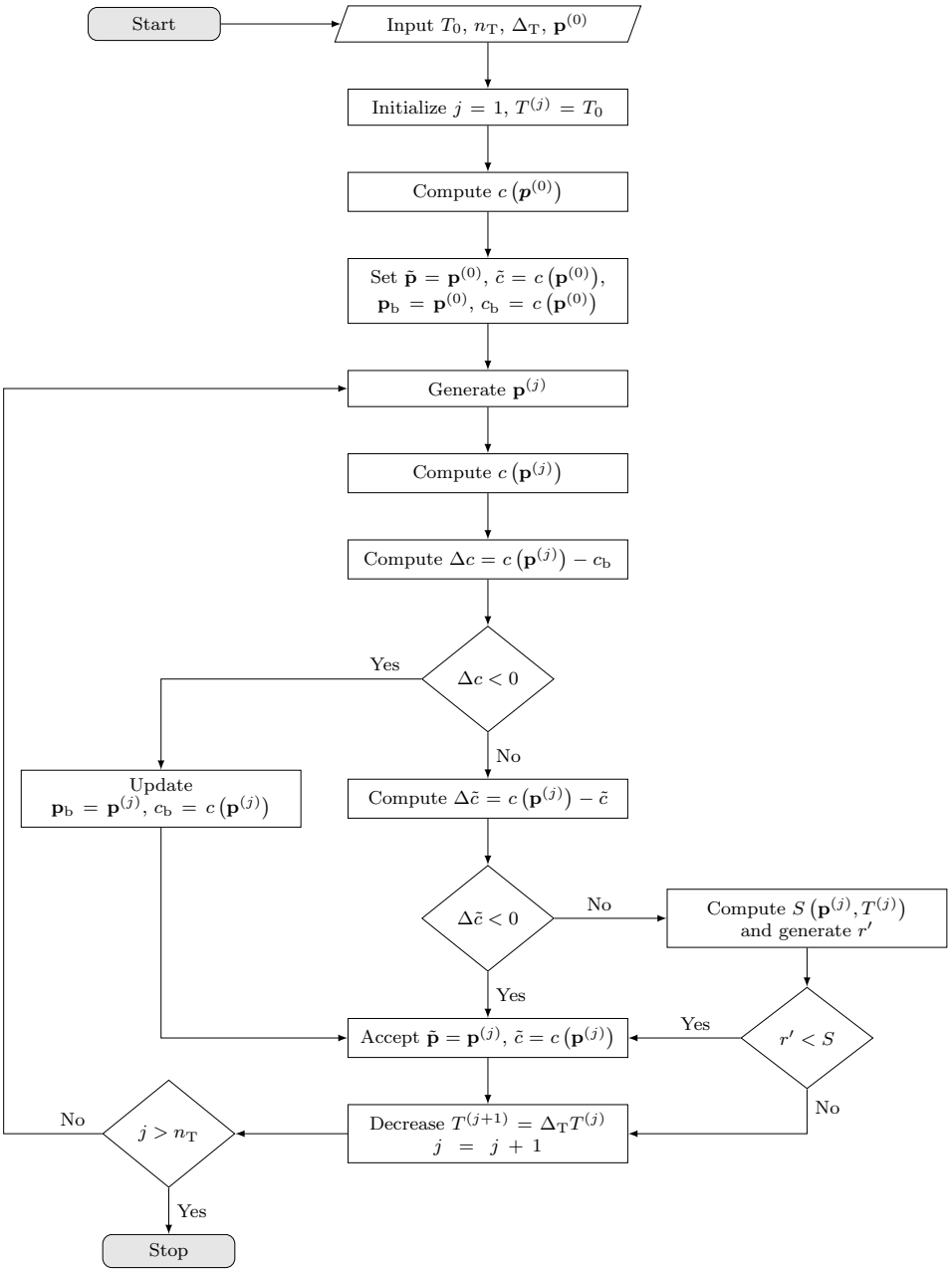

Figure 2.4: Flowchart of the Simulated Annealing (SA) algorithm.

Chapter 3

Results on radioimmunotherapy

"We are only as strong as we are united, as weak as we are divided."
— Albus Dumbledore, *Harry Potter and the Goblet of Fire.*

This chapter summarizes the outcomes achieved during the thesis on developing mathematical models for radioimmunotherapy. This innovative antitumor treatment aims to exploit the synergy between radiation and immune system enhancement through immunotherapy drugs. Conventional radiotherapy models, like the LQ model, cannot fully explain cell death mechanisms in radioimmunotherapy. Consequently, a differential model is presented to describe tumor volume evolution in preclinical radioimmunotherapy studies, allowing the formulation of hypotheses about optimal treatment combinations and administration schedules.

This chapter partially reproduces the content of the article: I. González-Crespo, A. Gómez-Caamaño, Ó. López Pouso, J. D. Fenwick, and J. Pardo-Montero, "A biomathematical model of tumor response to radioimmunotherapy with αPDL1 and αCTLA4," *IEEE/ACM Transactions on Computational Biology and Bioinformatics*, vol. 20, no. 2, pp. 808–21, 2023. DOI: 10.1109/TCBB.2022.3174454.

3.1 Overview of the problem

Cancer ImmunoTherapy (IT) is a therapeutic strategy that aims at boosting and exploiting the natural immune response to control and cure tumors. Particularly, Immune Checkpoint Inhibitors (ICIs), such as αCTLA4 and αPD(L)1 drugs (see Section 1.4.1), are used to treat several cancers, including melanoma, prostate, non-small cell lung cancer, and leukemia [105, 106]. ICIs block different proteins, like the CTLA-4 receptor and those involved in the PD-1/PD-L1 pathway, which are well-known suppressors of the immune response against tumors. These ITs have shown promising results in preclinical experiments, and there are several monoclonal antibodies against CTLA-4 and PD-(L)1 approved to treat different types of cancer [107]. However, the efficacy of IT as a cancer treatment by itself is still limited, except for particular cases. For example, *ipilimumab* (αCTLA4) has shown an improvement in the survival of melanoma patients, but with low response rates, within the 10–15% range [108].

Many preclinical studies have shown that RadioImmunoTherapy (RIT) combined treatments, in particular with inhibitors of CTLA-4 and PD-(L)1, are significantly more effective than RT and IT as monotherapies [7, 18, 29, 59, 109]. Although the dominant mechanism behind the effect of RT is the direct damage on tumor cells' DNA [110], there is evidence that radiation can trigger other indirect cell-death mechanisms, particularly at high-doses-per-fraction treatments, which may influence the synergy with IT. High radiation doses may promote an immune response against surviving tumor cells [28, 29, 111], increasing tumor control. These immune effects seem to be related to an increased release of tumor antigens due to radiation-mediated cell death, which enhances the activation of antitumor T-cells; and modifications of the Tumor MicroEnvironment (TME), such as the elimination of immune down-regulators like regulatory T-cells (Tregs) and Myeloid-Derived Suppressor Cells (MDSCs), facilitating T-cell infiltration in the tumor [7, 50, 112].

Despite the demonstrated effectiveness of RIT, how the best combination of both therapies can be achieved is still a matter of study. In this regard, validated tumor response models to RIT constitute a powerful tool to investigate the biological mechanisms behind the effect of the treatment, and may also assist in the design of optimal therapeutic strategies, potentially guiding clinicians in the selection of optimal treatments. Modeling the response of tumors to IT has been addressed in the biomathematical literature, following both phenomenological and mechanistic approaches [113–119]. On the contrary, modeling the synergistic effect of RIT has been less studied due to the novelty of this treatment strategy, but it has become an active field of research over the last few years [34, 35, 120–123]. For example, Serre *et al.* [34, 120] proposed a simple response model to RIT with αCTLA4 and αPD(L)1 ICIs that was fitted to experimental data of tumor response and rejection probability of implanted tumors. Besides, Kosinsky *et al.* [121] presented a more complex model, based on ODEs, which was fitted to experimental data and used to formulate hypotheses of optimal treatment strategies with RT and inhibitors of PD-L1.

3.2 Model of tumor response to RIT

This section presents a mathematical model of tumor response to RIT with ICIs against the CTLA-4 receptor and the PD-1/PD-L1 pathway. The model has been tested by fitting it to preclinical data of tumor response to combined therapies of radiation with different fractionations along with αPDL1 or αCTLA4 [18, 59], including volume dynamics and tumor control rates.

The dynamics of the most relevant cell populations are described by ODEs, DDEs and IDEs. On the one hand, DDEs explicitly include biological response delays on cell dynamics, which may have importance when modeling biological systems. On the other hand, IDEs describe the effect of the treatment at the delivery times, introducing changes in cell populations through impulses.

The model is presented as a continuous deterministic model to describe tumor volumes. However, when modeling TCP, it is converted into a discrete stochastic model by introducing a birth-death Markov chain. This allows the model to yield TCPs according to the clonogenic cells hypothesis, introduced in Section 1.3.4.

3.2.1 Overview of the model

The proposed biomathematical model follows the cancer-immunity cycle, described in Section 1.4.1. In summary, tumor cells release antigens, both naturally and due to cell death; antigens are taken by APCs to activation sites (lymph nodes) where they trigger T-cell activation; active T-cells migrate to the tumor, infiltrate it, and eliminate tumor cells. Each RT dose fraction damages and eliminates tumor cells (contributing to the release of antigens), as well as T-cells present in the tumor. IT drugs affect either the activation of T-cells (αCTLA4) or the immune-mediated death of tumor cells by activated T-cells (αPD(L)1).

A diagram of the variables of the model and the interaction between them is shown in Figure 3.1. The model includes three main species: tumor cells, T-cells, and antigens/APCs. These species are split into six compartments, which exist in two different spatial locations: in the tumor (viable cancer cells, C; tumor cells that are doomed by radiation and will eventually die, C_d; and active T-cells against tumor cells, T_a), and in the activation sites (a phenomenological compartment accounting for the effects of antigens and APCs, $\hat{A}$; the T-cell pool, $\hat{T}$; activated T-cells, $\hat{T}_\mathrm{a}$; and blocked T-cells through the CTLA-4 receptor, $\hat{T}_\mathrm{b}$). The compartments at the activation sites are identified with a hat ($\hat{}$) to facilitate the understanding of the model. Migration between different spatial locations (antigens/APCs migrating from the tumor to activation sites and activated T-cells migrating from the activation sites and infiltrating the tumor) results in biological delays which are explicitly included in the model through DDEs (see Section 2.1.2). The effect of radiation delivery on tumor cells and irradiated T-cells, as well as the administration of IT drugs, are modeled as impulses by using IDEs (see Section 2.1.1).

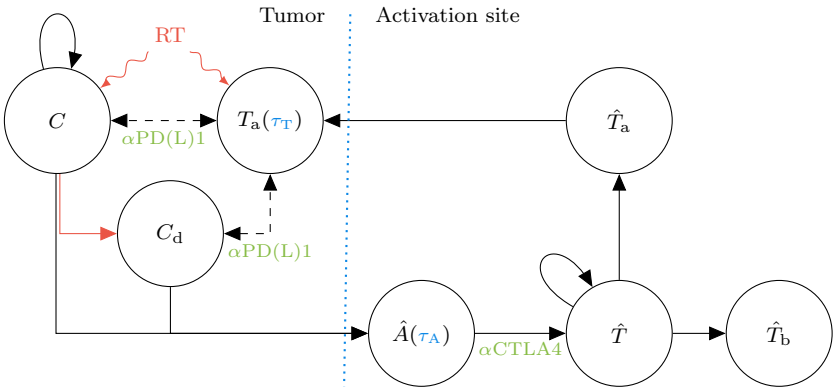

Figure 3.1: Flowchart of the model showing the interaction between different compartments: viable tumor cells (C), doomed tumor cells (C_d), active T-cells in the tumor (T_a), antigens/Antigen Presenting Cells (APCs) ($\hat{A}$), the pool of T-cells ($\hat{T}$), activated T-cells ($\hat{T}_a$) and blocked T-cells ($\hat{T}_b$). The dotted line shows the separation between compartments physically located in the tumor (left) and in the activation sites (right). The notation also distinguishes between the two locations, identifying the compartments within the activation zone with a hat ($\hat{}$). τ_A and τ_T are biological delays related to the migration of antigens and T-cells between those two physical locations. The action points of RadioTherapy (RT), anti-Programmed Death-(Ligand) 1 (αPD(L)1), and anti-CTLA-4 (αCTLA4) are also indicated.

The model dynamics has the following form:

$$\begin{aligned}
\text{dynamics } C &= \text{proliferation} - \text{radiation death} - \text{immune death (PD-(L)1)} \\
\text{dynamics } \hat{A} &= \text{natural release} + \text{RT-mediated release} - \text{natural elimination} - \\
&\quad \text{T-cell activation (CTLA-4)} \\
\text{dynamics } T_a &= \text{activation/infiltration (CTLA-4)} - \text{radiation death} - \\
&\quad \text{immune death} - \text{natural elimination}
\end{aligned}$$

The presented compartmental model attempts to describe the dynamics of the main agents involved in the tumor response to RIT. However, many simplifications were made to present a tractable problem. On the one hand, spatial coordinates were not considered, although a simple spatial dependency is indirectly introduced through biological delays simulating the migration processes between the tumor site and the T-cell activation zone. On the other hand, the process of T-cell infiltration within the tumor was not included in the model but integrated into the migration delay. Besides, immune-mediated death is overly simplified, as other cell types that participate in this process, either favoring immunity or acting as suppressors, like natural killers or Tregs, were not included. Regarding the effect of RT, the LQ model was used to account for radiation cell death, but departures from the LQ model were also studied and discussed.

3.2.2 Radiation cell death and tumor proliferation

Dose delivery is modeled as instantaneous, which seems a good approximation, as in typical fractionated treatments it takes minutes, while the typical times of the model dynamics are days. The LQ model (1.1), described in Section 1.3.1, is typically used to model radiation-mediated cell death through the calculation of the SF. However, as previously mentioned, it is well-known that cell death can depart from the standard LQ model, especially at high-dose-per-fraction treatments. As the model was fitted to data from different fractionation schedules, including hypofractionated RT, other LQ-derived models were investigated and compared to provide the best fits to experimental data. In particular, the LQL model (1.7) (described in Section 1.3.2) and a simple *ad hoc* modification of the quadratic term in the LQ model [33]:

$$\beta \to \beta \left(1 + c\sqrt{d}\right), \tag{3.1}$$

where c ($\mathrm{Gy}^{-1/2}$) is a free parameter and d (Gy) is the dose per fraction. Introducing the above modification in the parameter β of equation (1.1) results in the modified LQ ($\mathrm{LQ_{mod}}$) model:

$$SF = \exp\left(-\alpha d - \beta \left(1 + c\sqrt{d}\right) d^2\right). \tag{3.2}$$

Negative c values might be related to damage saturation effects, as sublethal damage repair in the LQL model, while positive values are linked to indirect cell death mechanisms contributing to cell killing.

The LQ, LQL, and $\mathrm{LQ_{mod}}$ models were used to describe radiation-induced tumor cell death. While radiation-induced T-cell death was described by using the LQ model.

Tumor cells lethally damaged by radiation (doomed) are not instantaneously removed from the system, but follow a given kinetics, generally a plateau (*mitotic delay*) followed by a progressive death as damaged cells enter mitosis and suffer mitotic catastrophe due to damage in their DNA. On the contrary, T-cells die in interphase within a few hours of irradiation (*apoptosis*), without intervening mitosis. The model considers a mitotic delay followed by an exponential death [37] in tumor cells and the immediate death of irradiated T-cells.

The proliferation of viable tumor cells is modeled by the logistic formalism [124], as tumor growth might be limited by different factors, like physical constraints due to its location or the lack of necessary nutrients. Moreover, while doomed cells may carry some proliferating capacity (*abortive divisions* [125]), it should be limited and not contribute to the long-term cell population. Therefore, it was not included in the model.

Being $\{t_i, i = 1 \dots n\}$ a collection of n radiation delivery times and $\{d_i, i = 1 \dots n\}$ the delivered fractions of dose, the following IDE describes the proliferation dynamics

and radiation effect on viable tumor cells:

$$\begin{aligned} \frac{dC}{dt}(t) &= \lambda_1 C(t)(1-\lambda_2 C_{\text{tot}}(t)), \quad \forall t \neq t_i, \\ \Delta C(t_i) &= (SF_{\text{C}}(d_i)-1)C(t_i), \qquad \forall t = t_i, \end{aligned} \tag{3.3}$$

where λ_1 (days^{-1}) is the exponential proliferation rate, λ_2 is a parameter related to the carrying capacity of the system, and $C_{\text{tot}}(t) = C(t) + C_{\text{d}}(t)$ is the total number of tumor cells at time t. Moreover, SF_{C} is the SF of tumor cells given by the LQ model (1.1), the LQL model (1.7) or the LQ_{mod} model (3.2).

Each radiation fraction is considered to create new doomed cells, but not to interfere with the radiation kinetics of existing ones. Therefore, the compartment of doomed cells is split into n subcompartments created by the n delivered dose fractions, having:

$$\begin{aligned} \frac{dC_{\text{d},i}}{dt}(t) &= -\phi\omega(\bar{t}_i)C_{\text{d},i}(t), \qquad \forall t \neq t_i, \\ \Delta C_{\text{d},i}(t_i) &= (1-SF_{\text{C}}(d_i))C(t_i), \quad \forall t = t_i, \\ C_{\text{d}}(t) &= \sum_{i=1}^{n} C_{\text{d},i}. \end{aligned} \tag{3.4}$$

Where, $C_{\text{d},i}(t)$ is the compartment of doomed cells created by the radiation dose fraction d_i, t_i the delivery time of that fraction, and $\bar{t}_i = t - t_i$. Notice that $C_{\text{d},i}(t)$ is defined as zero for $t < t_i$. The parameter ϕ (days^{-1}) is the death rate, and the function ω models the mitotic delay and progressive incorporation of damaged cells to cell death kinetics after a radiation fraction:

$$\omega(z) = \begin{cases} 0, & \text{for } z \leq \tau_{\text{d}1}, \\ \dfrac{z-\tau_{\text{d}1}}{\tau_{\text{d}2}-\tau_{\text{d}1}}, & \text{for } \tau_{\text{d}1} < z \leq \tau_{\text{d}2}, \\ 1, & \text{for } z > \tau_{\text{d}2}, \end{cases} \tag{3.5}$$

being $\tau_{\text{d}1}$ (days) and $\tau_{\text{d}2}$ (days) the initial and final instants of time describing the mitotic delay.

Regarding the radiation-mediated death of T-cells within the tumor, it follows:

$$\Delta T_{\text{a}}(t_i) = (SF_{\text{T}}(d_i)-1)T_{\text{a}}(t_i), \quad \forall t = t_i, \tag{3.6}$$

where SF_{T} is the SF of T-cells given by the LQ model (1.1). As previously mentioned, it is assumed that radiation-damaged T-cells die instantly, thus there are no kinetic terms associated with that process.

3.2.3 Antigen release and T-cell activation

Antigens are considered to be released both naturally, due to the presence of tumor cells (with a rate proportional to the number of both viable and doomed tumor cells), and as a result of radiation-induced cell death (proportional to the rate of doomed cell elimination). Besides, the model includes a term that describes their natural removal from the system. A biological delay, τ_{A} (days), between antigen release and T-cell activation accounts for the time that APCs take to collect antigens and carry them to the activation sites (see Figures 1.5 and 3.1), having:

$$\frac{d\hat{A}}{dt}(t) = \rho C_{\mathrm{tot}}(t-\tau_{\mathrm{A}}) + \ \psi\phi \sum_{i=1}^{n} \left(\omega(\overline{t_i-\tau_{\mathrm{A}}})C_{\mathrm{d,i}}(t-\tau_{\mathrm{A}})\right) - \sigma\hat{A}(t), \tag{3.7}$$

where ρ (days^{-1}) is the natural release rate, ψ is the cell-death-mediated release rate, $\overline{t_i-\tau_{\mathrm{A}}} = t-(t_i-\tau_{\mathrm{A}})$, and σ (days^{-1}) is the natural elimination rate. The funtion ω is given by equation (3.5) and ϕ is the death rate from equation (3.4).

The activation of T-cells against tumor cells is modeled through four bilinear equations, which describe the generation of activated T-cells ($\hat{T}_{\mathrm{a}}$) or blocked T-cells ($\hat{T}_{\mathrm{b}}$) (through the CTLA-4 receptor) from a pool of blank T-cells ($\hat{T}$):

$$\frac{d\hat{A}}{dt}(t) = -a\hat{A}(t)\hat{T}(t) - b\hat{A}(t)\hat{T}(t), \tag{3.8}$$

$$\frac{d\hat{T}}{dt}(t) = -a\hat{A}(t)\hat{T}(t) - b\hat{A}(t)\hat{T}(t) + h, \tag{3.9}$$

$$\frac{d\hat{T}_{\mathrm{a}}}{dt}(t) = a\hat{A}(t)\hat{T}(t), \tag{3.10}$$

$$\frac{d\hat{T}_{\mathrm{b}}}{dt}(t) = b\hat{A}(t)\hat{T}(t). \tag{3.11}$$

Parameters a (days^{-1}) and b (days^{-1}) describe the affinities for activation and inactivation, respectively [34]. Moreover, the amount of available blank T-cells decreases due to the activation/inactivation process, and it is renewed with a constant pool (due to maturation of new T-cells), h (days^{-1}). To prevent the T-cell compartment from unlimited growth, an initial condition was set, $\hat{T}(0) = T_0$, which serves also as a carrying capacity, imposing $\hat{T}(t) \leq T_0, \ \forall t$.

Active T-cells, $\hat{T}_{\mathrm{a}}$, migrate and infiltrate in the tumor with an associated biological delay τ_{T} (days), which models the time needed to move from the activation sites to the tumor zone and act on tumor cells. Once within the tumor, they become part of the compartment T_{a}, resulting in:

$$\frac{dT_{\mathrm{a}}}{dt}(t) = \frac{d\hat{T}_{\mathrm{a}}}{dt}(t-\tau_{\mathrm{T}}) = a\hat{A}(t-\tau_{\mathrm{T}})\hat{T}(t-\tau_{\mathrm{T}}). \tag{3.12}$$

To test the hypothesis that vascular damage at high radiation doses [11] may reduce the effectiveness of RIT by limiting the infiltration of T-cells in the tumor, a simple modulation factor was introduced on active T-cells within the tumor. This time-dependent term accounts for vascular damage and progressive recovery. Inspired by previous works [11, 95], critical vascular damage is considered for doses beyond 15 Gy, and the progressive recovery of the vascular function is modeled as:

$$f(t) = \min\{0.05(t - t'), 1\}, \tag{3.13}$$

where $t - t'$ is the recovery time since the last radiation dose delivered at $t = t'$, and 0.05 days^{-1} is the recovery rate [95]. This term represents the fraction of active T-cells reaching the tumor and multiplies the right side of equation (3.12).

3.2.4 Immnune-mediated cell death

Interaction between active T-cells and tumor cells within the tumor results in the partial depletion of both. Following the work of de Pillis *et al.* [113], this interaction is modeled with a bilinear term for the compartment T_{a}, in addition to an exponential natural elimination:

$$\frac{dT_{\mathrm{a}}}{dt}(t) = -\iota T_{\mathrm{a}}(t)C_{\mathrm{tot}}(t) - \eta T_{\mathrm{a}}(t), \tag{3.14}$$

where ι (days^{-1}) is the depletion rate due to cell competition and η (days^{-1}) is the natural elimination rate. On the other hand, immune-mediated death of viable tumor cells (analogous for $C_{\mathrm{d}}(t)$) is modeled by the following rational term:

$$\frac{dC}{dt}(t) = -p\frac{(T_{\mathrm{a}}(t)/C_{\mathrm{tot}}(t))^q}{s + (T_{\mathrm{a}}(t)/C_{\mathrm{tot}}(t))^q}C(t), \tag{3.15}$$

where p (days^{-1}) is the maximum depletion rate, q represents how the elimination rate depends on the effector/target ratio, and s modules the steepness of the immune-mediated-death curve.

Data fitting experiments of cell lysis data showed that while a simple bilinear term is sufficient to describe immune-mediated T-cell death, the elimination of tumor cells due to the interaction with immune cells is better described by a rational term like that in equation (3.15). The rational term allows for a saturation effect which may result from antigen-specific T-cells targeting a specific tumor cell type [113].

3.2.5 The effect of αPD(L)1 and αCTLA4

The biokinetics of αPD(L)1 and αCTLA4 ITs are included in the model through the variables p_1 and c_4, which represent the concentration of the respective drugs in the system. The administration is modeled as instantaneous source terms at the injection

times (respectively, $\{t_k, k = 1 \dots l\}$) and $\{t_j, j = 1 \dots m\}$). Besides, the drugs are progressively eliminated from the organism following an exponential clearance, having:

$$\begin{aligned} \frac{dc_4}{dt}(t) &= -\nu c_4(t), \quad \forall t \neq t_j, \\ \Delta c_4(t_j) &= i_{c_4}, \qquad \forall t = t_j, \end{aligned} \tag{3.16}$$

and:

$$\begin{aligned} \frac{dp_1}{dt}(t) &= -\mu p_1(t), \quad \forall t \neq t_k, \\ \Delta p_1(t_k) &= i_{p_1}, \qquad \forall t = t_k. \end{aligned} \tag{3.17}$$

Being ν (days^{-1}) and μ (days^{-1}) the clearance rates of αCTLA4 and αPD(L)1 drugs, and i_{c_4} and i_{p_1} the respective administered doses in arbitrary units.

The pharmacokinetic modeling of IT drugs is simplified. However, equation (3.16) seems a good approximation for the kinetics of αCTLA4, as Selby *et al.* [126] investigated the biokinetics of different αCTLA4 drugs finding that they follow linear forms. Nevertheless, Deng *et al.* [127] investigated the biokinetics of αPDL1 and found a more complex non-linear behavior.

Rather than considering a complex model to characterize the effect of αCTLA4 on the activation process of T-cells, a simple dependence on c_4 was introduced in the parameter b in equations (3.8), (3.9) and (3.11). Thus, following the work by Serre *et al.* [34], αCTLA4 counteracts T-cell blockade as:

$$b \to \frac{b}{1 + c_4(t)}. \tag{3.18}$$

On the other hand, the effect of αPD(L)1 on the interaction between tumor cells and T-cells is modeled by introducing a dependence on the parameter p in equation (3.15), having:

$$p \to p(1 + p_1(t)), \tag{3.19}$$

that results in enhanced immune-mediated death of tumor cells.

3.2.6 The complete model

Let $\{t_i, i = 1 \dots n\}$, $\{t_j, j = 1 \dots m\}$, and $\{t_k, k = 1 \dots l\}$ be the delivery times of RT, αCTLA4, and αPD(L)1, respectively; and $C_{\text{tot}}(t) = C(t) + C_{\text{d}}(t)$ with $C_{\text{d}}(t) = \sum_{i=1}^{n} C_{\text{d},i}$.

Assembling the equations presented in the above sections, the complete model of tumor response to RIT is for all $t \neq t_i$:

$$\begin{aligned}
\frac{dC}{dt}(t) &= \lambda_1 C(t)\left(1-\lambda_2 C_{\mathrm{tot}}(t)\right) - p(1+p_1(t))\frac{(T_{\mathrm{a}}(t)/C_{\mathrm{tot}}(t))^q}{s+(T_{\mathrm{a}}(t)/C_{\mathrm{tot}}(t))^q}C(t),\\
\frac{dC_{\mathrm{d},i}}{dt}(t) &= -\phi\omega(\overline{t_i})C_{\mathrm{d},i}(t) - p(1+p_1(t))\frac{(T_{\mathrm{a}}(t)/C_{\mathrm{tot}}(t))^q}{s+(T_{\mathrm{a}}(t)/C_{\mathrm{tot}}(t))^q}C_{\mathrm{d},i}(t),\\
\frac{dT_{\mathrm{a}}}{dt}(t) &= a\hat{A}(t-\tau_{\mathrm{T}})\hat{T}(t-\tau_{\mathrm{T}}) - \iota T_{\mathrm{a}}(t)C_{\mathrm{tot}}(t) - \eta T_{\mathrm{a}}(t),\\
\frac{d\hat{T}}{dt}(t) &= -a\hat{A}(t)\hat{T}(t) - \frac{b}{1+c_4(t)}\hat{A}(t)\hat{T}(t) + h,\\
\frac{d\hat{T}_{\mathrm{a}}}{dt}(t) &= a\hat{A}(t)\hat{T}(t),\\
\frac{d\hat{T}_{\mathrm{b}}}{dt}(t) &= \frac{b}{1+c_4(t)}\hat{A}(t)\hat{T}(t),\\
\frac{d\hat{A}}{dt}(t) &= \rho C_{\mathrm{tot}}(t-\tau_{\mathrm{A}}) + \psi\phi\sum_{i=1}^{n}\omega(\overline{t_i-\tau_{\mathrm{A}}})C_{\mathrm{d},i}(t-\tau_{\mathrm{A}}) - \sigma\hat{A}(t)\\
&\qquad - a\hat{A}(t)\hat{T}(t) - \frac{b}{1+c_4(t)}\hat{A}(t)\hat{T}(t),
\end{aligned}$$

where the function ω is given by equation (3.5), and the biokinetics of αPD(L)1 and αCTLA4 drugs are described by:

$$\begin{aligned}
\frac{dc_4}{dt}(t) &= -\nu c_4(t), \quad \forall t \neq t_j,\\
\frac{dp_1}{dt}(t) &= -\mu p_1(t), \quad \forall t \neq t_k.
\end{aligned}$$

Moreover, the following impulses are introduced at treatment delivery times:

$$\begin{aligned}
\Delta C(t_i) &= (SF_{\mathrm{C}}(d_i)-1)C(t_i), && \forall t = t_i,\\
\Delta C_{\mathrm{d},i}(t_i) &= (1-SF_{\mathrm{C}}(d_i))C(t_i), && \forall t = t_i,\\
\Delta T_{\mathrm{a}}(t_i) &= (SF_{\mathrm{T}}(d_i)-1)T_{\mathrm{a}}(t_i), && \forall t = t_i,\\
\Delta c_4(t_j) &= i_{c_4}, && \forall t = t_j,\\
\Delta p_1(t_k) &= i_{p_1}, && \forall t = t_k,
\end{aligned}$$

where $SF_{\mathrm{C}}(d)$ is given by the LQ model (1.1), the LQL model (1.7) or the $\mathrm{LQ}_{\mathrm{mod}}$ model (3.2); and $SF_{\mathrm{T}}(d)$ is obtained from the LQ model. Besides, the initial conditions for $t \in [-\max\{\tau_{\mathrm{A}},\tau_{\mathrm{T}}\},0]$ are $C(t) = C_0 > 0$, $\hat{T}(t) = T_0 > 0$, and the remaining initial values are set to 0.

Some notes on the formal analysis of the proposed model are presented in Appendix B.

3.3 Specific methods and materials in RIT

In addition to the general methods described in Chapter 2, this section presents specific methods used in the RIT study.

3.3.1 Numerical solution

The model presented in Section 3.2.6 was numerically solved by employing the forward Euler method, described in Section 2.1.3. To obtain the numerical solution, different user-defined functions were coded in MATLAB, which are available on the Dataverse repository [128]. Details about a convergence study can be found in Appendix C.

3.3.2 Experimental data

To validate and test the model, experimental data were collected from published preclinical studies available in the literature.

On the one hand, Dewan *et al.* [59] studied the response of preclinical tumors in mice populations to RT (different fractionations) and αCTLA4, either as monotherapies or combined. Tumor cells (TSA breast carcinoma cells) were implanted and let grow for 12 days, until reaching a volume of ~ 32 mm^3. Treatments started at that time, and the evolution of tumor volumes was monitored every 5 days until day 35 after tumor injection. The study also reported the fraction of animals where tumor control was achieved (no evidence of tumor at the time of euthanasia). Establishing the first day of the treatment as day 0, the authors investigated tumor response to the following RIT schedules (see Figure 3.2):

i) control,

ii) RT alone, 20 Gy single-fraction,

iii) RT alone, 8 Gy×3 (days 0, 1, 2),

iv) RT alone, 6 Gy×5 (days 0, 1, 2, 3, 4),

v) IT alone, delivered in 3 fractions (days 2, 5, 8),

vi) RIT, 20 Gy×1 RT and 3 fractions IT (days 2, 5, 8),

vii) RIT, 8 Gy×3 RT and 3 fractions IT (days 2, 5, 8),

viii) RIT, 6 Gy×5 RT and 3 fractions IT (days 2, 5, 8),

ix) RIT, 8 Gy×3 RT and 3 fractions IT (days 0, 3, 6),

x) RIT, 8 Gy×3 RT and 3 fractions IT (days 4, 6, 8).

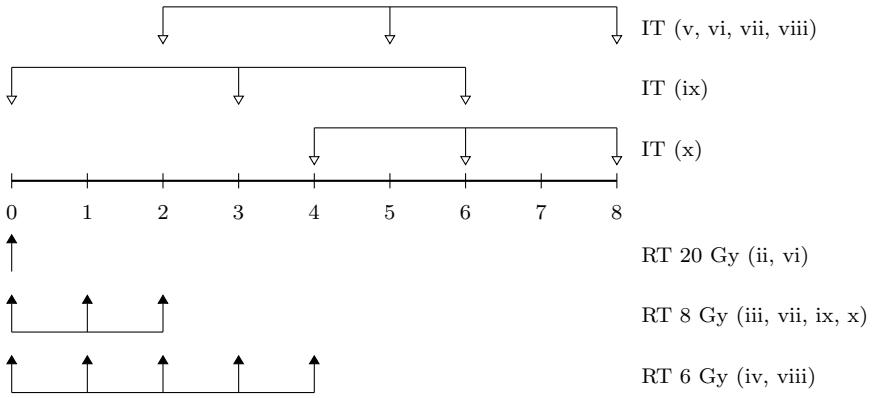

Figure 3.2: Administration schedule of treatments combining different RadioTherapy (RT) fractionations and ImmunoTherapy (IT) delivery times with αCTLA4, experimentally studied by Dewan *et al.* [59].

On the other hand, Deng *et al.* [18] presented data of tumor response to RT and αPDL1, either as monotherapies or combined. Cancer cells (TUBO breast carcinoma cells) were implanted in mice, and tumors were allowed to grow for 14 days until they had volumes of $\sim$ 120 mm^3. At that time, treatments started and tumor volumes were monitored every 3 days up to day 35 after tumor injection. Establishing the first day of treatment as day 0, the investigated schedules were:

i) control,

ii) RT alone, 12 Gy single-fraction,

iii) IT alone, delivered in 4 fractions (days 0, 3, 6, 9),

iv) RIT, 12 Gy×1 RT and 4 fractions of IT (days 0, 3, 6, 9).

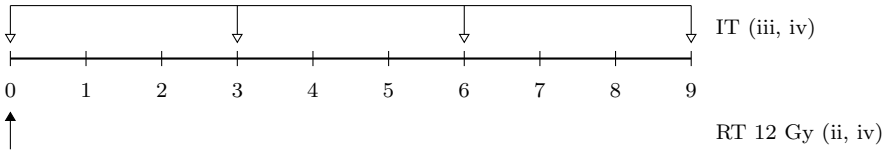

Figure 3.3: Administration schedule of treatments combining different RadioTherapy (RT) fractionations and ImmunoTherapy (IT) delivery times with αPDL1, experimentally studied by Deng *et al.* [18].

The response model was fitted to the reported data of (population-averaged) tumor volume evolution. Firstly, the simulated tumors freely grew until reaching the pre-treatment reported volumes. That time was considered as reference (day 0), and treatment times were defined relative to it onwards. Notice that the time to reach the initial volumes differs from the experimental results, as the performed simulations start from different numbers of cells than those experimentally injected (100 against $10^5 - 10^6$ tumor cells). Besides, the model does not aim to describe free tumor growth, which may be dominated by different mechanisms than tumor response.

3.3.3 Model fitting

To obtain tumor volumes from the model, both tumor cells (viable and doomed) and T-cells within the tumor were accounted for, having:

$$V(t) = C_{\text{tot}}(t)V_{\text{C}} + T_{\text{a}}(t)V_{\text{T}}, \tag{3.20}$$

where V_{C} (mm^3) and V_{T} (mm^3) are the volumes of individual tumor cells and T-cells, respectively.

The SA algorithm described in Section 2.3.3 was used to find best-fitting parameters, with a fitting function given by the WSSD between modeled and experimental values (see Section 2.3.1). The optimization method was applied to all response curves of each study at once (i.e. the sum of squared differences runs over different time points and combinations of RT and IT), to avoid different best-fitting parameters for each curve.

3.3.4 Parameter values

Some of the model parameters were not fitted, but set to values obtained from the literature. Cell volumes in equation (3.20) were set to $V_{\text{C}} = 10^{-6}$ mm^3 and $V_{\text{T}} = 2 \times 10^{-7}$ mm^3 [129]. For T-cells, the LQ parameters were set to $\alpha_{\text{T}} = 0.1$ Gy^{-1} and $\alpha_{\text{T}}/\beta_{\text{T}} = 10$ Gy (assuming radiosentitive T-cells). The biokinetic elimination rates of αPDL1 and αCTLA4 were set to $\mu = 0.5$ days^{-1} and $\nu = 0.1$ days^{-1} respectively, from fits to data reported in the literature [126, 127]. The parameters characterizing the mitotic delay of radiation-damaged cells were set to $\tau_{\text{d}1} = 1$ days, $\tau_{\text{d}2} = 1.5$ days, which values are in the range of reported mitotic delays [130]. Although a and b were considered free parameters to be fitted, the activation/inactivation rate of T-cells was fixed to $r = 1 + b/a = 5$ [34].

On the other hand, values of best-fitting parameters were constrained to qualitative reasonable bounding intervals when deemed necessary, to avoid unphysical/unreasonable values (for example, $\alpha_{\text{T}} > 0$ and $\beta_{\text{T}} > 0$ in the LQ model, or $\lambda_1 > 0$ for tumor proliferation). The bounding intervals are shown in Table D.1.

3.3.5 Sensitivity analysis

A local sensitivity analysis was performed to study the influence of parameter values on the model fit to experimental data. The sensitivity of the cost function to parameter perturbations was evaluated following a one-at-a-time approach around best-fitting values as:

$$S_i = |F(\boldsymbol{x} + \Delta\boldsymbol{x}_i) - F(\boldsymbol{x})|\,, \tag{3.21}$$

where F is the cost function given by the WSSD (equation (2.11)), $\boldsymbol{x}$ the set of best-fitting parameters and $\Delta\boldsymbol{x}_i = (0, ..., 0, 0.1x_i, 0, ..., 0)$ (setting a 10% perturbation with respect to the best-fitting value x_i).

It has to be noticed that the local sensitivity analysis has limited application to nonlinear models, like the case of this study. The followed approach only partially explores the parametric space and underestimates the interplay between the model factors, which may lead to biased results. However, this procedure was used as a low computational cost method to explore which mechanisms might be more relevant in the response to RIT. In order to perform a more exhaustive study, it should be complemented with a global sensitivity analysis, that requires higher computational demands [131].

3.3.6 Modeling TCP: Markov model

Based on the clonogenic cell hypothesis, all cells with proliferating capacity, corresponding to the compartment C in the model, must be eliminated to control the tumor. Subsequently, control is achieved when C reaches 0.

The continuous and deterministic model presented before was transformed into a discrete and stochastic model by including a Markov birth-death stochastic process [132]. For each viable tumor cell, a probabilistic experiment is performed to decide whether the cell multiplies, dies, or none, resulting in two, zero, or one cells, as depicted in Figure 3.4. The terms in the differential equations are interpreted as birth or death probabilities, respectively P_p and P_d, having:

$$\begin{aligned} P_\mathrm{p} &= \lambda_1 \left(1 - \lambda_2 C_\mathrm{tot}(t)\right) \Delta t, \\ P_\mathrm{d} &= p(1 + p_1(t)) \frac{(T_\mathrm{a}(t)/C_\mathrm{tot}(t))^q}{s + (T_\mathrm{a}(t)/C_\mathrm{tot}(t))^q} \Delta t, \end{aligned}$$

where Δt is the discretization time step used to numerically solve the model.

To limit the computation times, the stochastic Markov modification only applies when the number of viable tumor cells falls below a certain threshold, set to 1000 cells.

The stochasticity of the Markov model introduces variability in the solutions for identical sets of parameter values. Moreover, to simulate heterogeneous populations, random perturbations were introduced in the parameter values. 200 simulations were performed introducing random normal perturbations with a 5% standard deviation

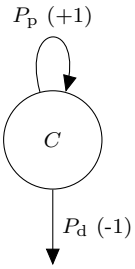

Figure 3.4: Sketch of the process described by the Markov birth-death model. C is the number of clonogenic tumor cells, P_p is the proliferation probability and P_d is the death probability.

around best-fitting parameter values. For the resulting population, the TCP was computed as the ratio of controlled tumors out of the total number of simulations.

3.4 Results

This section summarizes the results on RIT regarding the fit of the presented model to preclinical volumes, the simulation of experimental TCP, and the optimization of RIT delivery schedules.

3.4.1 Model fitting to preclinical data of tumor response to RIT with αPDL1 and αCTLA4

The response model was fitted to the volume dynamics data presented by Dewan *et al.* [59], corresponding to different combinations of RIT with αCTLA4, as described in Section 3.3.2. The LQ model (1.1) fails at simultaneously fitting the volume response curves from experiments with high and low doses per fraction. Thus, the LQ_{mod} model (3.2) was employed to account for the radiation damage on tumor cells, as presented in Section 3.2.2. Figure 3.5 shows the best fits, while the corresponding best-fitting parameters are presented in Table D.2. This dataset shows exponential tumor growth in the control group and non-significant effect of αCTLA4 monotherapy on tumor response. RT alone causes a moderate tumor response, and combinations of RT and αCTLA4 lead to an important decrease on tumor growth.

Some relevant parameter values are the proliferation rate ($\lambda_1 = 0.1367$ days^{-1}), the radiation damage parameters ($\alpha_C = 0.0200$ Gy^{-1}, $\beta_C = 0.0068$ Gy^{-2}, and $c = -0.2001$ Gy$^{-1/2}$), and the immune-mediated death rate on tumor cells ($p = 24.4339$ days^{-1}) and T-cells ($\iota = 1.9847 \times 10^{-8}$ days^{-1}). For reference, the best-fitting value of the cost function was $F = 29.5606$.

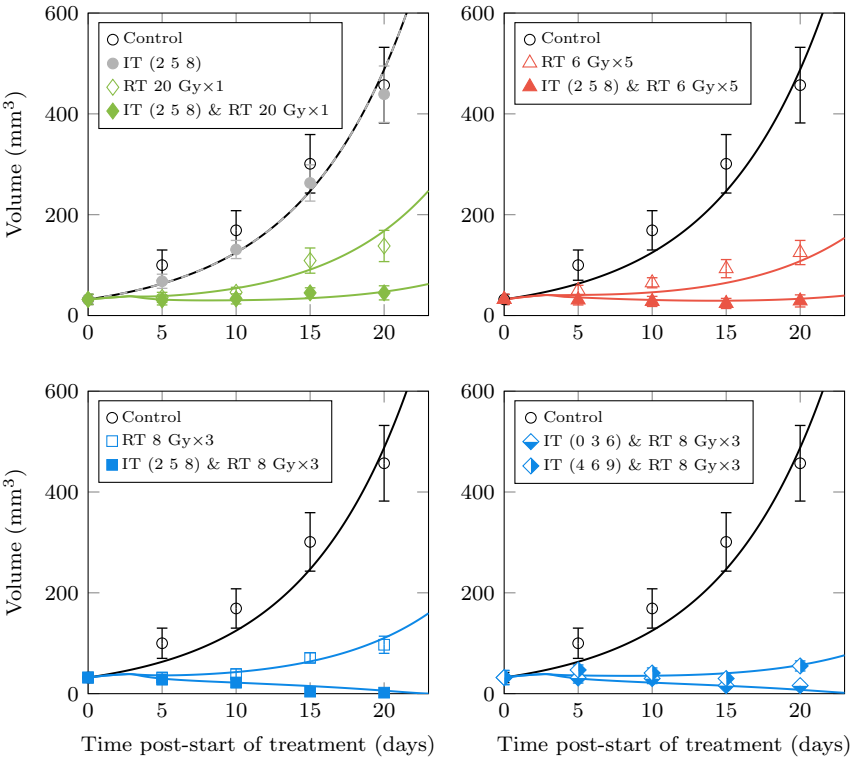

Figure 3.5: Model fitting to experimental data reported by Dewan *et al.* [59] of tumor response to RadioTherapy (RT), ImmunoTherapy (IT) with αCTLA4, and combined treatments. The $\mathrm{LQ}_{\mathrm{mod}}$ model (3.2) accounts for the radiosensitivity of tumor cells. Radiation doses were delivered on consecutive days starting from day 0. Notice that differences between control and IT curves are small and both of them overlap in the figure. All the fits were obtained with a single set of parameters, although they are plotted separately to facilitate the visualization. The control curve is included in all the panels as a common reference.

Negative values for parameter c in equation (3.2) point to a decrease in relative radiosensitivity with increasing dose. Such behavior can be also described by using the LQL model (1.7). Therefore, the same fit was performed with the LQL model instead, obtaining similar results, as shown in Figure 3.6. Best-fitting parameters are reported in Table D.3, including relevant parameters associated with proliferation ($\lambda_1 = 0.1356$ days^{-1}), radiation damage ($\alpha_{\mathrm{C}} = 0.0442$ Gy^{-1}, $\beta_{\mathrm{C}} = 0.0167$ Gy^{-2}, and $\gamma = 8.4298$ Gy^{-1}) and the immune effect on tumor cells ($p = 23.3045$ days^{-1}) and T-cells ($\iota = 2.2922 \times 10^{-8}$ days^{-1}). For reference, the best-fitting value of the cost function was $F = 42.1755$.

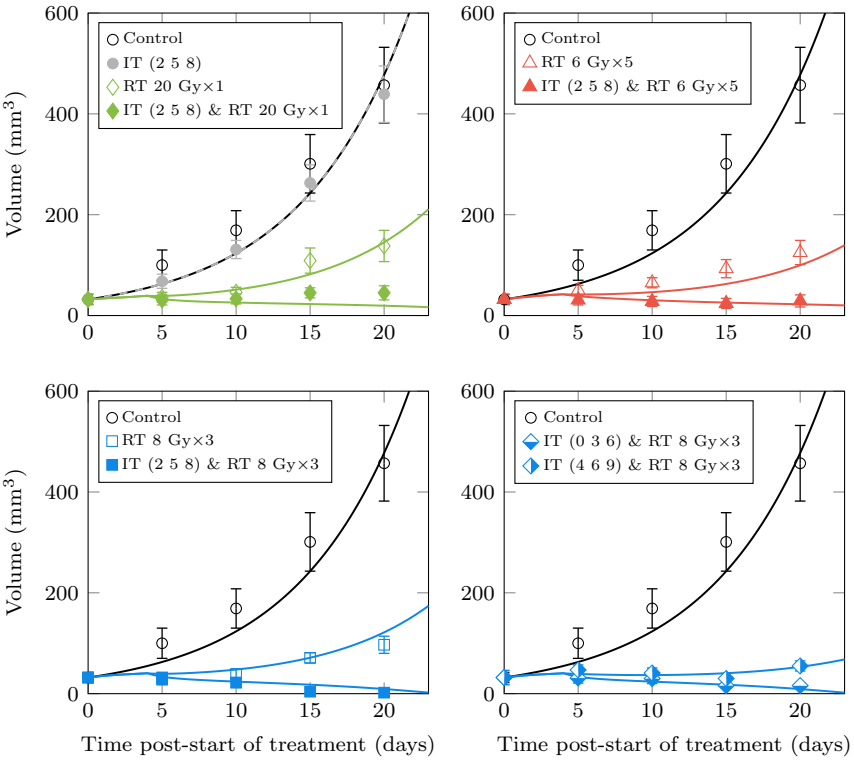

Figure 3.6: Model fitting to experimental data reported by Dewan *et al.* [59] of tumor response to RadioTherapy (RT), ImmunoTherapy (IT) with αCTLA4, and combined treatments. The LQL model (1.7) accounts for the radiosensitivity of tumor cells. Radiation doses were delivered on consecutive days starting from day 0. Notice that differences between control and IT curves are small and both of them overlap in the figure. All the fits were obtained with a single set of parameters, although they are plotted separately to facilitate the visualization. The control curve is included in all the panels as a common reference.

The model was also fitted to data presented by Deng *et al.* [18], which shows tumor responses to RT and αPDL1, as mentioned in Section 3.3.2. Figure 3.7 shows the best fits, while the associated best-fitting parameters are reported in Table D.2. This dataset presents similar patterns of tumor response to the previous one: αPDL1 alone has a non-significant effect on tumor response, RT alone causes a moderate tumor response, and the combination of RT with αPDL1 leads to tumor growth decrease.

To fit the data of Figure 3.7, most of the best-fitting parameters obtained for the study in Figure 3.5 were kept fixed: only parameters related to the administration of αPDL1, tumor cell proliferation ($\lambda_1 = 0.1217$ days^{-1}) and tumor cell radiosensitivity

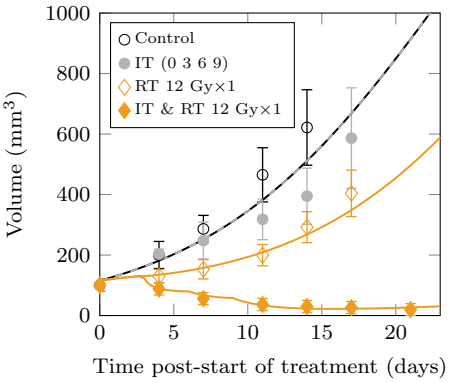

Figure 3.7: Model fitting to experimental data reported by Deng *et al.* [18] of tumor response to RadioTherapy (RT) (12 Gy single fraction on day 0), ImmunoTherapy (IT) with αPDL1, and combined treatments. The LQ model (1.1) accounts for the radiosensitivity of tumor cells. Notice that differences between control and IT curves are small and both of them overlap in the figure.

($\alpha_C = 0.0299$ Gy^{-1}) were allowed to vary. Because this dataset only includes one dose per fraction, the LQ model (1.1) was employed to describe radiation damage on tumor cells, imposing $\alpha_C/\beta_C = 10$ Gy and considering only α_C as a free parameter. While there are differences in the clones and tumors that could justify using different host-related and tumor-related parameters, imposing such constraints on the optimization limits reaching good fits by over-fitting.

3.4.2 Study of vascular damage on RIT effectiveness

Large radiation doses can seriously damage tumor vasculature, which might limit the infiltration of active T-cells in the tumor. This might explain the poorer results obtained with the 20 Gy single-fraction irradiation by Dewan *et al.* [59]. To test the hypothesis that vascular damage may affect the effectiveness of RIT, a dose and time-dependent T-cell infiltrating parameter was introduced in the model through equation (3.13), to account for vascular damage and recovery. This term represents the fraction of active T-cells reaching the tumor. Inspired by previous works [11, 95], critical vascular damage was considered for radiation doses above 15 Gy, followed by a progressive recovery of the vascular function.

Figure 3.8 shows the best fits of the model to data presented by Dewan *et al.* [59], considering vascular damage and the LQ model (1.1) to account for the radiation-mediated damage on tumor cells. Best-fitting parameter values are reported in Table D.4, including relevant parameters related to proliferation ($\lambda_1 = 0.1357$ days^{-1}), radiation damage ($\alpha_C = 0.0200$ Gy^{-1}, $\beta_C = 0.0022$ Gy^{-2}) and the immune effect

on tumor cells ($p = 24.9382$ days^{-1}) and T-cells ($\iota = 6.2472 \times 10^{-9}$ days^{-1}). For reference, the best-fitting value of the cost function was $F = 25.3345$.

The AIC was used to compare the goodness-of-fit between the three versions of the response model used to fit the data reported by Dewan *et al.* [59]. The likelihood of the fit, L, in equation (2.13) was computed as the product of the individual probabilities of having the modeled volumes assuming a Gaussian distribution. For $n = 50$ datapoints, the LQ model with vascular damage ($AIC = 436.24$, $k = 19$) was preferred to the LQ_{mod} model ($AIC = 446.02$, $k = 20$) and the LQL model ($AIC = 458.75$, $k = 20$) according to their AIC.

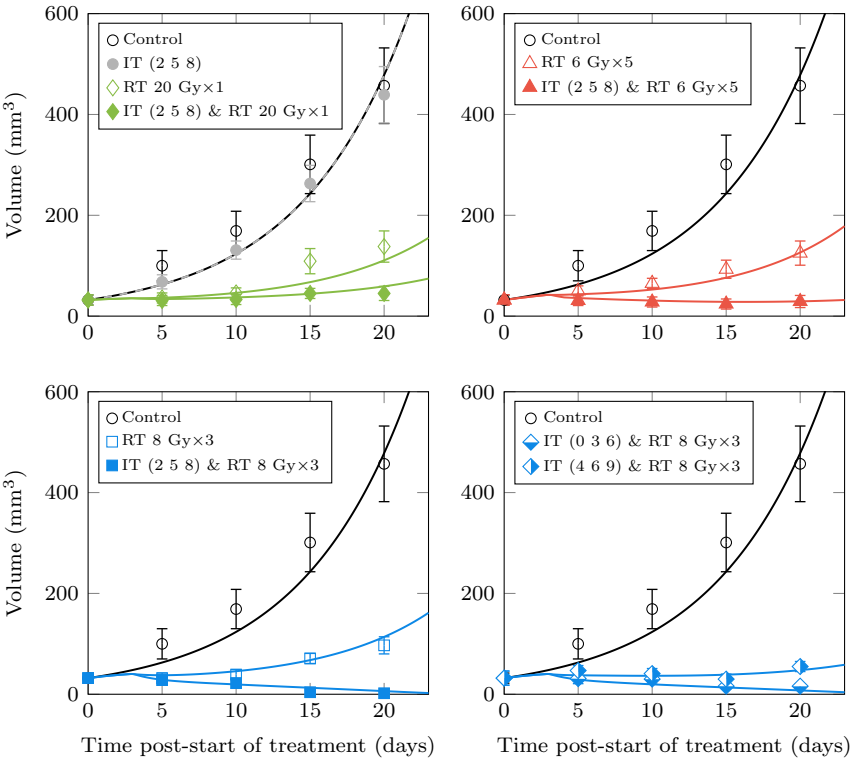

Figure 3.8: Model fitting to experimental data reported by Dewan *et al.* [59] of tumor response to RadioTherapy (RT), ImmunoTherapy (IT) with αCTLA4, and combined treatments. The LQ model characterizes tumor cell response to radiation, and vascular damage at 20 Gy per fraction was included to limit T-cell infiltration in the tumor. Radiation doses were delivered on consecutive days starting from day 0. Notice that differences between control and IT curves are small and both of them overlap in the figure. All the fits were obtained with a single set of parameters, although they are plotted separately to facilitate the visualization. The control curve is included in all the panels as a common reference.

Although the volumes presented in the previous figures include tumor cells and T-cells, the model should not reproduce tumor volumes by including low fractions of tumor cells and large fractions of T-cells, which would eventually lead to tumor control contradicting experimental evidence. Figures D.1 and D.2 present the contribution of tumor cells and T-cells to tumor volumes, showing that modeled tumor volumes are dominated by tumor cells.

3.4.3 Local sensitivity analysis

A local sensitivity analysis was performed, as described in Section 3.3.5. Table 3.1 ranks the sensitivity of the cost function to model parameters. The model is most sensitive to parameters describing tumor cell proliferation, radiosensitivity, and immune-mediated tumor cell death.

Parameter	Description	Sensitivity index
q	Immune-mediated tumor cell death parameter	309.4673
λ_1	Proliferation rate of tumor cells (days^{-1})	71.6561
s	Slope of the immune-mediated tumor death curve	20.7941
p	Immune-mediated tumor cell death rate (days^{-1})	12.8123
T_0	Initial pool of *blank* T-cells in activation site	7.3442
η	Rate of natural elimination of T-cells (days^{-1})	4.2115
h	Rate of production of *blank* T-cells (days^{-1})	3.5890
α_C	Linear parameter of LQ model for tumor cells (Gy^{-1})	2.1120
β_C	Quadratic parameter of LQ model for tumor cells (Gy^{-2})	1.8827
τ_A	Delay between antigen liberation and T-cell activation (days)	0.6541

Table 3.1: Analysis of the most critical model parameters. The sensitivity index given by equation (3.21) for each parameter is calculated as the difference between the cost function of fits to experimental data presented by Dewan *et al.* [59] (best-fitting parameters reported in Table D.4) and the cost function obtained when a 10% perturbation is applied to that particular parameter. Only the ten most critical parameters are shown. For reference, the best cost value was $F = 25.3345$.

3.4.4 Optimization of IT administration on RIT treatments

Finding the optimal sequence of administration of RIT can improve effectiveness, as experimentally shown in results presented by Dewan *et al.* [59]. In that study, the authors found that the combination of 8 Gy×3 RT fractions and 3 fractions of αCTLA4 lead to different tumor responses depending on the days of administration of the IT (RT was always delivered on the same days). In particular, different IT schedules lead to different tumor volumes and control rates. This may be caused by the interplay between biological mechanisms with different kinetics, such as the biological delays between the release of antigens and the activation of T-cells, as well as the migration of such T-cells to the tumor, tumor proliferation, and the progressive death of doomed cells.

The presented model along with the best-fitting parameters reported in Table D.4 were used to investigate optimal research strategies by simulating TCP, following the procedure described in Section 3.3.6. The administration of the three 8 Gy RT fractions was fixed on days 0, 1, and 2, while the delivery schedule of the three IT doses was varied, starting from day 0 to day 7, and ending from day 2 to day 9. The evolution of tumor volumes and the TCP were evaluated from 200 simulations on each combination.

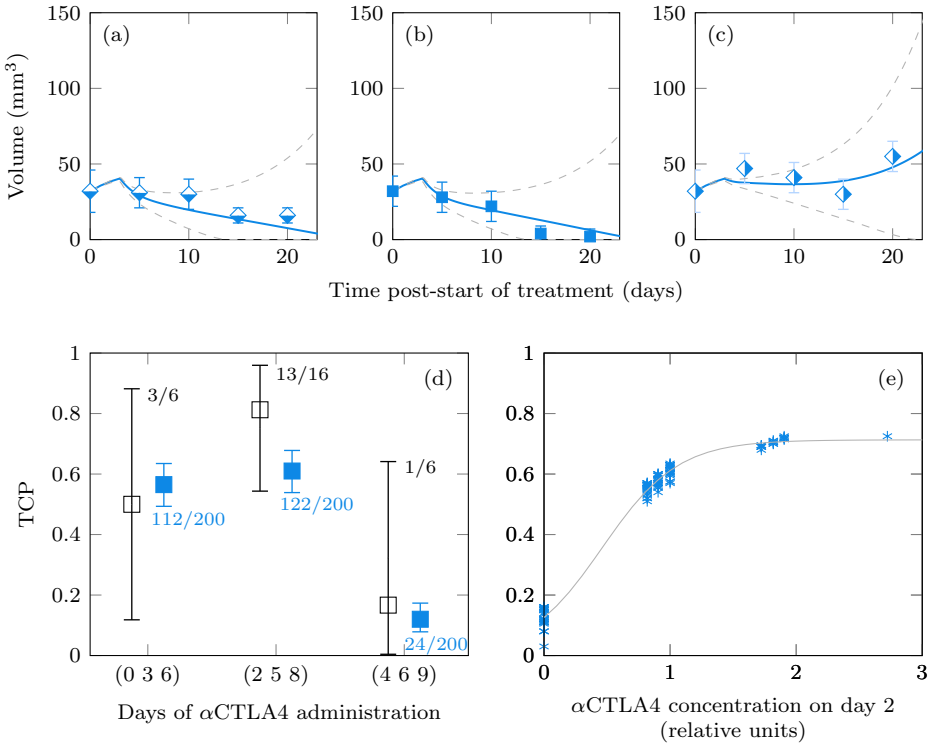

Figure 3.9: Study of optimal schedules of RT (8 Gy×3 fractions) and IT (3 fractions of αCTLA4) obtained from the presented model and best-fitting parameters reported in Table D.4. RT fractions are delivered at days (0, 1, 2), and IT is delivered with different schedules starting from day 0 to day 7. Panels (a), (b), and (c) report the dynamics of tumor volumes and the 95% confidence intervals for the combinations investigated by Dewan *et al.* [59], delivering IT at days (0, 3, 6), (2, 5, 8), and (4, 6, 9) respectively. Panel (d) shows the comparative between 95% confidence intervals for Tumor Control Probability (TCP) values obtained with the model (200 simulations) and experimental controls (6 to 16 animals), for the same treatment combinations. Panel (e) presents TCP (asterisks) versus the concentration of αCTLA4 on day 2 after starting treatment, showing a positive correlation between those two variables. The solid line corresponds to the fit of a logistic function.

Results are reported in Figure 3.9. Panels (a)–(c) report the evolution of tumor volumes with best-fitting parameters and 95% confidence intervals (obtained from the 200 different simulations) for the combinations investigated by Dewan *et al.* [59]. Panel (d) shows the comparative of 95% confidence intervals for TCP values obtained from the model (200 simulations) and experimental controls (6 to 16 animals), for the same previous combinations. The combination leading to the best tumor response is that delivering IT at days 2, 5 and 8. Moreover, the relation between modeled TCP and different metrics related to the administration of IT was studied. As shown in panel (e), the concentration of αCTLA4 on day 2 is associated with TCP.

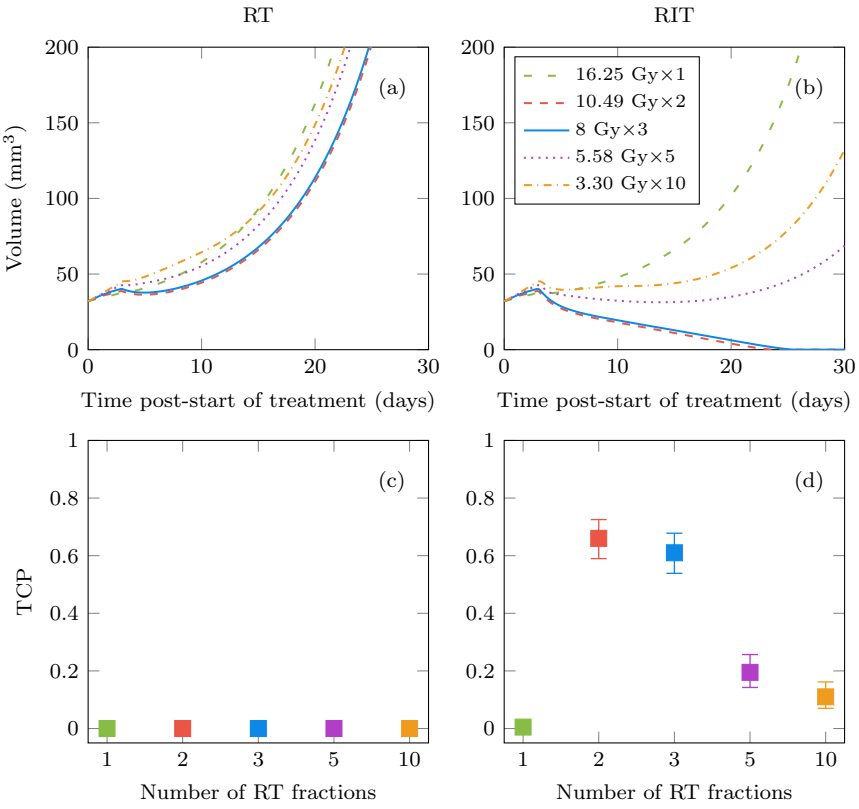

Figure 3.10: Modeled responses to different RadioTherapy (RT) schedules with αCTLA4 (2, 5, 8). RT fractionations are equivalent from a classical radiobiological point of view (same BED). Tumor volume evolution is shown for RT alone (a), and RadioImmunoTherapy (RIT) with αCTLA4 (b). Tumor Control Probability (TCP) (95% confidence intervals) were obtained from the model (200 simulations) for RT alone (c), and RIT (d). The model parameters used for this study are presented in Table D.4, and include vascular damage effect at 16.25 Gy, governed by equation (3.13).

3.4.5 Optimization of dose fractionation on RIT treatments

The effect of different RT fractionations as monotherapy or in combination with αCTLA4 (fixed to days 2, 5, and 8) was studied. The treatment with 8 Gy×3 fractions was used as a reference, and different RT fractionations (1, 2, 3, 5, or 10 fractions, one fraction per day on consecutive days) were studied. The doses of each fractionation schedule were selected to have the same BED, given by equation (1.11), using $\alpha_C/\beta_C = 9.29$ Gy (corresponding to the value presented on Table D.4). For this α_C/β_C ratio, the resulting doses per fraction were: 16.25 (×1), 10.49 (×2), 8 (×3), 5.58 (×5), and 3.30 (×10) Gy.

Figure 3.10 reports the evolution of tumor volumes under different treatment regimens, as well as TCPs (replicating the experiment described in the previous section for 200 simulations and normally distributed perturbations on the reference values from Table D.4).

Conventional fractionation may be sub-standard, as daily fractions can deplete active T-cells from the tumor (it is widely assumed that T-cells are radiosensitive, even though this idea may be contradicted by recent evidence [133]). In this regard, hypofractionated schedules may prove more effective, as already seen in some experimental studies, but without reaching extreme hypofractionation. In the latter case, the strategy may result disadvantageous due to two factors: on the one hand, a single fraction may fail to keep therapeutic numbers of T-cells in the tumor for a long time; on the other hand, large doses may lose some effectiveness, and can seriously damage tumor vasculature, which might limit the infiltration of active T-cells in the tumor.

Figure 3.11 shows the evolution of the main populations for three different treatments. As can be seen in panels (a) and (b), in line with what was hypothesized above, the combined treatment with hypofractionated non-single-dose radiation is the most effective. Furthermore, in panels (c) and (d) it can be seen that while with single-dose treatment the number of T-cells reaching the tumor is limited, with a more fractionated treatment the radiation eliminates active T-cells in the tumor reducing its efficacy. Table 3.2 summarizes the findings and shows the strengths and weaknesses of each treatment.

	Activation	Infiltration	Death
Extreme-hypofractionated RT	✓	✘	✓
Moderate-hypofractionated RT	✓	✓	✓
Conventional RT	✓	✓	✘

Table 3.2: Comparative between different fractionated RadioTherapy (RT) schedules regarding T-cell's activation, infiltration, and radiation-mediated death. While extreme-hypofractionated regimens may compromise the therapeutic effect by reducing T-cell infiltration, conventional treatments might be also suboptimal by promoting the elimination of T-cells due to multiple irradiations.

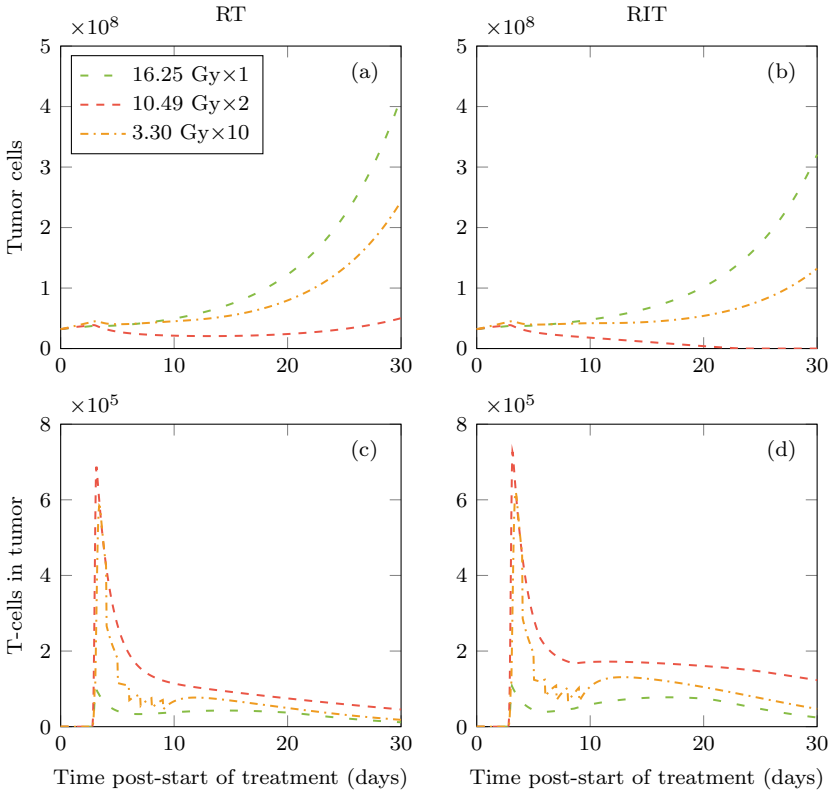

Figure 3.11: Evolution of tumor cells and active T-cells in the tumor zone for the different fractionations: single-dose, non-single-dose hypofractionation, and more fractionated treatment. The panels on the left correspond to RadioTherapy (RT) and those on the right to RadioImmunoTherapy (RIT) with αCTLA4 (2 5 8). Non-single-dose hypofractionated treatments appear to be more effective, as they allow T-cell infiltration into the tumor and reduce T-cell damage.

3.5 Discussion

The proposed model fits experimental volume curves of tumor response to different combinations of RIT with αPDL1 and αCTLA4, as shown in Sections 3.4.1 and 3.4.2. Furthermore, it reproduces experimental TCP values, as presented in Section 3.4.4, even though these fits are favored by large experimental uncertainties obtained from trials with small population sample sizes. However, a limitation of the presented model is the risk of overfitting due to the lack of validation data compared to the number of parameters involved. To mitigate this weakness, as many parameters as possible were set to fixed values according to the existing literature, as shown in Section 3.3.4,

and their range of variation in the optimization process was limited to consistent values, reported in Table D.1. Besides, most of the parameters (16/20) obtained from the fitting to data of RIT with αCTLA4 were kept fixed when simulating data of RIT with αPDL1, as mentioned in Section 3.4.1. These constraints strengthen the obtained results, although they should still be taken with care.

On the other hand, the model fails to reproduce the effect of αPDL1 and αCTLA4 as monotherapies on the progression of tumor volumes. While this effect is small in the collected experimental data, they show a consistent influence of IT on tumor volume. However, the model shows a non-noticeable effect of αCTLA4 and αPDL1 monotherapies for the considered experiments, as reported in Sections 3.4.1 and 3.4.2. Therefore, its application to the particular case of IT as monotherapy could be debatable. In any case, it might be that the low percentage of subjects responding to IT monotherapy treatments present a particular phenotype (model parameters) that makes them more sensitive to such therapies, an effect that cannot be reproduced when fitting population-averaged data.

The fits suggest very radioresistant tumors (low α values) but are in line with reported experimental values for tumors in mice [134]. Moreover, the best fits were obtained when the relative radiosensitivity of tumor cells decreases with increasing dose per fraction, as predicted by the LQL model. Such effect could also be explained by a limited infiltration of T-cells into the tumor due to vascular damage at large doses per fraction. It must be noticed that, for the sake of simplicity, only the effect of limited T-cell infiltration was included in the analysis, but vascular damage may cause other effects, such as proliferation arrest, starvation, and hypoxia, resulting in a complex interaction.

The obtained results led to the formulation of some hypotheses regarding the effectiveness of RIT and optimal treatment combinations. On the one hand, experimental results show that delivering IT at days (2, 5, 8) leads to a better response than deliveries at days (0, 3, 6) or (4, 6, 9). Given the slow clearance rate of αCTLA4, with mean lifetime $T_{1/2} \sim 7$ days, the elimination from day 0 to day 2, and from day 2 to day 4, is $\sim 20\%$ of the drug concentration. This seems to point out that biological delays may influence the activation and/or immune effect of T-cells. The modeling study of optimal combinations (see Section 3.4.4) suggests that a better synergy could be obtained by delivering IT soon after the first fraction of RT, and then continuing IT fractions longer into the treatment, to keep therapeutic numbers of T-cells in the tumor for a longer time (according to the different kinetics of the IT drug, tumor cell death, and antigen liberation). The combined treatment starts to lose effectiveness if the administration of IT is delayed beyond 2–3 days post-start of RT. On the other hand, both conventional fractionation and extreme hypofractionation may be suboptimal in RIT treatments, as reported in Section 3.4.5. High doses per fraction used in extreme hypofractionated schedules may lead to loss of effectiveness due to saturation damage (modeled by the LQL model), and cause critical vascular damage compromising T-cell infiltration. This might also explain the poorer results obtained

with the 20 Gy single-fraction irradiation. On the contrary, conventional fractionations cause multiple irradiations of circulating T-cells, reducing their immune activity. Thus, moderate hypofractionation of the radiation dose may offer the best results.

Direct extrapolation of the above hypotheses to clinical data must be considered with care, for they are based on the analysis of preclinical data. In human tumors, many biological processes are slower than in mice (such as cell proliferation, clearance and biokinetics of drugs, and migration) and will certainly affect the complex interplay that leads to optimal treatment combinations.

The combined study of indirect tumor cell death mechanisms (due to vascular damage and radiation-triggered immune response) and direct radiation damage on tumor cells may be paramount in RT and RIT, as both processes may interfere with each other. Biomathematical models linking these effects can provide insight into the problem and help to interpret experimental results, as well as to interpret conflicting reports on the effect of indirect cell death on tumor response [11, 21].

Compared to other models of IT and RIT response, this thesis presents a simpler modeling of the immune-mediated tumor cell death, including a single population of T-cells and ignoring other populations. Besides, the most relevant novelty is the introduction of biological delays (through DDEs). It is hypothesized that these biological delays play an important role in the response to RIT, and should be considered in the design of optimal combination strategies. This seems to be supported by experimental results, as argued above. Moreover, a stochastic approach was introduced to compute TCPs, and the effect of vascular damage in the response to RIT was investigated.

Chapter 4

Results on FLASH radiotherapy

"I'm a racecar, you're... a much older racecar,
but under the hood, you and I are the same."
"We are not the same! Understand?"
— Lightning McQueen & Doc Hudson, *Cars.*

This chapter summarizes the outcomes achieved during the thesis on developing mathematical models for FLASH radiotherapy. This novel radiation modality has preclinically proven to decrease toxicity in healthy tissue around tumors while maintaining the anti-tumor effect of conventional radiotherapy. Building on previous works, this chapter presents a mathematical approach to replicate tumor volume evolution curves in preclinical FLASH and conventional radiotherapy studies. This allows for the examination of the mechanisms behind the effect of FLASH radiotherapy and the analysis of its presumed iso-effectiveness compared to conventional modalities.
This chapter partially reproduces the content of the article: I. González-Crespo, F. Gómez, Ó. López Pouso, and J. Pardo-Montero, "An in-silico study of conventional and FLASH radiotherapy iso-effectiveness: potential impact of radiolytic oxygen depletion on tumor growth curves and tumor control probability," *Physics in Medicine & Biology*, vol. 69, p. 215016, 2024. DOI: 10.1088/1361-6560/ad8291. See the Copyright terms in Appendix F.

4.1 Overview of the problem

FLASH-RT is a modality that consists in delivering radiation doses at UHDRs exceeding 40 Gy s^{-1}, in contrast to the 0.05–0.40 Gy s^{-1} used in conv-RT [61, 62]. FLASH-RT has generated significant interest in recent years, as *in vivo* experiments have shown its potential to spare non-tumor tissue while maintaining the effectiveness of conv-RT on tumors, known as the FLASH effect [66–74]. Several preclinical studies reported fewer side effects when using FLASH-RT compared to conv-RT [66–68, 70–72, 74]. Some of these studies showed non-significant differences in tumor growth delay between the two techniques [66, 72]. Liljedahl *et al.* [73] reported long-term anti-tumor iso-effectiveness in conv-RT and FLASH-RT when re-challenging cured animals. Furthermore, Vozenin *et al.* [69] observed the protective effect of FLASH-RT in mini-pig and cat-cancer patients.

Many studies have suggested that the protective effect arises from the ROD process caused by irradiation at UHDRs, which results in increased cell radioresistance. Pratx and Kapp [75, 76] suggested that the sparing of hypoxic stem cell niches may motivate the protective effect of FLASH-RT. Cao *et al.* [78] reported that ROD may spare cells at very low oxygen levels (under 5 mmHg), while Petersson *et al.* [77] suggested that sparing may appear at intermediate oxygen levels (over 20 mmHg). However, other research works propose that oxygen depletion alone is insufficient to fully explain the protective effect [79–81, 100]. Instead, these studies suggest that additional physicochemical factors may contribute to the phenomenon, such as variations in reactive species production between tumor and non-tumor cells, the recombination of free radicals, or radiation-induced immune effects. In recent years, theoretical work has accompanied experimental studies in an attempt to elucidate the underlying mechanisms of the FLASH effect [81–84].

Understanding why the protective effect is not observed in tumors remains an ongoing area of research. As FLASH-RT moves closer to the clinical scenario [135–137], it is important to guarantee that clinical trials will not lead to decreased TCP, and if necessary to boost the radiation dose to compensate for such loss. In this regard, a recent theoretical study by Liew *et al.* [138] has argued that FLASH-RT might not preserve TCP. That research suggested that FLASH-RT might cause a substantial loss of TCP while showing that the sparing effect might be too small to be observed in the growth kinetics of preclinical tumors.

In this study, the possibility of TCP loss is theoretically analyzed considering the effect of ROD on the SF of cells. For that purpose, a systematic and progressive approach was followed by analyzing experimental data of ROD in solutions and *in vivo*, estimating SFs *in vitro*, and studying the growth curves of irradiated preclinical tumors. Finally, the results were extrapolated to TCP-dose curves in a clinical scenario, and the potential effect of ROD on the iso-effectiveness of FLASH-RT was studied according to the oxygenation status and radiosensitivity of irradiated tumors. Additionally, the modeling study considers the influence of heterogeneity in tumor

oxygen distributions, as Taylor *et al.* [84] have suggested that it may be paramount to characterize the impact of FLASH-RT.

4.2 Oxygenation model in FLASH-RT and conv-RT

The oxygenation problem was presented in Section 2.2. Different versions of equation (2.8) model oxygen partial pressure under particular conditions corresponding to the irradiation with conv-RT or FLASH-RT of various targets: water and other solutions mimicking cell compounds, cells *in vitro*, and tumors *in vivo*.

Variations of the oxygen partial pressure, p (mmHg), during FLASH-RT due to ROD in water and other solutions were modeled by the radiolytic consumption term presented in Section 2.2.6 (equation (2.10)) as follows:

$$\frac{dp(t)}{dt} = -\frac{D}{T}\frac{G_0\ p(t)}{k_{\mathrm{ROD}} + p(t)}. \tag{4.1}$$

Notice that D (Gy) is the radiation dose, T (s) is the total time of irradiation, G_0 (mmHg Gy^{-1}) is the radiolytic consumption rate, and k_{ROD} (mmHg) is the oxygen pressure for half-maximum oxygen depletion rate.

The same expression was employed to describe oxygen in the *in vitro* scenario. In that case, it is assumed a constant oxygenation level in the spatial coordinates. Moreover, the dynamics of any oxygen source are neglected for simplicity. This approach may overestimate oxygen depletion in the *in vitro* situation. However, this particular scenario is studied only to illustrate the potential differences in the SF of cells between FLASH-RT and conv-RT, not to analyze results from the experimental literature or debate the iso-effectiveness in terms of TCP, which are the main objectives of the presented work.

Following the work of Taylor *et al.* [84], the complete spatiotemporal reaction-diffusion equation (2.8) was employed to describe oxygen dynamics during FLASH-RT in simulated tumor tissue, including consumption terms due to the ROD effect, given by equation (2.10), and the metabolic activity of cells, described by equation (2.9). Thus, the following PDE modeled the oxygenation dynamics of *in vivo* experiments in FLASH-RT:

$$\frac{dp(t,\boldsymbol{x})}{dt} = D_{\mathrm{O}_2}\Delta p(t,\boldsymbol{x}) - g_{\max}\frac{p(t,\boldsymbol{x})}{k + p(t,\boldsymbol{x})} - \frac{D}{T}\frac{G_0\ p(t,\boldsymbol{x})}{k_{\mathrm{ROD}} + p(t,\boldsymbol{x})}. \tag{4.2}$$

Notice that D_{O_2} (μm^2 s^{-1}) is the diffusion coefficient of oxygen, $g_{\max}$ (mmHg s^{-1}) is the maximum depletion rate due to metabolic activity, and k (mmHg) is the oxygen pressure for half-maximum metabolic depletion rate.

As mentioned in Section 2.2.6, in conv-RT the amount of eliminated oxygen due to ROD is compensated by tumor blood vessels, in agreement with *in vivo* experiments.

Thus, the steady-state form of the above equation with no ROD was used to describe oxygen partial pressure in conv-RT as follows:

$$D_{O_2}\Delta p(\boldsymbol{x}) = g_{\max}\frac{p(\boldsymbol{x})}{k + p(\boldsymbol{x})}. \tag{4.3}$$

Equations (4.2) and (4.3) were defined over a two-dimensional domain (Ω) representing tumor tissue (see Section 2.2.2), and turned into IVPs, respectively Problem 2.3 and Problem 2.4, by imposing initial and boundary conditions.

4.3 SF in FLASH-RT and conv-RT

SFs were obtained from the LQ model with the OERs modification, given by equations (1.4)–(1.6). In order to introduce the dependence of oxygen partial pressure on the spatial coordinates, the SFs for conv-RT and FLASH-RT, respectively SF_{C} and SF_{F}, were calculated as follows [84] (note that here D refers to the radiation dose, d in equation (1.4)):

$$SF_{\mathrm{C}} = \int_{\Omega} SF(D, p(\boldsymbol{x}))d\Omega, \tag{4.4}$$

$$SF_{\mathrm{F}} = \frac{1}{T}\int_0^T \left(\int_{\Omega} SF(D, p(t, \boldsymbol{x}))d\Omega\right) dt, \tag{4.5}$$

where Ω is a two-dimensional domain (see Section 2.2.2), and $p(\boldsymbol{x})$ and $p(t, \boldsymbol{x})$ are the oxygen partial pressures, respectively obtained from equations (4.3) and (4.2).

4.4 Model of tumor volume evolution

A simple compartmental mathematical model was designed to describe the evolution of tumor volumes after FLASH-RT and conv-RT treatments. Two populations of tumor cells were considered, viable and radiation-doomed, that occupy volumes C, and C_{d}, respectively. Both types of cells undergo logistic proliferation [139] with growth rate λ (days^{-1}) and carrying capacity K (mm^3), as damaged cells are able to carry *abortive divisions* [125]. Moreover, doomed cells follow an exponential turnover [37] with a depletion rate γ (days^{-1}), which is constrained to be higher than λ, therefore resulting in a progressive elimination, having:

$$\frac{dC(t)}{dt} = \lambda\left(1 - \frac{C(t) + C_{\mathrm{d}}(t)}{K}\right)C(t), \tag{4.6}$$

$$\frac{dC_{\mathrm{d}}(t)}{dt} = \lambda\left(1 - \frac{C(t) + C_{\mathrm{d}}(t)}{K}\right)C_d(t) - \gamma C_{\mathrm{d}}(t). \tag{4.7}$$

Introducing a depletion rate $\phi = \gamma - \lambda$, thus $\phi > 0$, the model is rewritten as:

$$\frac{dC(t)}{dt} = \lambda \left(1 - \frac{C(t) + C_{\mathrm{d}}(t)}{K}\right) C(t), \tag{4.8}$$

$$\frac{dC_{\mathrm{d}}(t)}{dt} = -\lambda \frac{C(t) + C_{\mathrm{d}}(t)}{K} C_{\mathrm{d}}(t) - \phi C_{\mathrm{d}}(t). \tag{4.9}$$

Initial conditions were given as $C(0) = C_0$, where $C_0 > 0$, and $C_{\mathrm{d}}(0) = 0$. The total volume, V (mm^3), is defined as the sum of the two compartments, $V(t) = C(t) + C_{\mathrm{d}}(t)$.

The radiation effect is modeled as instantaneous by turning the above ODEs into IDEs (see Section 2.1.1). Let $\{t_i, i = 1 \dots n\}$ be the set of the n days in which a radiation treatment is delivered. Equations (4.8) and (4.9) are defined for $t \neq t_i$, while at the irradiation times, the following impulses are added to the model:

$$\Delta C(t_i) = (SF - 1) C(t_i), \tag{4.10}$$

$$\Delta C_{\mathrm{d}}(t_i) = (1 - SF) C(t_i), \tag{4.11}$$

being SF the corresponding SF for conv-RT or FLASH-RT, obtained through equations (4.4) and (4.5), respectively.

A theoretical study of some formal aspects of the presented model is shown in Appendix B.

4.5 Specific methods and materials in FLASH-RT

In addition to the general methods described in Chapter 2, this section presents specific methods used in the FLASH-RT study.

4.5.1 Numerical solution

The oxygenation model was solved in a two-dimensional squared domain, as detailed in Section 2.2.2, by using the FEM, described in Section 2.2.7. The theoretical framework for the use of the FEM is given in Section 2.2.4.

The model of tumor volume response was solved through the forward Euler method, described in Section 2.1.3. As this algorithm may present stability problems for particular cases, a convergence analysis for some of the performed simulations is included in Appendix C.

4.5.2 Experimental data

To validate and test the presented models, experimental data were collected from published preclinical studies available in the literature.

On the one hand, previous works [99–101] reported measurements of the amount of depleted oxygen by FLASH-RT in different solutions (water, Bovine Serum Albumin

(BSA), and CELL solution, respectively) for different dose rates and baseline oxygen levels. The characteristics of the collected data are summarized in Table 4.1.

Study	Irradiated medium	Radiation dose	Dose rate
Jansen *et al.* [100]	water	32.3 Gy	201.9 Gy s^{-1}
		31.9 Gy	319 Gy s^{-1}
		32.1 Gy	1.1×10^5 Gy s^{-1}
Van Slyke *et al.* [101]	CELL	30 Gy	100 Gy s^{-1}
El Khatib *et al.* [99]	BSA	30 Gy	100 Gy s^{-1}

Table 4.1: Characteristic of the collected experimental data of oxygen depletion. Notice that none of the experiments were performed on cellular compounds, but over different mediums that partially mimic the intracellular milieu. Van Slyke *et al.* used the CELL aqueous solution composed of glycerol, glucose, glutathione, and HEPES; while El Khatib *et al.* employed a 5% Bovine Serum Albumin (BSA) and phosphate solution.

Moreover, Van Slyke *et al.* [101] reported measurements of *in vivo* oxygen depletion in preclinical tumors with different mean oxygen partial pressure during FLASH-RT delivering 30 Gy with a dose rate of 100 Gy/s.

Study	Tumor line	Radiation dose	Dose rate	Sample size
Diffenderfer *et al.* [72]	MH641905	-	-	control (5)
		12 Gy	0.74 Gy s^{-1}	conv-RT (15)
		12 Gy	63 Gy s^{-1}	FLASH-RT (15)
		18 Gy	0.71 Gy s^{-1}	conv-RT (15)
		18 Gy	63 Gy s^{-1}	FLASH-RT (14)
Zhu *et al.* [140]	Py8119	-	-	control (8)
		9.5* Gy	0.20 Gy s^{-1}	conv-RT (8)
		9.5* Gy	125 Gy s^{-1}	FLASH-RT (8)
	Py230	-	-	control (8)
		9.5* Gy	0.20 Gy s^{-1}	conv-RT (8)
		9.5* Gy	125 Gy s^{-1}	FLASH-RT (8)

Table 4.2: Characteristic of the collected experimental data of tumor evolution in mice. *In the experiments by Zhu *et al.*, the absorbed dose was measured having, for a FLASH-RT planned dose of 10 Gy, received doses of 9.75 Gy, 9.50 Gy, 9.81 Gy and 9.36 Gy (following the table order), which were approximated by 9.5 Gy.

On the other hand, the study conducted by Diffenderfer *et al.* [72] reported the evolution of *in vivo* tumor volumes for a population of 64 mice separated in 5 groups: control (5 mice), 12 Gy conv-RT (15 mice), 12 Gy FLASH-RT (15 mice), 18 Gy conv-RT (15 mice) and 18 Gy FLASH-RT (14 mice). The dose rate used in those FLASH-RT experiments was 63 Gy s^{-1} and all of them involved single fraction schedules. Moreover, Zhu *et al.* [140] conducted two independent studies, each of them with a

different tumor line, involving 24 mice in each experiment separated into 3 groups: control (8 mice), 9.5 Gy conv-RT (8 mice) and 9.5 Gy FLASH-RT (8 mice). In this case, the dose rate was 125 Gy s^{-1}, and radiation was also delivered in a single fraction. The characteristics of the collected data are summarized in Table 4.2.

4.5.3 Model fitting

Equation (4.1) was fitted to the oxygen depletion experiments described in Table 4.1. Best-fitting parameters and the associated confidence intervals were obtained through the nonlinear optimization tools `nlinfit` and `nlparci` from the MATLAB Statistics and Machine Learning Toolbox.

The SA algorithm, described in Section 2.3.3, was employed to fit the volume model given by equations (4.8)–(4.11) to the datasets from the experiments summarized in Table 4.2. The fitting function was the WSSD between experimental data and the predicted values, given by equation (2.11).

4.5.4 Parameter values

Some model parameters were fixed to values obtained from the literature, reported in Table 4.3. On the contrary, other parameter values proceed from model fitting to the experimental datasets reported in Section 4.5.2, as detailed later in Section 4.6.1.

Parameter	Value	References
$g_{\max}$	15 mmHg s^{-1}	[94]
k	2.50 mmHg	[94]
D_{O_2}	$2{\times}10^3$ μm^2 s^{-1}	[94]
OER_α	2.50	[42]
OER_β	2.50	[42]
k_m	3.28 mmHg	[42]

Table 4.3: List of parameters in the oxygenation model fixed to values from the literature, and references to the corresponding studies.

4.5.5 Statistical analysis

Differences in the volume dynamics curves between the control, conv-RT and FLASH-RT groups were statistically analyzed by using ANalysis of COVAriance (ANCOVA) [141]. As ANCOVA uses linear models and tumor growth presents an exponential-like shape, tumor volumes were transformed into their logarithmic form, as was done in other works [66]. This study was performed using a separate lines model through the `aoctool` function from the MATLAB Statistics and Machine Learning Toolbox.

Moreover, the `multcompare` function was used to perform multiple comparison tests and obtain the associated p-values. Two curves were considered significantly different if p-value < 0.05.

4.5.6 Generation of simulated samples

Following the steps given in Section 2.2.2, 100 simulated tumor geometries were generated, using random VFs sampled from a normal distribution with mean μ=0.10, and standard deviation $\sigma = 0.04$, adding a 0.04 positive cutoff to avoid extremely poor vascularizations. The steady-state problem (Problem 2.4) was solved for each of the generated tumors to obtain oxygenation profiles, having baseline mean oxygen levels in the range $\sim$ 5–30 mmHg, similar to those reported in the literature [101]. Oxygen distributions, named as the H sample onwards, were limited to 100 simulations due to the computational cost of solving the oxygenation models. Figure E.1 illustrates the spatial oxygen distributions and the respective oxygenation histograms of two elements with different VFs, $f_v = 0.04$ and $f_v = 0.11$. Figure E.2 summarizes the oxygen distributions in the H sample as a heatmap.

When simulating oxygen evolution during FLASH-RT through Problem 2.3, different G_0 values were used for each distribution to introduce variability in oxygen depletion rates.

4.5.7 TCP estimation

The Poisson-LQ model (1.14), described in Section 1.3.4, was used to calculate TCP from the SFs obtained through equations (4.4) and (4.5), respectively in conv-RT and FLASH-RT.

To account for population heterogeneity on TCP calculations, a set of 1000 simulated tumors was obtained by randomly assigning different model parameters to each of them. In particular, each tumor was characterized by a radiosensitivity parameter, α_{ox} in equation (1.4), and a number of tumor cells, N_0 in equation (1.14), sampled from normal distributions with standard deviation equal to 20% of the mean values. Moreover, each one of the 1000 simulated tumors was associated with an oxygen distribution and radiolytic consumption rate from the H sample, introduced in the previous section.

TCP was calculated for several doses (assuming single fraction treatments) to obtain TCP-dose curves. Such curves were then characterized by calculating D_{50} (Gy) and D_{90} (Gy), the doses required to obtain $TCP = 0.5$ and 0.9, respectively, by interpolating the TCP-dose curve.

4.6 Results

This section summarizes the results on FLASH-RT regarding the use of the oxygenation model to reproduce oxygen depletion measurements from preclinical studies, the fit of the presented model of tumor evolution to preclinical volumes, and the simulation of TCP to study the assumed iso-effectiveness between conv-RT and FLASH-RT.

4.6.1 Simulation of oxygen depletion in FLASH-RT

Equation (4.1) was fitted to the measurements of depleted oxygen in water and other solutions reported in Table 4.1. Using the methodology described in Section 4.5.3, best-fitting values of G_0 and k_{ROD} were obtained. Figure 4.1 and Table 4.4 show the fitted curves and the best-fitting parameter values with 95% confidence intervals, respectively. From this study, the radiolytic depletion rate was set to $G_0 = 0.25$ mmHg Gy^{-1} as a reference value for the rest of the calculations, close to the mean value obtained from the fits presented in Table 4.4, and similar to values previously used by other authors [84]. The parameter k_{ROD} was set to 1 mmHg, which was also employed in previous modeling studies [84], and near to the best-fitting values reported in Table 4.4.

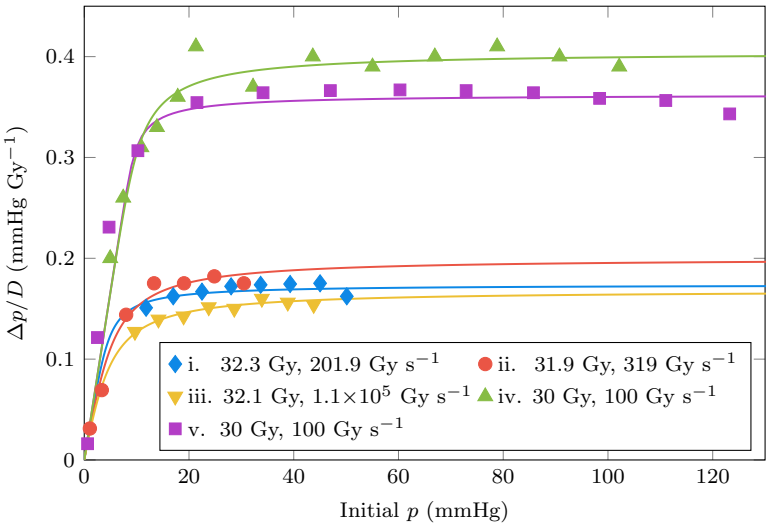

Figure 4.1: Oxygen depletion curves obtained by fitting equation (4.1) to the measurements reported by Jansen *et al.* [100] (i, ii and iii) in water, Van Slyke *et al.* [101] (iv) in CELL solution, and El Khatib *et al.* [99] (v) in BSA solution. The total amount of depleted oxygen during FLASH-RT, Δp, divided by the delivered radiation dose is presented against the initial oxygen partial pressure.

	G_0 (mmHg Gy^{-1})	k_{ROD} (mmHg)
i	0.179 ± 0.009	1.509 ± 1.112
ii	0.202 ± 0.022	2.418 ± 1.547
iii	0.166 ± 0.006	2.282 ± 0.732
iv	0.407 ± 0.019	1.303 ± 0.837
v	0.365 ± 0.021	0.650 ± 1.120

Table 4.4: Best-fitting values of G_0 and k_{ROD}, and 95% confidence intervals obtained by fitting (4.1) to the oxygen depletion curves reported by El Khatib *et al.* [99], Jansen *et al.* [100], and Van Slyke *et al.* [101]. The fits are shown in Figure 4.1.

Subsequently, the *in vivo* scenario was investigated. Using the simulated tumors from the H sample described in Section 4.5.6, oxygen depletion was calculated after a FLASH-RT delivery of 30 Gy with a dose rate of 100 Gy s^{-1}, and the results were compared with those reported by Van Slyke *et al.* [101]. A different radiolytic consumption rate was assigned to each simulated tumor following a normal distribution with mean $\mu = 0.25$ mmHg Gy^{-1} and 20% deviation from the mean value. Figure 4.2 presents the simulated and experimental data, which show a good agreement on the slope of the linear fits.

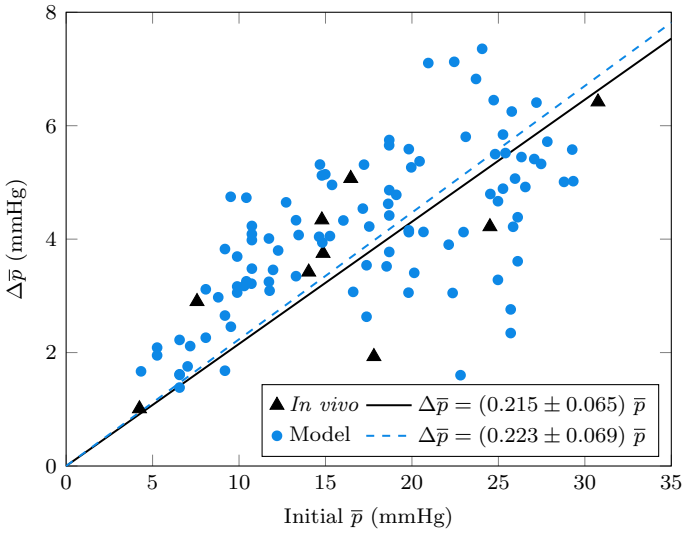

Figure 4.2: Amount of depleted oxygen during FLASH-RT (30 Gy, 100 Gy s^{-1}) versus the initial mean oxygen partial pressure, $\bar{p}$, in preclinical tumors. The triangles represent *in vivo* data reported by Van Slyke *et al.* [101], and the circles represent the simulated data for 100 tumors, obtained by solving Problem 2.3. Linear fits of each dataset are presented as solid and dashed lines, respectively.

4.6.2 Comparison of SF in conv-RT and FLASH-RT *in vitro*

As mentioned in Section 4.2, the effect of ROD on the SF of irradiated cells *in vitro* was investigated, as a previous step to study heterogeneous oxygen distributions simulating *in vivo* experiments. Fixing $G_0 = 0.25$ mmHg/Gy and $k_{\mathrm{ROD}} = 1$ mmHg, equation (4.1) was employed to obtain oxygen depletion curves during FLASH-RT for different radiation doses and baseline oxygen levels. On the other hand, the oxygen partial pressure remained steady during irradiation with conv-RT. Then, the SFs for conv-RT and FLASH-RT were obtained as described in Section 4.3.

The study was limited to oxygenations in the range 1–40 mmHg, as it was previously reported (both from experimental [142] and modeling studies [143]) that for oxygen pressures above 30–40 mmHg the FLASH effect is not observed.

Different values of the radiosensitivity parameters, α_{ox} and β_{ox}, reported in Table 4.5, were investigated. These values were set to be iso-effective for a dose of 20 Gy using the LQ model (1.1).

$\alpha_{\mathrm{ox}}/\beta_{\mathrm{ox}}$ (Gy)	α_{ox} (Gy^{-1})	β_{ox} (Gy^{-2})
3 (low)	0.157	0.052
10 (medium)	0.400	0.040
20 (high)	0.600	0.030
∞	1.200	0

Table 4.5: Radiosensitivity parameters and ratios employed in the *in vitro* study. These values were set to be iso-effective for a dose of 20 Gy with conv-RT.

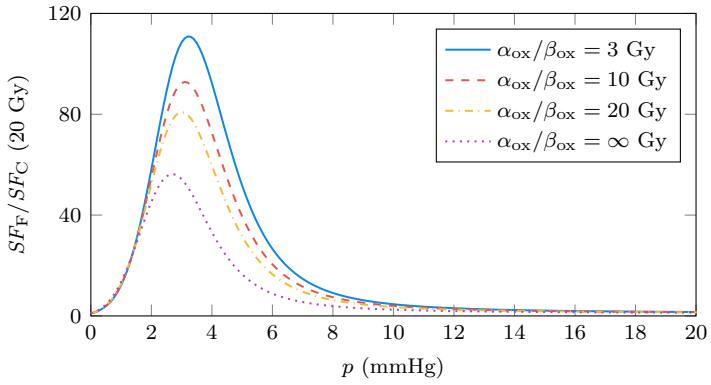

Figure 4.3: Ratio of Surviving Fractions (SFs) between FLASH-RT (SF_{F}) and conv-RT (SF_{C}) for a dose of 20 Gy versus the oxygenation status of the cells. A dose rate of 100 Gy s^{-1} was employed to obtain SF_{F}.

Figure 4.3 illustrates the difference in SF between conv-RT and FLASH-RT versus the oxygenation for a radiation dose of 20 Gy. It is observed that differences tend to zero in the limits $p \to \infty$ and $p \to 0$, the reason being that at large oxygen concentrations, the effect of ROD on the OERs becomes insignificant and that ROD is limited at very low oxygen concentrations. The maximum differences are observed approximately in the range 2–6 mmHg. The location of this range depends on both the modeling of ROD and the modeling of the OER, particularly in the parameter k_{m}, which was set to 3.28 mmHg, as reported in Table 4.3.

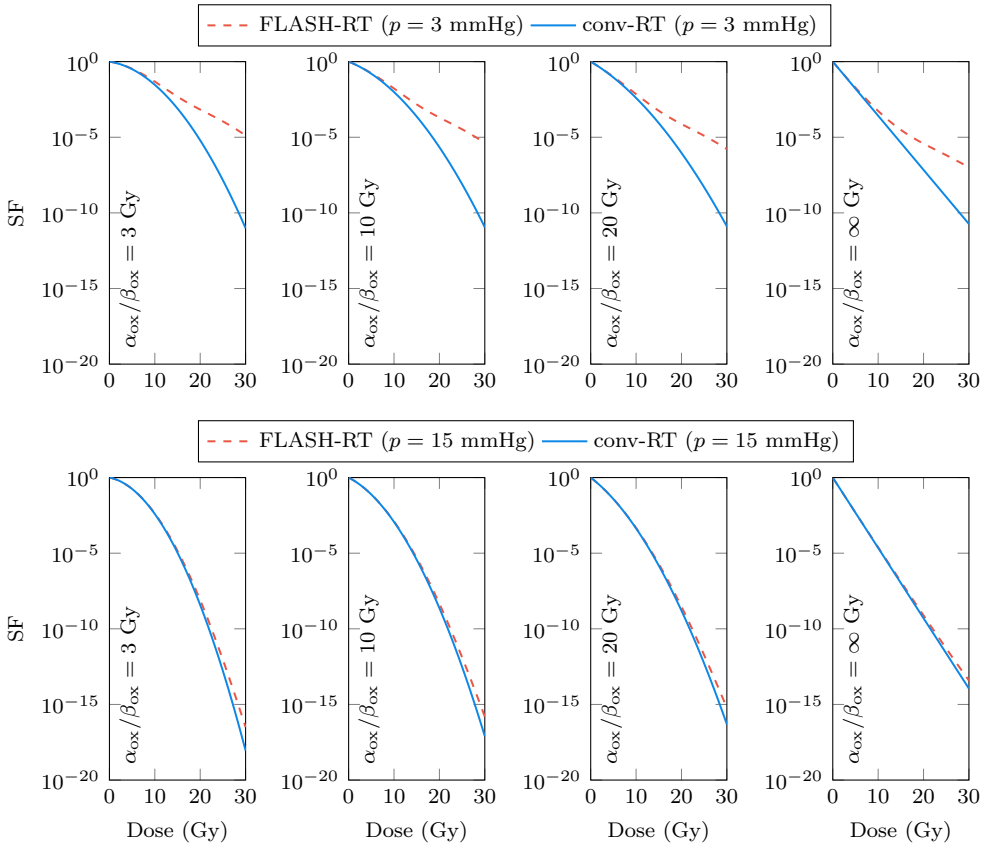

Figure 4.4: Surviving Fraction (SF) versus dose curves for cells irradiated with conv-RT and FLASH-RT at two oxygenation levels (*poorly oxygenated*, $p = 3$ mmHg, *moderately-well oxygenated*, $p = 15$ mmHg). Results are presented for $\alpha_{\mathrm{ox}}/\beta_{\mathrm{ox}} \in \{3, 10, 20, \infty\}$ Gy.

Figure 4.4 shows the SF versus dose curves resulting from the *in vitro* study. The differences in SF between FLASH-RT and conv-RT match qualitatively well with previously reported experimental studies [142], showing higher SFs in FLASH-RT. Moreover, the obtained curves reveal the influence of oxygen on these differences when comparing *poorly* and *moderately-well oxygenated* statuses, respectively represented by $p = 3$ mmHg and $p = 15$ mmHg.

4.6.3 Model fitting to preclinical tumor volume curves

The optimization techniques mentioned in Section 4.5.2, were used to fit the tumor response model given by equations (4.8)–(4.11) to the datasets of tumor volume dynamics after conv-RT and FLASH-RT summarized in Table 4.2. Parameters α_{ox}, λ, K, ϕ and the initial volume, V_0 (being $C_{\mathrm{d}}(0) = 0$), were fitted while the ratio $\alpha_{\mathrm{ox}}/\beta_{\mathrm{ox}}$ was set to 10 Gy. To find the best fit considering the oxygen distribution and the radiolytic consumption rate, the optimization process was performed separately for each oxygen distribution in the H sample, using the same G_0 parameter values assigned for the *in vivo* experiment described in Section 4.6.1. Then, the best-fitting distribution and parameters were selected as those that minimize the cost function, defined in Section 4.5.2 (however, differences in the cost value between the 100 optimizations were minimal, having an increasing value of α_{ox} with decreasing oxygenation).

As summarized in Table 4.2, the two experiments performed by Diffenderfer *et al.* [72] corresponded to the same tumor line but for different radiation doses. Thus, the same set of model parameters were used for both datasets. On the contrary, the experiments reported by Zhu *et al.* [140] were treated separately as belonging to different tumor lines which may present different response parameters. Additionally, three distinct initial volumes, one for each curve of control, conv-RT, and FLASH-RT, were used to emulate noticeable differences in pre-irradiation volumes observed in the experiment with Py8119 tumors.

The best-fitting curves and experimental data are shown in Figure 4.5. While the best-fitting parameters for each experimental study are summarized in Table E.1.

4.6.4 Analysis of conv-RT and FLASH-RT iso-effectiveness from dose-volume curves

Building on the results of the previous section, the significance of the differences between control, conv-RT and FLASH-RT tumor growth curves was investigated. The study was performed following the next steps:

Step 1: A random growth curve was generated by sampling parameters from a normal distribution with the best-fitting parameters reported in Table E.1 as mean values and a 20% relative standard deviation (which qualitatively fits the

error bars of the experimental studies), sampling an oxygenation from the H sample, and assigning a treatment group (control, FLASH-RT, conv-RT).

Step 2: Step 1 was repeated to obtain the sample size of each experimental study.

Step 3: The ANCOVA methodology was used to detect significant differences between groups, as described in Section 4.5.5.

Step 4: Steps 1–3 were repeated 1000 times to achieve enough statistics.

Figure 4.6 illustrates one of the resulting simulations from following Steps 1 and 2 to analyze the differences between conv-RT and FLASH-RT groups.

A very large percentage of the simulated experiments showed a significant difference between control and FLASH-RT or conv-RT. However, only a small fraction of the simulated experiments showed a significant difference between FLASH-RT and conv-RT, respectively 15.8% and 28.6%, as shown in Figure 4.7. The data from the experiment by Zhu *et al.* [140] in Py8119 tumors ((c) in Figure 4.5) was excluded from this analysis because the baseline differences in volume between groups lead to significant differences that cannot be attributed to the treatments.

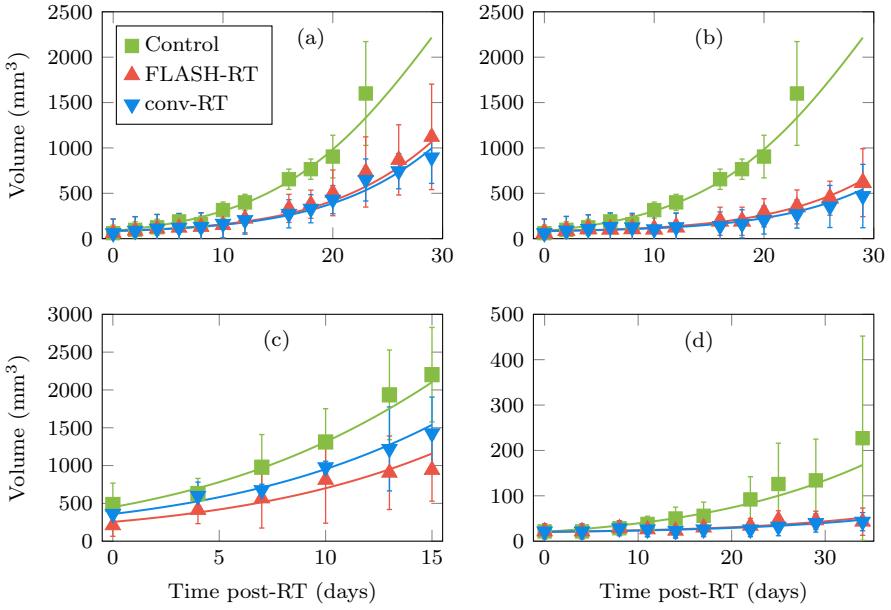

Figure 4.5: Best fits of tumor growth curves (mean values and standard deviations) for control, FLASH-RT, and conv-RT groups, reported by Diffenderfer *et al.* [72] ((a) MH641905 12 Gy, (b) MH641905 18 Gy) and Zhu *et al.* [140] ((c) Py8119 9.5 Gy, (d) Py230 9.5 Gy).

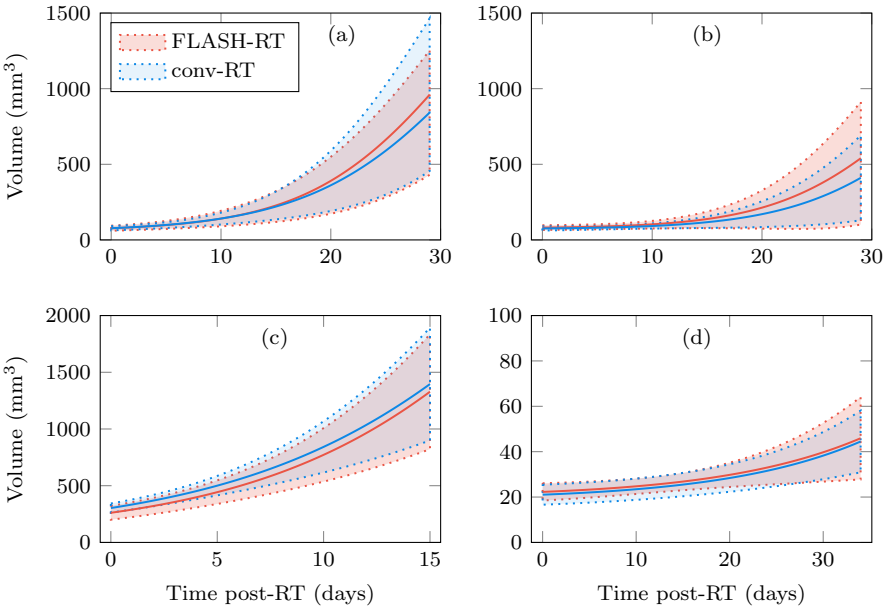

Figure 4.6: Example of the comparison between tumor growth curves after irradiation with FLASH-RT and conv-RT from fits to the data reported by Diffenderfer *et al.* [72] ((a) MH641905 12 Gy, (b) MH641905 18 Gy) and Zhu *et al.* [140] ((c) Py8119 9.5 Gy, (d) Py230 9.5 Gy). The solid lines represent the mean values and the shadow areas represent the standard deviation of populations with the sample size given in Table 4.2 for each experiment.

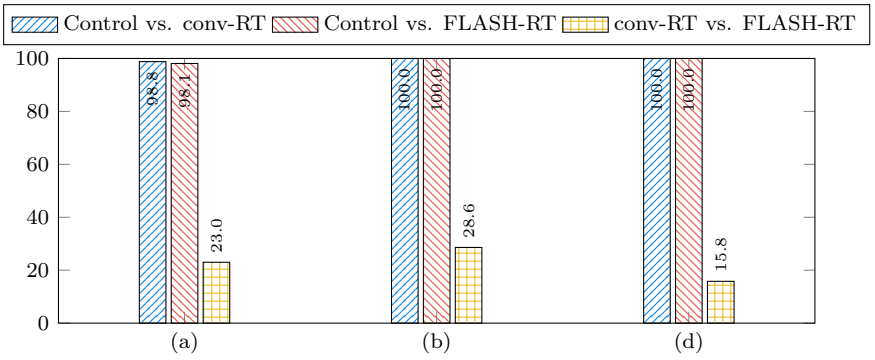

Figure 4.7: Percentage of simulated experiments showing a significant difference (p-value < 0.05) between control, conv-RT, and FLASH-RT groups, for simulations based on the experimental data reported by Diffenderfer *et al.* [72] and Zhu *et al.* [140], summarized in Table 4.2.

4.6.5 Estimation of the effect of ROD on TCP

Once the effect of ROD on the SF of tumor cells *in vitro* was estimated, the obtained results were extrapolated to TCP versus dose curves *in vivo*. For that purpose, TCP was computed on simulated tumors with heterogeneous oxygen distributions, following the methodology described in Section 4.5.7. Different α_{ox}/β_{ox} values were studied and reported in Table 4.6. Fixing $\alpha_{ox} = 0.4$ Gy^{-1} and $\alpha_{ox}/\beta_{ox} = 10$ Gy as reference values, the other radiosensitivity parameters, α_{ox}, were set to yield the same D_{50} with conv-RT. Populations of 1000 simulated tumors for each group (radiosensitivity ratio) were generated using the data on Table 4.6 and $N_0 = 10^6$ tumor cells as mean values for parameter perturbations.

α_{ox}/β_{ox} (Gy)	α_{ox} (Gy^{-1})	β_{ox} (Gy^{-2})
3 (low)	0.175	0.058
10 (medium)	0.400	0.040
20 (high)	0.553	0.028

Table 4.6: Radiosensitivity parameters and ratios employed in the *in vivo* study. These values were set to yield the same D_{50} (dose at which TCP is 0.5) with conv-RT.

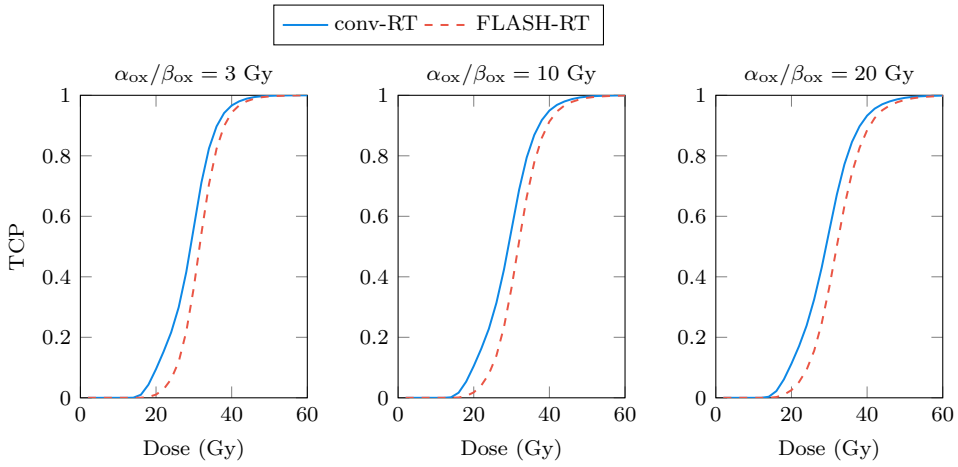

Figure 4.8: Tumor Control Probability (TCP)-dose curves for heterogeneously oxygenated tumors with different α_{ox}/β_{ox} ratios, irradiated with conv-RT and FLASH-RT.

Figure 4.8 presents the resulting TCP-dose curves for each group. Using the dose D_{50}, described in Section 4.5.7, as a metric to compare the potential differences in TCP curves between both radiation modalities, the figure shows that FLASH-RT brings higher D_{50} values, as reported in Table 4.7. To account for the effect of the

α_{ox}/β_{ox} ratio on the differences in D_{50} between FLASH-RT and conv-RT, the associated BED was calculated from equation (1.11). Table 4.7 shows an increasing BED with decreasing α_{ox}/β_{ox} ratio. Thus, this study suggests that TCP loss with FLASH-RT becomes bigger in tumors with low α_{ox}/β_{ox} ratios.

α_{ox}/β_{ox} (Gy)	D_{50}^{C} (Gy)	D_{50}^{F} (Gy)	ΔD_{50} (Gy)	$BED(\Delta D_{50})$
3	29.17	31.52	2.35	4.19
10	29.17	31.78	2.61	3.29
20	29.16	31.98	2.82	3.22

Table 4.7: Differences in D_{50} between conv-RT and FLASH-RT according to the α_{ox}/β_{ox} ratio. Differences are reported in grays (ΔD_{50}), and the corresponding Biologically Effective Dose (BED) to account for the influence of the radiosensitivity ratio.

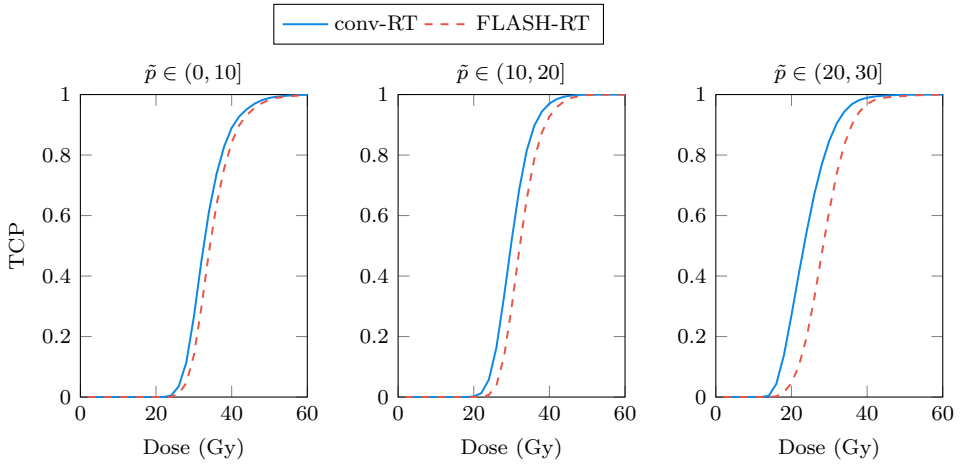

Figure 4.9: Tumor Control Probability (TCP)-dose curves for conv-RT (solid lines) and FLASH-RT (dashed lines) in tumors with heterogeneous oxygen levels according to their median oxygen partial pressure, $\tilde{p}$: *poorly oxygenated* ($\tilde{p} \leq 10$ mmHg), *moderately oxygenated* ($10 < \tilde{p} \leq 20$ mmHg), and *well oxygenated* tumors ($\tilde{p} > 20$ mmHg). The α_{ox}/β_{ox} ratio was set to 10 Gy.

A similar study was performed to investigate the influence of tumor oxygenation on TCP. For that purpose, the radiosensitivity ratio was set to $\alpha_{ox}/\beta_{ox} = 10$ Gy and the corresponding tumor population was split into three groups according to their median oxygen distribution, $\tilde{p}$: *poorly oxygenated* ($\tilde{p} \leq 10$ mmHg), *moderately oxygenated* ($10 < \tilde{p} \leq 20$ mmHg), and *well oxygenated* tumors ($\tilde{p} > 20$ mmHg). TCP-dose curves were obtained separately for each group, both for FLASH-RT and conv-RT, obtaining the curves presented in Figure 4.9. Moreover, the resulting D_{50} and D_{90} are summarized in Table 4.8 for both RT modalities, along with their relative ratio. When analyzing the

TCP-dose curves according to the median oxygenation, differences between FLASH-RT and conv-RT seem to be more important in *well oxygenated* than *poorly oxygenated* tumors (as qualitatively shown in Figure 4.9 and quantitatively shown in Table 4.8).

$\tilde{p}$ (mmHg)	D_{50}^{C} (Gy)	D_{50}^{F} (Gy)	D_{50}^{F}/D_{50}^{C}	D_{90}^{C} (Gy)	D_{90}^{F} (Gy)	D_{90}^{F}/D_{90}^{C}
$(0, 10]$	32.56	34.23	1.05	40.43	42.06	1.04
$(10, 20]$	29.83	32.19	1.08	36.11	38.86	1.08
$(20, 30]$	23.30	28.36	1.22	31.79	35.96	1.13

Table 4.8: Differences in D_{50} and D_{90} between conv-RT (D_{50}^{C}, D_{90}^{C}) and FLASH-RT (D_{50}^{F}, D_{90}^{F}) in tumors with heterogeneous oxygen levels according to their median oxygen partial pressures, $\tilde{p}$. The α_{ox}/β_{ox} ratio was set to 10 Gy.

4.7 Discussion

This study investigates the possibility that FLASH-RT might not preserve TCP. The followed approach is based on the mathematical modeling of oxygen distribution in tissues through differential equations, the LQ model with OERs to account for the oxygen effect on irradiated cells, a simple model of tumor growth after irradiation, and the LQ-Poisson TCP formulation to calculate the TCP of different treatments. With these tools, a systematic and progressive study was performed by analyzing experimental data of ROD in solutions and *in vivo*, estimating SFs *in vitro*, and simulating tumor growth in preclinical irradiated tumors. Finally, the obtained results were extrapolated to the analysis of TCP-dose curves in a clinical setting, and the potential effect of ROD on the clinical iso-effectiveness of FLASH-RT (in terms of TCP).

The proposed models can fit data of ROD measurements in solutions and *in vivo* (Figures 4.1 and 4.2), qualitatively reproduce the SF versus dose curves for FLASH-RT and conv-RT (Figure 4.4), and the growth curves of irradiated tumors (Figure 4.5). The study suggests that even if ROD may lead to differences in the SF of tumor cells between conv-RT and FLASH-RT, such differences may be not large enough to induce significant differences in the growth curves of preclinical tumors (that are far from control) when evaluated in small groups of animals (5–15), as shown in Figure 4.6. However, these differences may affect the TCPs obtained with FLASH-RT and conv-RT, where the model predicts significantly lower TCPs for FLASH-RT, as reported in Figure 4.7. In this regard, the obtained results are in agreement with those presented by Liew *et al.* [138].

On the one hand, TCP loss with FLASH-RT seems more important in tumors with low α/β ratios (Figure 4.8), where the ROD effect is expected to cause more cell sparing, as the β-term is more sensitive to oxygenation changes (see equations (1.4)–(1.6)).

On the other hand, counterintuitive results were found when analyzing the role of tumor oxygenation on the ROD effect between simulated tumors with heterogeneous oxygen distributions (*in vivo*) and the SFs for cells at different oxygenation levels (*in vitro*). It is explicitly shown in Figures E.3 and 4.9 that the TCP-dose curves assuming spatially homogeneous oxygenations present the opposite behaviour than was observed for the *in vivo* simulations. The ROD effect is more relevant in *poorly oxygenated* cells, a trend that the simulations reproduced for homogeneously oxygenated cells/tumors. However, when analyzing the TCP-dose curves of heterogeneously oxygenated tumors according to their oxygenation status, *well oxygenated* tumors are more affected by the ROD effect than tumors with *moderate* and *poor* oxygenations (defined in this work as median oxygen partial pressure under 20 mmHg and 10 mmHg, respectively). This apparent contradiction can be explained by the complex interplay between oxygen heterogeneity, the role of the OERs, and ROD. *Well oxygenated* tumors are controlled with lower doses than *moderately/poorly oxygenated* tumors due to the OER effect, as shown in Table 4.8. However, tumor control is mostly affected by low oxygenation regions, which are present even in *well oxygenated* tumors (as shown in the oxygen histograms reported in Figures E.1 and E.2), and the ROD effect on the SF is also more important in low oxygenation regions, particularly in the 2–6 mmHg range, as shown in Figure 4.3. Thus, in spite of a smaller fraction of cells being affected by the ROD effect in *well oxygenated* tumors, the lower doses needed to achieve control make the overall FLASH effect larger than for *moderately* and *poorly oxygenated* tumors. Intuitively, a small fraction of cells is shifted from $p \sim$ 2–6 mmHg to $\sim$ 0 mmHg in *well oxygenated* tumors, while a large fraction of cells undergoes the same shift for *poorly oxygenated* tumors. However, that small fraction of cells cannot be killed by the dose $D \approx 32$ Gy needed to achieve 90% control for those tumors with conv-RT (see Table 4.8), causing a large drop of TCP for FLASH-RT and thus requiring a much larger dose to compensate for the ROD effect. On the contrary, the larger fraction of cells undergoing that shift for *poorly oxygenated* tumors can still be adequately controlled with the dose $D \approx$ 40 Gy needed to achieve 90% for those tumors, therefore causing a more modest drop of TCP and requiring less of a boost to compensate for the ROD effect. These results may be of interest in a hypothetical clinical trial with tumors assigned to groups receiving different doses according to their oxygenation/hypoxic status. In that context, the ROD effect might have a more detrimental effect on *well oxygenated* tumors (receiving lower doses) than on *poorly oxygenated* tumors (receiving higher doses).

Ideally, it would be of interest to experimentally investigate not only the growth curves of tumors irradiated with FLASH-RT and conv-RT but also the TCPs achieved with those treatments, even if this is experimentally complex due to the low radiosensitivity of tumor models and the large number of animals that would be necessary. Notably, recent advances have been made; a study by Sørensen *et al.* [144] investigated tumor control versus dose for FLASH-RT and conv-RT in mice tumors. Although they found no statistically significant differences between conv-RT and FLASH-RT,

reported D_{50} values were slightly larger for FLASH-RT, and the uncertainty in the reported values ($\sim$ 7 Gy wide 95% confidence intervals) was too large to exclude differences of 2–3 Gy, as those reported in Table 4.8. Studies like the one conducted by Sørensen *et al.* [144] seem of paramount importance, not only to establish the iso-effectiveness of FLASH-RT with a more clinically relevant endpoint, but also to guide modeling studies on the mechanisms behind the FLASH effect.

Taylor *et al.* [84] found a similar behavior when analyzing the effect of FLASH-RT on SFs. On the one hand, they showed that the FLASH effect is larger for low α/β ratios. On the other hand, they also found that oxygen heterogeneity can lead to a larger FLASH effect in *well oxygenated* tissues than in *poorly oxygenated* tissues, which might seem counterintuitive based on the dependence of the OERs on the oxygen partial pressure. Interestingly, they showed that this apparently contradictory effect becomes more evident the higher the heterogeneity of the oxygen distribution, by comparing oxygen distributions obtained from randomly placed and regular networks of vessels (which lead to more homogeneous oxygenations). The study presented in Section 4.6.5 suggests that this behavior holds when analyzing TCPs with more realistic oxygen distributions based on experimentally characterized vascular networks.

The results reported in this study are dependent on the parameter values used in it, which were obtained from the literature and model fitting to experimental datasets. For example, the rate of radiolytic oxygen consumption was obtained by analyzing ROD in solutions, as shown in Section 4.6.1. The applicability of these model solutions in mimicking cellular cultures has been debated. The CELL solution partially mimics the intracellular environment [101], and therefore results obtained for this solution would be more representative of the *in vivo* response. However, a relatively *conservative* value of 0.25 mmHg/Gy was used rather than 0.40 mmHg/Gy. Higher values would increase the FLASH sparing of tumors investigated in this work. Besides, the maximum OERs would also affect the results. OER_α and OER_β were set to 2.5, a value widely employed in the modeling literature, although other authors have reported values below 2 [145]. Lower values for OER_α and OER_β would result in less FLASH effect and a lower loss of TCP.

It cannot be discarded that other effects that have not been modeled in this work, like radiation-induced immune effects or differences in the production yield of reactive species between tumor and non-tumor cells [79–81, 146], can contribute to tumor control and maintain the iso-effectiveness of FLASH-RT.

Chapter 5

Conclusions

"Part of the journey is the end."
— Tony Stark, *Avengers: Endgame.*

This thesis dissertation has faced the challenge of proposing new mathematical models to describe the tumor response to novel advanced radiotherapy techniques, particularly on radioimmunotherapy and FLASH radiotherapy. The presented models allow the investigation of the mechanisms behind the effect of the treatments, to formulate hypotheses about optimal treatment strategies, and to analyze contradicting evidence from experimental studies.
This chapter summarizes the conclusions derived from the performed research and includes some notes on future work.

5.1 General conclusions

Mathematical models arose soon after the development of RT to treat cancer as valuable tools to assist clinicians in treatment planning. Particularly, the LQ model was paramount in the design of novel fractionations, dose optimization, and the estimation of radiation-derived toxicity in normal tissues. However, the classical models became insufficient to describe more advanced RT techniques that emerged over the last decades. This thesis presented novel response models to RIT and FLASH-RT.

Mathematical modeling was based on the use of differential equations to describe the dynamics of cells and other agents involved in tumor response to RT, including ODEs, DDEs, IDEs, and PDEs. Besides, the presented models were tested and validated by fitting them to preclinical data obtained from the literature. Different optimization tools were used for that purpose, through user-defined functions and MATLAB software. The general methods used in the investigation were described in Chapter 2.

5.2 Conclusions on radioimmunotherapy

RIT through ICIs has experimentally shown to increase effectiveness compared to the individual use of RT and IT as single treatments. With the introduction of the first ICI drugs in the clinical scenario over the last decade, how to design optimal RIT treatments continues being an active research field, as the synergistic effect of RT and IT is not fully understood.

Biomathematical models can help to interpret and analyze experimental data of the synergy between RT and IT, assist in the design of more effective RIT, and potentially facilitate the implementation of optimized strategies. A new mechanistic model for RIT with αCTLA4 and αPD(L)1 antibodies was proposed in Chapter 3. This model presents some novelties compared to those published in recent years. On the one hand, DDEs were employed to include the effect of biological delays related to the transportation of immune agents between the tumor and lymphoid organs. On the other hand, a Markov stochastic approach was used to estimate TCP.

The proposed model can fit preclinical data of tumor volume evolution during and after RIT treatments with different RT fractionation schedules combined with αCTLA4 or αPDL1, as well as tumor control rates resulting from RIT with αCTLA4.

The performed study suggests that a good understanding of the biological delays associated with such therapies, the biokinetics of IT drugs, and the interplay among them, may be of paramount importance for designing optimal RIT schedules. In agreement with preclinical data, the model predicts that delivering αCTLA4 IT too soon or too late after starting the radiation treatment, may be suboptimal. Moreover, extreme-hypofractionated and conventional RT schedules may fail to keep therapeutic

numbers of T-cells in the tumor, thus moderate hypofractionation is likely to be the preferred strategy.

Future work would involve model fitting to new published data. Particularly, tumor control rates in RIT with αPD(L)1, as the interplay between the biokinetics of IT drugs and the biological delays might suggest different optimal strategies from those proposed for αCTLA4. Furthermore, bringing the model closer to the clinical scenario would entail a necessary simplification of the equations to a simpler expression, similar to that of classical models in RT.

5.3 Conclusions on FLASH radiotherapy

FLASH-RT has shown *in vivo* its potential to spare normal tissue while seemingly maintaining the effectiveness of conv-RT on tumors. Understanding why the protective effect is not observed in tumors remains an ongoing area of research. As FLASH-RT has moved closer to clinical application in recent years, it is important to guarantee that clinical trials will not lead to TCP loss compared to conv-RT, and, if necessary, to boost the radiation dose to compensate for such effect.

The role of ROD on the FLASH effect has been debated in several works. Despite the fact that oxygen depletion in radiation delivery at UHDRs increases cell radioresistance, some studies suggest that this phenomenon cannot fully explain the protective effect, pointing to other immune and physicochemical factors. This thesis investigates the apparent iso-effectiveness of FLASH-RT and conv-RT attending to the role of ROD. In this context, tumor oxygenation was modeled through a reaction-diffusion PDE, and a simple mechanistic model was proposed to describe tumor response to FLASH-RT and conv-RT. The presented models can fit preclinical data of oxygen depletion measurements and tumor volume response to the treatments.

The performed study suggests that ROD may lead to differences in the SF of tumor cells between both radiation modalities, which may not be large enough to induce significant differences in the volume evolution of preclinical tumors (that are far from control). Nonetheless, these differences may be significant in clinical TCP, especially in tumors with low α/β radiosensitivity ratios, where the ROD effect is expected to cause more cell sparing. Besides, well-oxygenated tumors presenting heterogeneous oxygen distributions (defined in this work as those with median partial pressure over 20 mmHg) may show increased TCP loss when treated with the doses expected to achieve a certain TCP with conv-RT. The obtained results raised concerns on the use of tumor growth delay studies to state the iso-effectiveness of FLASH-RT and conv-RT, as they may not be sensitive enough to effects that would otherwise have major clinical consequences. It would be of special interest to experimentally investigate not only the growth curves of tumors but also the achieved TCP to properly assess the iso-effectiveness of FLASH-RT and conv-RT.

Future work would comprehend the incorporation to the response model of other factors that can compensate TCP loss due to ROD and maintain the iso-effectiveness between conv-RT and FLASH-RT, supporting the experimental evidence.

Bibliography

[1] S. Gianfaldoni, R. Gianfaldoni, U. Wollina, *et al.*, "An overview on radiotherapy: From its history to its current applications in dermatology", *Open access Macedonian Journal of Medical Sciences*, vol. 5, no. 4, pp. 521–5, 2017. DOI: 10.3889/oamjms.2017.122.

[2] E. H. Grubbé, "Priority in the therapeutic use of X-rays", *Radiology*, vol. 21, no. 2, pp. 156–62, 1933. DOI: 10.1148/21.2.156.

[3] H. Becquerel and P. Curie, "Action physiologique des rayons du radium", *Comptes Rendus de l'Académie des Sciences*, vol. 132, pp. 1289–91, 1901.

[4] E. O. Lawrence and M. S. Livingston, "The production of high speed light ions without the use of high voltages", *Physical Review*, vol. 40, no. 1, pp. 19–35, 1932. DOI: 10.1103/PhysRev.40.19.

[5] H. Coutard, "Principles of X ray therapy of malignant diseases", *The Lancet*, vol. 224, no. 5784, pp. 1–8, 1934. DOI: 10.1016/S0140-6736(00)90085-0.

[6] D. W. Fry, R. B. R. -S. -Harvie, L. B. Mullett, *et al.*, "A travelling-wave linear accelerator for 4-MeV. electrons", *Nature*, vol. 162, no. 4126, pp. 859–61, 1948. DOI: 10.1038/162859a0.

[7] F. G. Herrera, J. Bourhis, and G. Coukos, "Radiotherapy combination opportunities leveraging immunity for the next oncology practice: Radiation-immunotherapy combinations", *CA: A Cancer Journal for Clinicians*, vol. 67, no. 1, pp. 65–85, 2017. DOI: 10.3322/caac.21358.

[8] C. Park, L. Papiez, S. Zhang, *et al.*, "Universal survival curve and single fraction equivalent dose: Useful tools in understanding potency of ablative radiotherapy", *International Journal of Radiation Oncology * Biology * Physics*, vol. 70, no. 3, pp. 847–52, 2008. DOI: 10.1016/j.ijrobp.2007.10.059.

[9] S. S. Lo, A. J. Fakiris, E. L. Chang, *et al.*, "Stereotactic body radiation therapy: A novel treatment modality", *Nature Reviews Clinical Oncology*, vol. 7, no. 1, pp. 44–54, 2010. DOI: 10.1038/nrclinonc.2009.188.

[10] B. G. Douglas and J. F. Fowler, "The effect of multiple small doses of X rays on skin reactions in the mouse and a basic interpretation", *Radiation Research*, vol. 66, no. 2, pp. 401–26, 1976. DOI: 10.2307/3574407.

[11] C. W. Song, Y. J. Lee, R. J. Griffin, *et al.*, "Indirect tumor cell death after high-dose hypofractionated irradiation: Implications for stereotactic body radiation therapy and stereotactic radiation surgery", *International Journal of Radiation Oncology * Biology * Physics*, vol. 93, no. 1, pp. 166–72, 2015. DOI: 10.1016/j.ijrobp.2015.05.016.

[12] M. García-Barros, F. Paris, C. Cordon-Cardo, *et al.*, "Tumor response to radiotherapy regulated by endothelial cell apoptosis", *Science*, vol. 300, no. 5622, pp. 1155–9, 2003. DOI: 10.1126/science.1082504.

[13] H. J. Park, R. J. Griffin, S. Hui, *et al.*, "Radiation-induced vascular damage in tumors: Implications of vascular damage in ablative hypofractionated radiotherapy (SBRT and SRS)", *Radiation Research*, vol. 177, no. 3, pp. 311–27, 2012. DOI: 10.1667/RR2773.1.

[14] C. W. Song, E. Glatstein, L. B. Marks, *et al.*, "Biological principles of stereotactic body radiation therapy (SBRT) and stereotactic radiation surgery (SRS): Indirect cell death", *International Journal of Radiation Oncology * Biology * Physics*, vol. 110, no. 1, pp. 21–34, 2021. DOI: 10.1016/j.ijrobp.2019.02.047.

[15] A. Filatenkov, J. Baker, A. M. S. Mueller, *et al.*, "Ablative tumor radiation can change the tumor immune cell microenvironment to induce durable complete remissions", *Clinical Cancer Research*, vol. 21, no. 16, pp. 3727–39, 2015. DOI: 10.1158/1078-0432.CCR-14-2824.

[16] L. de la Maza, M. Wu, L. Wu, *et al.*, "*In situ* vaccination after accelerated hypofractionated radiation and surgery in a mesothelioma mouse model", *Clinical Cancer Research*, vol. 23, no. 18, pp. 5502–13, 2017. DOI: 10.1158/1078-0432.CCR-17-0438.

[17] Y. Wang, Z. G. Liu, H. Yuan, *et al.*, "The reciprocity between radiotherapy and cancer immunotherapy", *Clinical Cancer Research*, vol. 25, no. 6, pp. 1709–17, 2019. DOI: 10.1158/1078-0432.CCR-18-2581.

[18] L. Deng, H. Liang, B. Burnette, *et al.*, "Irradiation and anti–PD-L1 treatment synergistically promote antitumor immunity in mice", *The Journal of Clinical Investigation*, vol. 124, no. 2, pp. 687–95, 2014. DOI: 10.1172/JCI67313.

[19] Y. Lee, S. L. Auh, Y. Wang, *et al.*, "Therapeutic effects of ablative radiation on local tumor require CD8+ T cells: Changing strategies for cancer treatment", *Blood, The Journal of the American Society of Hematology*, vol. 114, no. 3, pp. 589–95, 2009. DOI: 10.1182/blood-2009-02-206870.

[20] J. He, Y. Yin, T. A. Luster, *et al.*, "Antiphosphatidylserine antibody combined with irradiation damages tumor blood vessels and induces tumor immunity in a rat model of glioblastoma", *Clinical Cancer Research*, vol. 15, no. 22, pp. 6871–80, 2009. DOI: 10.1158/1078-0432.CCR-09-1499.

[21] E. J. Moding, K. D. Castle, B. A. Perez, *et al.*, "Tumor cells, but not endothelial cells, mediate eradication of primary sarcomas by stereotactic body radiation therapy", *Science Translational Medicine*, vol. 7, no. 278, 278ra34, 2015. DOI: 10.1126/scitranslmed.aaa4214.

[22] J. A. Torok, P. Oh, K. D. Castle, *et al.*, "Deletion of ATM in tumor but not endothelial cells improves radiation response in a primary mouse model of lung adenocarcinoma", *Cancer Research*, vol. 79, no. 4, pp. 773–82, 2019. DOI: 10.1158/0008-5472.CAN-17-3103.

[23] K. Deland, J. S. Mercer, D. M. Crabtree, *et al.*, "Radiosensitizing the vasculature of primary brainstem gliomas fails to improve tumor response to radiation therapy", *International Journal of Radiation Oncology * Biology * Physics*, vol. 112, no. 3, pp. 771–9, 2022. DOI: 10.1016/j.ijrobp.2021.09.047.

[24] J. M. Brown, D. J. Carlson, and D. J. Brenner, "The tumor radiobiology of SRS and SBRT: Are more than the 5 Rs involved?", *International Journal of Radiation Oncology * Biology * Physics*, vol. 88, no. 2, pp. 254–62, 2014. DOI: 10.1016/j.ijrobp.2013.07.022.

[25] R. Ruggieri, P. Stavrev, S. Naccarato, *et al.*, "Optimal dose and fraction number in SBRT of lung tumours: A radiobiological analysis", *Physica Medica*, vol. 44, pp. 188–95, 2017. DOI: 10.1016/j.ejmp.2016.12.012.

[26] J. P. Kirkpatrick, J. J. Meyer, and L. B. Marks, "The linear-quadratic model is inappropriate to model high dose per fraction effects in radiosurgery", *Seminars in Radiation Oncology*, vol. 18, no. 4, pp. 240–3, 2008. DOI: 10.1016/j.semradonc.2008.04.005.

[27] D. J. Brenner, "The linear-quadratic model is an appropriate methodology for determining isoeffective doses at large doses per fraction", *Seminars in Radiation Oncology*, vol. 18, no. 4, pp. 234–39, 2008. DOI: 10.1016/j.semradonc.2008.04.004.

[28] C. W. Song, H. Park, R. J. Griffin, *et al.*, "Radiobiology of stereotactic radiosurgery and stereotactic body radiation therapy", in *Technical basis of radiation therapy: Practical clinical applications*. Springer Berlin Heidelberg, 2012, pp. 51–61, ISBN: 9783642115721. DOI: 10.1007/174_2011_264.

[29] P. W. Sperduto, C. W. Song, J. P. Kirkpatrick, *et al.*, "A hypothesis: Indirect cell death in the radiosurgery era", *International Journal of Radiation Oncology * Biology * Physics*, vol. 91, no. 1, pp. 11–3, 2015. DOI: 10.1016/j.ijrobp.2014.08.355.

[30] C. W. Song, M. S. Kim, L. C. Cho, *et al.*, "Radiobiological basis of SBRT and SRS", *International Journal of Clinical Oncology*, vol. 19, no. 4, pp. 570–8, 2014. DOI: 10.1007/s10147-014-0717-z.

[31] M. Guerrero and M. Carlone, "Mechanistic formulation of a lineal-quadratic-linear (LQL) model: Split-dose experiments and exponentially decaying sources", *Medical Physics*, vol. 37, no. 8, pp. 4173–81, 2010. DOI: 10.1118/1.3456927.

[32] M. Guerrero and X. A. Li, "Extending the linear-quadratic model for large fraction doses pertinent to stereotactic radiotherapy", *Physics in Medicine & Biology*, vol. 49, no. 20, pp. 4825–35, 2004. DOI: 10.1088/0031-9155/49/20/012.

[33] A. Gago-Arias, S. Neira, M. Pombar, *et al.*, "Evaluation of indirect damage and damage saturation effects in dose-response curves of hypofractionated radiotherapy of early-stage NSCLC and brain metastases", *Radiotherapy and Oncology*, vol. 161, pp. 1–8, 2021. DOI: 10.1016/j.radonc.2021.05.012.

[34] R. Serre, S. Benzekry, L. Padovani, *et al.*, "Mathematical modeling of cancer immunotherapy and its synergy with radiotherapy", *Cancer Research*, vol. 76, no. 17, pp. 4931–40, 2016. DOI: 10.1158/0008-5472.CAN-15-3567.

[35] J. Poleszczuk and H. Enderling, "The optimal radiation dose to induce robust systemic anti-tumor immunity", *International Journal of Molecular Sciences*, vol. 19, no. 11, p. 3377, 2018. DOI: 10.3390/ijms19113377.

[36] S. J. McMahon, "The linear quadratic model: Usage, interpretation and challenges", *Physics in Medicine & Biology*, vol. 64, no. 1, 01TR01, 2019. DOI: 10.1088/1361-6560/aaf26a.

[37] A. Gago-Arias, P. Aguiar, I. Espinoza, *et al.*, "Modelling radiation-induced cell death and tumour re-oxygenation: Local versus global and instant versus delayed cell death", *Physics in Medicine & Biology*, vol. 61, no. 3, pp. 1204–16, 2016. DOI: 10.1088/0031-9155/61/3/1204.

[38] B. J. Moeller, R. A. Richardson, and M. W. Dewhirst, "Hypoxia and radiotherapy: Opportunities for improved outcomes in cancer treatment", *Cancer and Metastasis Reviews*, vol. 26, pp. 241–48, 2007. DOI: 10.1007/s10555-007-9056-0.

[39] A. S. E. Ljungkvist, J. Bussink, P. F. J. W. Rijken, *et al.*, "Vascular architecture, hypoxia, and proliferation in first-generation xenografts of human head-and-neck squamous cell carcinomas", *International Journal of Radiation Oncology * Biology * Physics*, vol. 54, no. 1, pp. 215–28, 2002. DOI: 10.1016/S0360-3016(02)02938-3.

[40] P. Vaupel and A. Mayer, "Hypoxia in cancer: Significance and impact on clinical outcome", *Cancer and Metastasis Reviews*, vol. 26, pp. 225–39, 2007. DOI: 10.1007/s10555-007-9055-1.

[41] D. R. Grimes and M. Partridge, "A mechanistic investigation of the oxygen fixation hypothesis and oxygen enhancement ratio", *Biomedical physics & engineering express*, vol. 1, no. 4, p. 045 209, 2015. DOI: 10.1088/2057-1976/1/4/045209.

[42] B. G. Wouters and J. M. Brown, "Cells at intermediate oxygen levels can be more important than the "hypoxic fraction" in determining tumor response to fractionated radiotherapy", *Radiation Research*, vol. 147, no. 5, pp. 541–50, 1997. DOI: 10.2307/3579620.

[43] K. Sachs, P. Hahnfeld, and D. J. Brenner, "Review the link between low-LET dose-response relations and the underlying kinetics of damage production/repair/misrepair", *International Journal of Radiation Biology*, vol. 72, no. 4, pp. 351–74, 1997. DOI: 10.1080/095530097143149.

[44] J. F. Fowler, "The linear-quadratic formula and progress in fractionated radiotherapy", *The British Journal of Radiology*, vol. 62, no. 740, pp. 679–94, 1989. DOI: 10.1259/0007-1285-62-740-679.

[45] G. W. Barendsen, "Dose fractionation, dose rate and iso-effect relationships for normal tissue responses", *International Journal of Radiation Oncology * Biology * Physics*, vol. 8, no. 11, pp. 1981–97, 1982. DOI: 10.1016/0360-3016(82)90459-X.

[46] S. Webb and A. E. Nahum, "A model for calculating tumour control probability in radiotherapy including the effects of inhomogeneous distributions of dose and clonogenic cell density", *Physics in Medicine & Biology*, vol. 38, no. 6, pp. 653–66, 1993. DOI: 10.1088/0031-9155/38/6/001.

[47] S. Webb and A. E. Nahum, "A model for calculating tumour control probability in radiotherapy including the effects of inhomogeneous distributions of dose and clonogenic cell density", *Physics in Medicine & Biology*, vol. 38, no. 6, pp. 653–66, 1993. DOI: 10.1088/0031-9155/38/6/001.

[48] T. L. Whiteside, S. Demaria, M. E. Rodriguez-Ruiz, *et al.*, "Emerging opportunities and challenges in cancer immunotherapy", *Clinical Cancer Research*, vol. 22, no. 8, pp. 1845–55, 2016. DOI: 10.1158/1078-0432.CCR-16-0049.

[49] T. A. Waldmann, "Immunotherapy: Past, present and future", *Nature Medicine*, vol. 9, no. 3, pp. 269–77, 2003. DOI: 10.1038/nm0303-269.

[50] D. S. Chen and I. Mellman, "Oncology meets immunology: The cancer-immunity cycle", *Immunity*, vol. 39, no. 1, pp. 1–10, 2013. DOI: 10.1016/j.immuni.2013.07.012.

[51] I. Mellman, G. Coukos, and G. Dranoff, "Cancer immunotherapy comes of age", *Nature*, vol. 480, no. 7378, pp. 480–9, 2011. DOI: 10.1038/nature10673.

[52] E. J. Lipson and C. G. Drake, "Ipilimumab: An anti-CTLA-4 antibody for metastatic melanoma", *Clinical Cancer Research*, vol. 17, no. 22, pp. 6958–62, 2011. DOI: 10.1158/1078-0432.CCR-11-1595.

[53] K. Pang, Z. D. Shi, L. Y. Wei, *et al.*, "Research progress of therapeutic effects and drug resistance of immunotherapy based on PD-1/PD-L1 blockade", *Drug Resistance Updates*, vol. 66, p. 100 907, 2023. DOI: 10.1016/j.drup.2022.100907.

[54] S. C. Formenti and S. Demaria, "Systemic effects of local radiotherapy", *The Lancet Oncology*, vol. 10, no. 7, pp. 718–26, 2009. DOI: 10.1016/S1470-2045(09)70082-8.

[55] S. Demaria, B. Ng, M. L. Devitt, *et al.*, "Ionizing radiation inhibition of distant untreated tumors (abscopal effect) is immune mediated", *International Journal of Radiation Oncology * Biology * Physics*, vol. 58, no. 3, pp. 862–70, 2004. DOI: 10.1016/j.ijrobp.2003.09.012.

[56] L. L. S. C. Apetoh, S. Ladoire, G. Coukos, *et al.*, "Combining immunotherapy and anticancer agents: The right path to achieve cancer cure?", *Annals of Oncology*, vol. 26, no. 9, pp. 1813–23, 2015. DOI: 10.1093/annonc/mdv209.

[57] C. Tang, X. Wang, H. Soh, *et al.*, "Combining radiation and immunotherapy: A new systemic therapy for solid tumors?", *Cancer Immunology Research*, vol. 2, no. 9, pp. 831–8, 2014. DOI: 10.1158/2326-6066.CIR-14-0069.

[58] M. Grapin, C. Richard, E. Limagne, *et al.*, "Optimized fractionated radiotherapy with anti-PD-L1 and anti-TIGIT: A promising new combination", *Journal for Immunotherapy of Cancer*, vol. 7, no. 160, pp. 1–12, 2019. DOI: 10.1186/s40425-019-0634-9.

[59] M. Z. Dewan, A. E. Galloway, N. Kawashima, *et al.*, "Fractionated but not single-dose radiotherapy induces an immune-mediated abscopal effect when combined with anti-CTLA-4 antibody", *Clinical Cancer Research*, vol. 15, no. 17, pp. 5379–88, 2009. DOI: 10.1158/1078-0432.CCR-09-0265.

[60] R. A. Bekker, S. Kim, S. Pilon-Thomas, *et al.*, "Mathematical modeling of radiotherapy and its impact on tumor interactions with the immune system", *Neoplasia*, vol. 28, p. 100 796, 2022. DOI: 10.1016/j.neo.2022.100796.

[61] M. Durante, E. Bräuer-Krisch, and M. Hill, "Faster and safer? FLASH ultra-high dose rate in radiotherapy", *The British Journal of Radiology*, vol. 91, no. 1082, p. 20 170 628, 2017. DOI: 10.1259/bjr.20170628.

[62] V. Favaudon, R. Labarbe, and C. L. Limoli, "Model studies of the role of oxygen in the FLASH effect", *Medical Physics*, vol. 49, no. 3, pp. 2068–81, 2022. DOI: 10.1002/mp.15129.

[63] D. L. Dewey and J. W. Boag, "Modification of the oxygen effect when bacteria are given large pulses of radiation", *Nature*, vol. 183, no. 4673, pp. 1450–1, 1959. DOI: 10.1038/1831450a0.

[64] B. Lin, F. Gao, Y. Yang, *et al.*, "FLASH radiotherapy: History and future", *Frontiers in Oncology*, vol. 11, p. 1890, 2021. DOI: 10.3389/fonc.2021.644400.

[65] E. Bogaerts, E. Macaeva, S. Isebaert, *et al.*, "Potential molecular mechanisms behind the ultra-high dose rate "FLASH" effect", *International Journal of Molecular Sciences*, vol. 23, no. 20, p. 12 109, 2022. DOI: 10.3390/ijms232012109.

[66] V. Favaudon, L. Caplier, V. Monceau, *et al.*, "Ultrahigh dose-rate FLASH irradiation increases the differential response between normal and tumor tissue in mice", *Science Translational Medicine*, vol. 6, no. 245, 245ra93, 2014. DOI: 10.1126/scitranslmed.3008973.

[67] P. Montay-Gruel, K. Petersson, M. Jaccard, *et al.*, "Irradiation in a flash: Unique sparing of memory in mice after whole brain irradiation with dose rates above 100Gy/s", *Radiotherapy and Oncology*, vol. 124, no. 3, pp. 365–9, 2017. DOI: 10.1016/j.radonc.2017.05.003.

[68] P. Montay-Gruel, A. Bouchet, M. Jaccard, *et al.*, "X-rays can trigger the FLASH effect: Ultra-high dose-rate synchrotron light source prevents normal brain injury after whole brain irradiation in mice", *Radiotherapy and Oncology*, vol. 129, no. 3, pp. 582–8, 2018. DOI: 10.1016/j.radonc.2018.08.016.

[69] M. C. Vozenin, P. De Fornel, K. Petersson, *et al.*, "The advantage of FLASH radiotherapy confirmed in mini-pig and cat-cancer patients", *Clinical Cancer Research*, vol. 25, no. 1, pp. 35–42, 2019. DOI: 10.1158/1078-0432.CCR-17-3375.

[70] P. Montay-Gruel, M. M. Acharya, K. Petersson, *et al.*, "Long-term neurocognitive benefits of FLASH radiotherapy driven by reduced reactive oxygen species", *Proceedings of the National Academy of Sciences*, vol. 116, no. 22, pp. 10 943–51, 2019. DOI: 10.1073/pnas.1901777116.

[71] K. Levy, S. Natarajan, J. Wang, *et al.*, "Abdominal FLASH irradiation reduces radiation-induced gastrointestinal toxicity for the treatment of ovarian cancer in mice", *Scientific Reports*, vol. 10, no. 21600, pp. 1–14, 2020. DOI: 10.1038/s41598-020-78017-7.

[72] E. S. Diffenderfer, I. I. Verginadis, M. M. Kim, *et al.*, "Design, implementation, and in vivo validation of a novel proton FLASH radiation therapy system", *International Journal of Radiation Oncology * Biology * Physics*, vol. 106, no. 2, pp. 440–8, 2020. DOI: 10.1016/j.ijrobp.2019.10.049.

[73] E. Liljedahl, E. Konradsson, E. Gustafsson, *et al.*, "Long-term anti-tumor effects following both conventional radiotherapy and FLASH in fully immunocompetent animals with glioblastoma", *Scientific Reports*, vol. 12, no. 12285, pp. 1–12, 2022. DOI: 10.1038/s41598-022-16612-6.

[74] F. Gao, Y. Yang, H. Zhu, *et al.*, "First demonstration of the FLASH effect with ultrahigh dose rate high-energy X-rays", *Radiotherapy and Oncology*, vol. 166, pp. 44–50, 2022. DOI: 10.1016/j.radonc.2021.11.004.

[75] G. Pratx and D. S. Kapp, "A computational model of radiolytic oxygen depletion during FLASH irradiation and its effect on the oxygen enhancement ratio", *Physics in Medicine & Biology*, vol. 64, no. 18, p. 185 005, 2019. DOI: 10.1088/1361-6560/ab3769.

[76] G. Pratx and D. S. Kapp, "Ultra-high-dose-rate FLASH irradiation may spare hypoxic stem cell niches in normal tissues", *International Journal of Radiation Oncology * Biology * Physics*, vol. 105, no. 1, pp. 190–2, 2019. DOI: 10.1016/j.ijrobp.2019.05.030.

[77] K. Petersson, G. Adrian, K. Butterworth, *et al.*, "A quantitative analysis of the role of oxygen tension in FLASH radiation therapy", *International Journal of Radiation Oncology * Biology * Physics*, vol. 107, no. 3, pp. 539–47, 2020. DOI: 10.1016/j.ijrobp.2020.02.634.

[78] X. Cao, R. Zhang, T. V. Esipova, *et al.*, "Quantification of oxygen depletion during FLASH irradiation in vitro and in vivo", *International Journal of Radiation Oncology * Biology * Physics*, vol. 111, no. 1, pp. 240–8, 2021. DOI: 10.1016/j.ijrobp.2021.03.056.

[79] J. Y. Jin, A. Gu, W. Wang, *et al.*, "Ultra-high dose rate effect on circulating immune cells: A potential mechanism for FLASH effect?", *Radiotherapy and Oncology*, vol. 149, pp. 55–62, 2020. DOI: 10.1016/j.radonc.2020.04.054.

[80] D. R. Spitz, G. R. Buettner, M. S. Petronek, *et al.*, "An integrated physico-chemical approach for explaining the differential impact of FLASH versus conventional dose rate irradiation on cancer and normal tissue responses", *Radiotherapy and Oncology*, vol. 139, pp. 23–7, 2019. DOI: 10.1016/j.radonc.2019.03.028.

[81] R. Abolfath, A. Baikalov, S. Rahvar, *et al.*, "Differential tissue sparing of FLASH ultra high dose rates: An in-silico study", *arXiv:2210.03565*, 2022. DOI: 10.48550/arXiv.2210.03565.

[82] H. Song, Y. Kim, and W. Sung, "Modeling of the FLASH effect for ion beam radiation therapy", *Physica Medica*, vol. 108, p. 102 553, 2023. DOI: 10.1016/j.ejmp.2023.102553.

[83] R. Labarbe, L. Hotoiu, J. Barbier, *et al.*, "A physicochemical model of reaction kinetics supports peroxyl radical recombination as the main determinant of the FLASH effect", *Radiotherapy and Oncolgy*, vol. 153, pp. 303–10, 2020. DOI: 10.1016/j.radonc.2020.06.001.

[84] E. Taylor, R. P. Hill, and D. Létourneau, "Modeling the impact of spatial oxygen heterogeneity on radiolytic oxygen depletion during FLASH radiotherapy", *Physics in Medicine & Biology*, vol. 67, no. 11, p. 115 017, 2022. DOI: 10.1088/1361-6560/ac702c.

[85] D. D. Bainov and P. S. Simeonov, *Impulsive differential equations: Asymptotic properties of the solutions*. Singapore: World Scientific, 1995, ISBN: 9789810218232. DOI: 10.1142/2413.

[86] B. Randjelovic, L. V. Stefanovic, and B. M. Dankovic, "Numerical solution of impulsive differential equations", *Facta Universitatis. Series Mathematics and Informatics*, vol. 15, pp. 101–11, 2000.

[87] N. S. B. A. Hamzah, M. Mamat, J. Kavikumar, *et al.*, "Impulsive differential equations by using the Euler method", *Applied Mathematical Sciences*, vol. 4, no. 65, pp. 3219–32, 2010.

[88] I. Györi and G. Ladas, *Oscillation theory of delay differential equations: With applications*, 1st ed. Oxford: Clarendon Press, 1992, ISBN: 9780198535829. DOI: 10.1093/oso/9780198535829.001.0001.

[89] L. Euler, *Institutiones calculi integralis*. Saint Petersburg: Academia Imperialis Scientiarum, 1768, vol. 1.

[90] J. C. Butcher, *Numerical methods for ordinary differential equations*, 2nd ed. John Wiley & Sons, 2016, ISBN: 9780470723357. DOI: 10.1002/9781119121534.

[91] V. Wulf and N. J. Ford, "Insight into the qualitative behaviour of numerical solutions to some delay differential equations", *Proceedings of HERCMA*, pp. 629–36, 1998.

[92] P. Díaz-Botana, "Modelización de hipoxia crónica/aguda en tumores mediante la resolución de la ecuación de reacción-difusión y su efecto en tratamientos radioterápicos", M.S. thesis, Universidade de Santiago de Compostela, 2016.

[93] I. Espinoza, P. Peschke, and C. P. Karger, "A model to simulate the oxygen distribution in hypoxic tumors for different vascular architectures", *Medical Physics*, vol. 40, no. 8, p. 081 703, 2013. DOI: 10.1118/1.4812431.

[94] A. Daşu, I. Toma-Daşu, and M. Karlsson, "Theoretical simulation of tumour oxygenation and results from acute and chronic hypoxia", *Physics in Medicine & Biology*, vol. 48, no. 17, pp. 2829–42, 2003. DOI: 10.1088/0031-9155/48/17/307.

[95] P. Rodríguez-Barbeito, P. Díaz-Botana, A. Gago-Arias, *et al.*, "A model of indirect cell death caused by tumor vascular damage after high-dose radiotherapy", *Cancer Research*, vol. 79, no. 23, pp. 6044–53, 2019. DOI: 10.1158/0008-5472.CAN-19-0181.

[96] I. Espinoza, P. Peschke, and C. P. Karger, "A voxel-based multiscale model to simulate the radiation response of hypoxic tumors", *Medical Physics*, vol. 42, no. 1, pp. 90–102, 2015. DOI: 10.1118/1.4903298.

[97] M. A. Konerding, E. Fait, and A. Gaumann, "3D microvascular architecture of pre-cancerous lesions and invasive carcinomas of the colon", *British Journal of Cancer*, vol. 84, no. 10, pp. 1354–62, 2001. DOI: 10.1054/bjoc.2001.1809.

[98] V. Thomée, *Galerkin finite element methods for parabolic problems*. Springer Berlin, Heidelberg, 2006, ISBN: 9783540331216. DOI: 10.1007/3-540-33122-0.

[99] M. El Khatib, A. L. Van Slyke, A. Velalopoulou, *et al.*, "Ultrafast tracking of oxygen dynamics during proton FLASH", *International Journal of Radiation Oncology * Biology * Physics*, vol. 113, no. 3, pp. 624–34, 2022. DOI: 10.1016/j.ijrobp.2022.03.016.

[100] J. Jansen, E. Beyreuther, D. García-Calderón, *et al.*, "Changes in radical levels as a cause for the FLASH effect: Impact of beam structure parameters at ultra-high rates on oxygen depletion in water", *Radiotherapy and Oncolgy*, vol. 175, pp. 193–6, 2022. DOI: 10.1016/j.radonc.2022.08.024.

[101] A. L. Van Slyke, M. El Khatib, A. Velalopoulou, *et al.*, "Oxygen monitoring in model solutions and in vivo in mice during proton irradiation at conventional and FLASH dose rates", *Radiation Research*, vol. 198, no. 2, pp. 181–9, 2022. DOI: 10.1667/RADE-21-00232.1.

[102] J. L. Lions, *Quelques Méthodes de Résolution des Problèmes aux Limites Non-Linéaires*. Paris: Dunod, 1969, ISBN: 2-10-006847-4.

[103] H. T. Banks and M. L. Joyner, "AIC under the framework of least squares estimation", *Applied Mathematics Letters*, vol. 74, pp. 33–45, 2017. DOI: 10.1016/j.aml.2017.05.005.

[104] S. Kirkpatrick, C. D. Gelatt Jr, and M. P. Vecchi, "Optimization by simulated annealing", *Science*, vol. 220, no. 4598, pp. 671–80, 1983. DOI: 10.1126/science.220.4598.671.

[105] E. D. Kwon, C. G. Drake, H. I. Scher, *et al.*, "Ipilimumab versus placebo after radiotherapy in patients with metastatic castration-resistant prostate cancer that had progressed after docetaxel chemotherapy (CA184-043): A multicentre, randomised, double-blind, phase 3 trial", *The Lancet Oncology*, vol. 15, no. 7, pp. 700–12, 2014. DOI: 10.1016/S1470-2045(14)70189-5.

[106] E. B. Golden, S. Demaria, P. B. Schiff, *et al.*, "An abscopal response to radiation and ipilimumab in a patient with metastatic non-small cell lung cancer", *Cancer Immunology Research*, vol. 1, no. 6, pp. 365–72, 2013. DOI: 10.1158/2326-6066.CIR-13-0115.

[107] J. Gong, A. Chehrazi-Raffle, S. Reddi, *et al.*, "Development of PD-1 and PD-L1 inhibitors as a form of cancer immunotherapy: A comprehensive review of registration trials and future considerations", *Journal for ImmunoTherapy of Cancer*, vol. 6, no. 8, p. 8, 2018. DOI: 10.1186/s40425-018-0316-z.

[108] F. S. Hodi, S. J. O'Day, D. F. McDermott, *et al.*, "Improved survival with ipilimumab in patients with metastatic melanoma", *The New England Journal of Medicine*, vol. 363, no. 8, pp. 711–23, 2010. DOI: 10.1056/NEJMoa1003466.

[109] M. Crittenden, H. Kohrt, R. Levy, *et al.*, "Current clinical trials testing combinations of immunotherapy and radiation", *Seminars in Radiation Oncology*, vol. 25, no. 1, pp. 54–64, 2015. DOI: 10.1016/j.semradonc.2014.07.003.

[110] E. Mladenov, S. Magin, A. Soni, *et al.*, "DNA double-strand break repair as determinant of cellular radiosensitivity to killing and target in radiation therapy", *Frontiers in Oncology*, vol. 3, p. 113, 2013. DOI: 10.3389/fonc.2013.00113.

[111] L. de la Cruz-Merino, A. Illescas-Vacas, A. Grueso-López, *et al.*, "Radiation for awakening the dormant immune system, a promising challenge to be explored", *Frontiers in Immunology*, vol. 5, p. 102, 2014. DOI: 10.3389/fimmu.2014.00102.

[112] T. Walle, R. Martinez-Monge, A. Cerwenka, *et al.*, "Radiation effects on antitumor immune responses: Current perspectives and challenges", *Therapeutic Advances in Medical Oncology*, vol. 10, p. 1 758 834 017 742 575, 2018. DOI: 10.1177/1758834017742575.

[113] L. G. de Pillis, A. E. Radunskaya, and C. L. Wiseman, "A validated mathematical model of cell-mediated immune response to tumor growth", *Cancer Research*, vol. 65, no. 17, pp. 7950–8, 2005. DOI: 10.1158/0008-5472.CAN-05-0564.

[114] L. G. de Pillis, W. Gu, and A. E. Radunskaya, "Mixed immunotherapy and chemotherapy of tumors: Modeling, applications and biological interpretations", *Journal of Theoretical Biology*, vol. 238, no. 4, pp. 841–62, 2006. DOI: 10.1016/j.jtbi.2005.06.037.

[115] S. Chareyron and M. Alamir, "Mixed immunotherapy and chemotherapy of tumors: Feedback design and model updating schemes", *Journal of Theoretical Biology*, vol. 258, no. 3, pp. 444–54, 2009. DOI: 10.1016/j.jtbi.2008.07.002.

[116] L. Xiulan and A. Friedman, "Combination therapy of cancer with cancer vaccine and immune checkpoint inhibitors: A mathematical model", *PLoS ONE*, vol. 12, no. 5, e0178479, 2017. DOI: 10.1371/journal.pone.0178479.

[117] A. Radunskaya, R. Kim, and T. Woods II, "Mathematical modeling of tumor immune interactions: A closer look at the role of a PD-L1 inhibitor in cancer immunotherapy", *SPORA: A Journal of Biomathematics*, vol. 4, no. 1, pp. 25–41, 2018. DOI: 10.30707/SPORA4.1Radunskaya.

[118] M. A. Benchaib, A. Bouchnita, V. Volpert, *et al.*, "Mathematical modeling reveals that the administration of EGF can promote the elimination of lymph node metastases by PD-1/PD-L1 blockade", *Frontiers in Bioengineering and Biotechnology*, vol. 7, p. 104, 2019. DOI: 10.3389/fbioe.2019.00104.

[119] R. Eftimie, J. L. Bramson, and D. J. D. Earn, "Interactions between the immune system and cancer: A brief review of non-spatial mathematical models", *Bulletin of Mathematical Biology*, vol. 73, no. 1, pp. 2–32, 2011. DOI: 10.1007/s11538-010-9526-3.

[120] R. Serre, F. Barlesi, X. Muracciole, *et al.*, "Immunologically effective dose: A practical model for immuno-radiotherapy", *Oncotarget*, vol. 9, no. 61, pp. 31 812–9, 2018. DOI: 10.18632/oncotarget.25746.

[121] Y. Kosinsky, S. J. Dovedi, K. Peskov, *et al.*, "Radiation and PD-(L)1 treatment combinations: Immune response and dose optimization via a predictive systems model", *Journal for ImmunoTherapy of Cancer*, vol. 6, no. 17, p. 17, 2018. DOI: 10.1186/s40425-018-0327-9.

[122] W. Sung, C. Grassberger, A. L. McNamara, *et al.*, "A tumor-immune interaction model for hepatocellular carcinoma based on measured lymphocyte counts in patients undergoing radiotherapy", *Radiotherapy and Oncology*, vol. 151, pp. 73–81, 2020. DOI: 10.1016/j.radonc.2020.07.025.

[123] J. D. Butner, D. Elganainy, C. X. Wang, *et al.*, "Mathematical prediction of clinical outcomes in advanced cancer patients treated with checkpoint inhibitor immunotherapy", *Science Advances*, vol. 6, no. 18, eaay6298, 2020. DOI: 10.1126/sciadv.aay6298.

[124] S. Fedotov and A. Iomin, "Probabilistic approach to a proliferation and migration dichotomy in tumor cell invasion", *Physical Review E*, vol. 77, p. 031 911, 2008. DOI: 10.1103/PhysRevE.77.031911.

[125] W. Dörr, "Three A's of repopulation during fractionated irradiation of squamous epithelia: Asymmetry loss, Acceleration of stem-cell divisions and Abortive divisions", *International Journal of Radiation Biology*, vol. 72, no. 6, pp. 635–43, 1997. DOI: 10.1080/095530097142780.

[126] M. J. Selby, J. J. Engelhardt, M. Quigley, *et al.*, "Anti-CTLA-4 antibodies of IgG2a isotype enhance antitumor activity through reduction of intratumoral regulatory T cells", *Cancer Immunology Research*, vol. 1, no. 1, pp. 32–42, 2013. DOI: 10.1158/2326-6066.CIR-13-0013.

[127] R. Deng, D. Bumbaca, C. V. Pastuskovas, *et al.*, "Preclinical pharmacokinetics, pharmacodynamics, tissue distribution, and tumor penetration of anti-PD-L1 monoclonal antibody, an immune checkpoint inhibitor", *mAbs*, vol. 8, no. 3, pp. 593–603, 2016. DOI: 10.1080/19420862.2015.1136043.

[128] I. González-Crespo, A. Gómez-Caamaño, Ó. López Pouso, *et al.*, *Replication data for "A biomathematical model of tumor response to radioimmunotherapy with $\alpha PDL1$ and $\alpha CTLA4$"*, 2022. DOI: 10.7910/DVN/QE2TKH.

[129] R. Kuse, S. Schuster, H. Schübbe, *et al.*, "Blood lymphocyte volumes and diameters in patients with chronic lymphocytic leukemia and normal controls", *Blut*, vol. 50, pp. 243–8, 1985. DOI: 10.1007/BF00320301.

[130] L. Lonati, S. Barbieri, I. Guardamagna, *et al.*, "Radiation-induced cell cycle perturbations: A computational tool validated with flow-cytometry data", *Scientific reports*, vol. 11, no. 1, p. 925, 2021. DOI: 10.1038/s41598-020-79934-3.

[131] P. M. Reed, A. Hadjimichael, K. Malek, *et al.*, *Addressing uncertainty in multisector dynamics research*. Zenodo, 2022. DOI: 10.5281/zenodo.6110623.

[132] L. G. Hanin, "Iterated birth and death process as a model of radiation cell survival", *Mathematical Biosciences*, vol. 169, no. 1, pp. 89–107, 2001. DOI: 10.1016/S0025-5564(00)00054-7.

[133] A. Arina, M. Beckett, C. Fernandez, *et al.*, "Tumor-reprogrammed resident T cells resist radiation to control tumors", *Nature Communications*, vol. 10, no. 1, p. 3959, 2019. DOI: 10.1038/s41467-019-11906-2.

[134] C. M. van Leeuwen, A. L. Oei, J. Crezee, *et al.*, "The alfa and beta of tumours: A review of parameters of the linear-quadratic model, derived from clinical radiotherapy studies", *Radiation Oncology*, vol. 13, no. 1, p. 96, 2018. DOI: 10.1186/s13014-018-1040-z.

[135] J. Bourhis, W. J. Sozzi, P. Gonçalves Jorge, *et al.*, "Treatment of a first patient with FLASH-radiotherapy", *Radiotherapy and Oncology*, vol. 139, pp. 18–22, 2019. DOI: 10.1016/j.radonc.2019.06.019.

[136] J. Bourhis, P. Montay-Gruel, P. Gonçalves Jorge, *et al.*, "Clinical translation of FLASH radiotherapy: Why and how?", *Radiotherapy and Oncology*, vol. 139, pp. 11–17, 2019. DOI: 10.1016/j.radonc.2019.04.008.

[137] M. C. Vozenin, J. Bourhis, and M. Durante, "Towards clinical translation of FLASH radiotherapy", *Nature Reviews Clinical Oncology*, vol. 19, no. 12, pp. 791–803, 2022. DOI: 10.1038/s41571-022-00697-z.

[138] H. Liew, S. Mein, T. Tessonnier, *et al.*, "Do we preserve tumor control probability (TCP) in FLASH radiotherapy? A model-based analysis", *International Journal of Molecular Sciences*, vol. 24, no. 6, p. 5118, 2023. DOI: 10.3390/ijms24065118.

[139] V. G. Vaidya and F. J. Alejandro Jr, "Evaluation of some mathematical models for tumor growth", *International Journal of Bio-Medical Computing*, vol. 13, no. 1, pp. 19–35, 1982. DOI: 10.1016/0020-7101(82)90048-4.

[140] H. Zhu, D. Xie, Y. Wang, *et al.*, "Comparison of intratumor and local immune response between MV X-ray FLASH and conventional radiotherapies", *Clinical and Translational Radiation Oncology*, vol. 38, pp. 138–46, 2023. DOI: 10.1016/j.ctro.2022.11.005.

[141] C. S. Reichardt, *Quasi-experimentation: A guide to design and analysis*. New York: Guilford Publications, 2019, ISBN: 9781462540204.

[142] G. Adrian, E. Konradsson, M. Lempart, *et al.*, "The FLASH effect depends on oxygen concentration", *The British Journal of Radiology*, vol. 93, no. 1106, p. 20 190 702, 2020. DOI: 10.1259/bjr.20190702.

[143] H. Zhu, J. Li, X. Deng, *et al.*, "Modeling of cellular response after FLASH irradiation: A quantitative analysis based on the radiolytic oxygen depletion hypothesis", *Physics in Medicine & Biology*, vol. 66, no. 18, p. 185 009, 2021. DOI: 10.1088/1361-6560/ac226d.

[144] B. S. Sørensen, M. K. Sitarz, C. Ankjærgaard, *et al.*, "Pencil beam scanning proton FLASH maintains tumor control while normal tissue damage is reduced in a mouse model", *Radiotherapy and Oncology*, vol. 175, pp. 178–84, 2022. DOI: 10.1016/j.radonc.2022.05.014.

[145] J. Jeong, K. I. Shoghi, and J. O. Deasy, "Modelling the interplay between hypoxia and proliferation in radiotherapy tumour response", *Physics in Medicine & Biology*, vol. 58, no. 14, pp. 4897–919, 2013. DOI: 10.1088/0031-9155/58/14/4897.

[146] S. Shukla, T. Saha, N. Rama, *et al.*, "Ultra-high dose-rate proton FLASH improves tumor control", *Radiotherapy and Oncology*, vol. 186, p. 109 741, 2023. DOI: j.radonc.2023.109741.

[147] Y. Takeuchi, N. Adachi, and H. Tokumaru, "The stability of generalized Volterra equations", *Journal of Mathematical Analysis and Applications*, vol. 62, no. 3, pp. 453–73, 1978. DOI: 10.1016/0022-247X(78)90139-7.

[148] Y. Takeuchi and N. Adachi, "Stable equilibrium of systems of generalized Volterra type", *Journal of Mathematical Analysis and Applications*, vol. 88, no. 1, pp. 157–69, 1982. DOI: 10.1016/0022-247X(82)90183-4.

List of Figures

List of Tables

List of Listings

Acronyms

αCTLA4 anti-CTLA-4 23–25, 50–52, 56–61, 63–65, 67–73, 96, 97, 113–116, 118, 119, 122, 137, 142–146, *see* CTLA-4

αPD(L)1 anti-Programmed Death-(Ligand) 1 24, 25, 50–52, 56–58, 96, 97, 114, *see* PD-(L)1

αPD1 anti-PD-1 24, *see* PD-1

αPDL1 anti-PD-L1 24, 51, 57, 60, 61, 65, 66, 72, 73, 96, 114, 115, 122, 142, *see* PD-L1

AIC Akaike Information Criterion 44, 45, 67

ANCOVA ANalysis of COVAriance 81, 88

APC Antigen Presenting Cell 22, 51, 52, 55, 114

BED Biologically Effective Dose 19, 20, 70, 71, 91, 113, 116, 122

BSA Bovine Serum Albumin 79, 80, 83, 116, 121

CAR Chimeric Antigen Receptor 14

CD Cluster of Differentiation 22, 23, 113

CHUS Complexo Hospitalario Universitario de Santiago 1, 2

conv-RT conventional RT 26, 40–42, 76–83, 85–93, 97, 98, 114, 117, 119, 122, 147, 150, *see* RT

CTLA-4 Cytotoxic T-Lymphocyte Antigen 4 21–23, 50–52, 55, 113

DC Dendritic Cell 22–24, 113

DDE Delay Differential Equation 30–33, 51, 74, 96, 137

FEM Finite Element Method 34, 36, 38, 39, 42, 79, 118, 131, 132

FLASH-RT FLASH RT 14, 21, 26, 27, 30, 33, 34, 40–42, 76–94, 96–98, 114, 116, 117, 119, 122, 133, 134, 137, 139, 147, 150, *see* RT

HIF Hypoxia Inducible Factor 17

ICI Immune Checkpoint Inhibitor 14, 22, 24, 25, 50, 51, 96

IDE Impulsive Differential Equation 30, 33, 51, 53, 79, 96, 137

IDIS Instituto de Investigación Sanitaria de Santiago 1, 2

IGRT Image-Guided RT 13, *see* RT

IMRT Intensity-Modulated RT 13, *see* RT

IT ImmunoTherapy 21–25, 27, 50, 51, 56, 57, 59–61, 64–70, 73, 74, 96, 97, 113–116

IVP Initial Value Problem 31, 32, 78, 133–135

LQ Linear-Quadratic 14–21, 25, 27, 30, 52–54, 58, 61, 63, 66–68, 78, 82, 85, 92, 96, 113, 115, 118, 119, 123, 144–146

LQ$_{\text{mod}}$ modified LQ 53, 54, 58, 63, 64, 67, 115, 122, 142, *see* LQ

LQL Linear-Quadratic-Linear 15, 18, 19, 30, 53, 54, 58, 64, 65, 67, 73, 113, 115, 123, 143

MDSC Myeloid-Derived Suppressor Cell 50

MHC Major Histocompatibility Complex 22, 23, 113

NTCP Normal Tissue Complication Probability 14

ODE Ordinary Differential Equation 30, 32, 50, 51, 79, 96, 137

OER Oxygen Enhancement Ratio 17, 18, 26, 78, 86, 92–94

PD-(L)1 Programmed Death-(Ligand) 1 50, 52

PD-1 Programmed Death 1 21, 22, 24, 50, 51, 114

PD-L1 Programmed Death-Ligand 1 21, 22, 24, 50, 51, 114

PDE Partial Differential Equation 30, 34, 42–44, 77, 96, 97, 125

RIT RadioImmunoTherapy 14, 21, 24, 25, 27, 30, 50–52, 56, 58–60, 62, 63, 66, 68, 70, 72–74, 96, 97, 116, 118, 119, 133, 137, 145, 146

ROD Radiolytic Oxygen Depletion 26, 33, 34, 40, 42, 76–78, 85, 86, 90, 92–94, 97, 98

RT RadioTherapy 12–16, 20–22, 24–27, 30, 33, 45, 50–53, 57, 59–61, 63–74, 91, 96, 97, 114–116, 121

SA Simulated Annealing 44–47, 61, 81, 114

SBRT Stereotactic Body RT 13, 14, *see* RT

SF Surviving Fraction 14–19, 53, 54, 76–79, 82, 85–87, 90, 92–94, 97, 113, 117

SFRT Spatially Fractionated RT 14, *see* RT

SRS Stereotactic Radiation Surgery 13, 14

TCP Tumor Control Probability 14, 20, 21, 51, 63, 69–72, 74, 76, 77, 82, 83, 90–94, 96–98, 116, 117, 119, 122, 150

TCR T-Cell Receptor 22, 23, 113

TME Tumor MicroEnvironment 17, 20, 22, 24, 30, 50

Treg regulatory T-cell 50, 52

UHDR Ultra-High Dose Rate 14, 26, 40, 41, 76, 97

USC Universidade de Santiago de Compostela 1, 2

VF Vascular Fraction 34, 35, 42, 82, 114, 119, 148

VMAT Volumetric Modulated Arc Therapy 13

WSSD Weighted Sum of Squared Differences 44, 61, 62, 81

Appendix A

Mesh convergence study to apply the FEM

Meshing to apply the FEM requires finding a good compromise between mesh quality and the resulting computational cost of solving the associated problem. A good-quality mesh is defined by uniform-shaped elements and smooth size transitions between consecutive elements. Low-quality meshes usually require fewer elements and decrease the execution time but may introduce errors and instability in the solution. Therefore, this appendix presents a mesh convergence study to solve Problem 2.4 applied to the domain shown in Figure 2.1.

The FEM was run with different mesh sizes and the solutions were compared to a reference solution for the finest computed mesh ($\sim 60\,000$ nodes) by calculating the absolute error in the mean partial pressure over the whole domain, $\overline{p}$. The results are shown in the left panel of Figure A.1. Moreover, the execution time of running the code in Listing 2.5 is shown in the right panel.

In this thesis, meshes with approximately 10 000 nodes were considered well-balanced in terms of quality and computational cost.

Finally, the MATLAB function `meshQuality` was employed to evaluate the shape quality of the elements in a representative mesh with 10 496 nodes and 19 621 elements, illustrated in Figure A.2. This function assigns a number within the range 0–1 to each element, where 1 corresponds to the optimal shape, being an equilateral triangle in the case of two-dimensional triangular meshes. The quality of an element, Q, is obtained as:

$$Q = \frac{4\sqrt{3}a}{h_1^2 + h_2^2 + h_3^2},$$

where a is the area of the triangle, and $h_i,\ i = 1, 2, 3$, are the three edges.

The mean quality of the mesh shown in Figure A.2 is $\overline{Q} = 0.98$ with a typical deviation of 0.03. Only eight elements out of the total (0.04%) present $Q < 0.8$ and one element shows $Q < 0.5$.

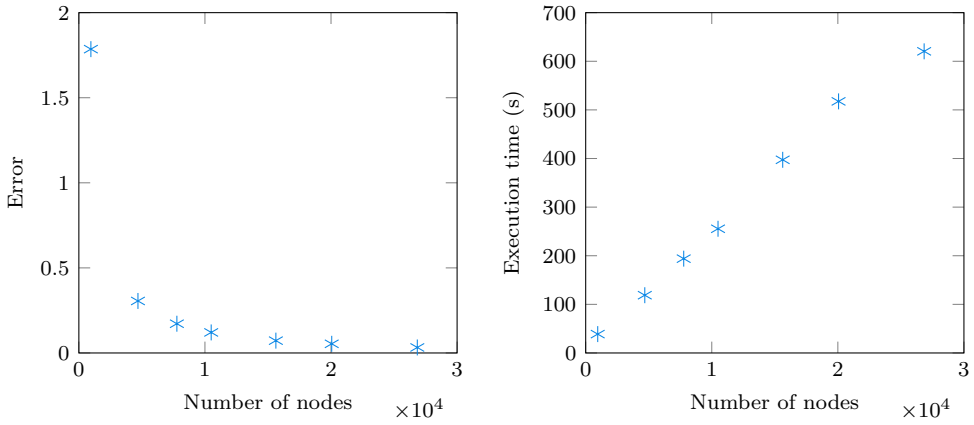

Figure A.1: Convergence study of the mesh to solve Problem 2.4. The left panel presents absolute error measurements for different numbers of nodes compared to the finest computed mesh ($\sim 60\,000$ nodes). The right panel shows the respective execution times obtained from running the code in Listing 2.5.

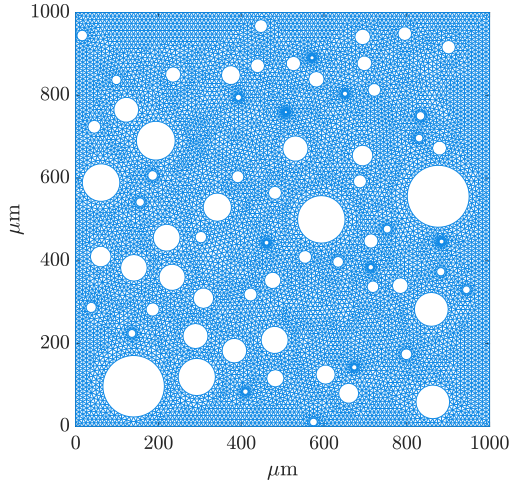

Figure A.2: Example of a mesh to apply the FEM to solve the oxygenation problem on the domain shown in Figure 2.1.

Appendix B

Formal analysis of the response models

This appendix presents some aspects of the formal analysis of the response models to RIT and FLASH-RT, respectively given in Sections 3.2.6 and 4.4.

B.1 RIT model

Using the notation from Section 2.1, the IVP associated to the RIT response model given in Section 3.2.6 can be rewritten as:

$$\begin{cases} \dfrac{d\boldsymbol{x}(t)}{dt} = \boldsymbol{f}(\boldsymbol{x}(t), \boldsymbol{x}(t-\tau_{\mathrm{A}}), \boldsymbol{x}(t-\tau_{\mathrm{T}})), & \forall t \neq t_i, \\ \Delta\boldsymbol{x}(t_i) = \boldsymbol{I}_i(\boldsymbol{x}(t_i)), & \forall t = t_i, \\ \boldsymbol{x}(t) = \boldsymbol{x}_0, & \forall t \in [-\max\{\tau_{\mathrm{A}}, \tau_{\mathrm{T}}\}, 0], \end{cases} \tag{B.1}$$

being $x_1(t) = C(t)$, $x_2(t) = C_{\mathrm{d}}(t)$, $x_3(t) = T_{\mathrm{a}}(t)$, $x_4(t) = \hat{T}_{\mathrm{a}}(t)$, $x_5(t) = \hat{T}_{\mathrm{b}}(t)$, $x_6(t) = \hat{T}(t)$, $x_7(t) = \hat{A}(t)$, $x_8(t) = c_4(t)$, and $x_9(t) = p_1(t)$.

As the initial condition is given by a continuous function and $\boldsymbol{f}$ is of class $\mathcal{C}^\infty$ in $\{\boldsymbol{x} \in \mathbb{R}^9 : x_1 > 0, x_2 > 0\} \times \mathbb{R}^9 \times \mathbb{R}^9$ (and particularly of class $\mathcal{C}^1$, thus $\boldsymbol{f}$ is locally Lipschitz continuous), then Theorems 1 and 2 prove that there exist a local solution to the above IVP.

B.2 FLASH-RT model

Using the notation from Section 2.1, the IVP associated to the FLASH-RT response model given in Section 4.4 can be rewritten as:

$$\begin{cases} \dfrac{d\boldsymbol{x}(t)}{dt} = \boldsymbol{f}(\boldsymbol{x}(t)), & \forall t \neq t_i, \\ \Delta\boldsymbol{x}(t_i) = \boldsymbol{I}_i(\boldsymbol{x}(t_i)), & \forall t = t_i, \\ \boldsymbol{x}(0) = \boldsymbol{x}_0, \end{cases} \tag{B.2}$$

being $x_1(t) = C(t)$, $x_2(t) = C_{\mathrm{d}}(t)$, and:

$$\boldsymbol{x} = \begin{pmatrix} x_1 \\ x_2 \end{pmatrix}, \boldsymbol{f} = \begin{pmatrix} \lambda\left(1 - \dfrac{x_1 + x_2}{K}\right) x_1 \\ -\lambda\dfrac{x_1 + x_2}{K} x_2 - \phi x_2 \end{pmatrix}, \Delta\boldsymbol{x} = \begin{pmatrix} (SF-1)x_1 \\ (1-SF)x_1 \end{pmatrix}, \text{ and } \boldsymbol{x}(0) = \begin{pmatrix} x_{0,1} \\ x_{0,2} \end{pmatrix}.$$

The function $\boldsymbol{f}$ is at least of class $\mathcal{C}^1$ in $\mathbb{R}^2$, thus local Lipschitz continuity is guaranteed by the mean value theorem. Subsequently, Theorem 1 proves that there exist $b > 0$ (for $t_0 = 0$) and a unique local solution $\boldsymbol{x} : (0, b) \to \mathbb{R}^2$ to the above IVP.

Notice that, as mentioned in Section 4.4, for this study the initial condition $x_{0,2}$ was set to 0. Thus, in the absence of impulses, $x_2 \equiv 0$, and the IVP is transformed into the following:

$$\begin{cases} \dfrac{dx(t)}{dt} = \lambda\left(1 - \dfrac{x_1(t)}{K}\right) x_1(t), & \forall t > 0 \\ x_1(0) = x_{0,1}. \end{cases} \tag{B.3}$$

The analytical global solution to the above IVP is:

- If $x_{0,1} = 0$, then $x_1 \equiv 0$.
- If $x_{0,1} = K$, then $x_1 \equiv K$.
- If $x_{0,1} \in (0, K)$, then $x_1 = \dfrac{x_{0,1}K}{x_{0,1} + (K - x_{0,1})\exp(-\lambda t)}$.

In the particular case that there is a single impulse at $t = 0$, which is the case of study in Section 4.6, the IVP (B.2) is equivalent to the following:

$$\begin{cases} \dfrac{dx_1(t)}{dt} = \lambda\left(1 - \dfrac{x_1 + x_2}{K}\right) x_1, & \forall t > 0 \\ \dfrac{dx_2(t)}{dt} = -\lambda\dfrac{x_1 + x_2}{K} x_2 - \phi x_2, & \forall t > 0 \\ x_1(0) = SF x_{0,1}, \\ x_2(0) = (1 - SF)x_{0,1}, \end{cases} \tag{B.4}$$

where $SF \in (0, 1]$, thus $0 \leq x_1(0) \leq x_{0,1}$ and $0 \leq x_2(0) < x_{0,1}$. The critical points of the above system have been studied and the respective phase portrait is shown in Figure B.1, having that:

- $(0, 0)$ is a saddle.
- $(K, 0)$ is a sink.
- $\left(0, -\phi\dfrac{K}{\lambda}\right)$ is a source.

In the context of this thesis, only positive solutions are biologically reasonable. Besides, if $x_1 = 0$ and $x_2 = 0$ for any t, it would mean that the tumor does not exist, and the presented model was not designed to describe tumor total remission. Thus, $(K, 0)$ is the only critical point of interest. In view of the phase portrait, if the initial condition is in the first quadrant, the solution of the system tends to the sink $(K, 0)$, as expected. Moreover, the critical point being a sink guarantees that the solutions to the system are global, i.e., they are defined in the interval $(0, \infty)$, assuming that the initial condition is near enough to $(K, 0)$.

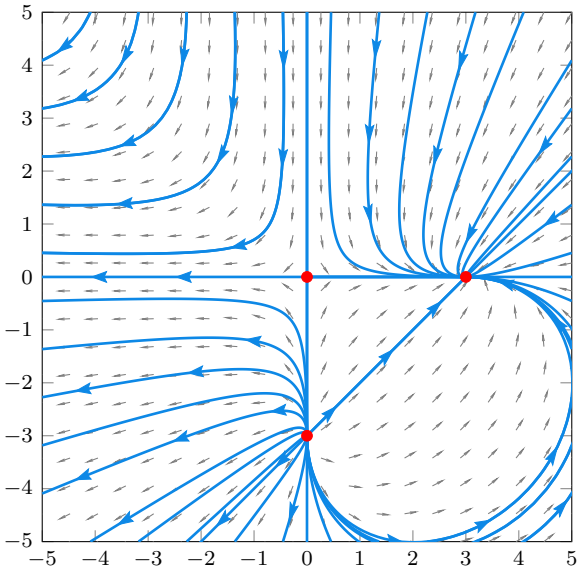

Figure B.1: Phase portrait of the system (B.4) using $\lambda = 1$, $\phi = 1$, and $K = 3$. The critical points are shown in red.

The IVP (B.4) is a particular case of a generalized Volterra system, the dynamical behavior of which has been studied in the literature [147, 148].

Appendix C

Forward Euler algorithm stability

Given the complexity of the presented models, which involve ODEs, DDEs and IDEs, a simple forward Euler algorithm, described in Section 2.1.3, was implemented to obtain numerical solutions. This method may have stability problems for stiff differential equations, but in general, it is not possible to know *a priori* whether a given equation presents stiffness [90].

This appendix presents convergence studies for the numerical solution of both the RIT and FLASH-RT response models.

C.1 RIT model

Figure C.1 shows the evolution of tumor volumes (obtained with best-fitting parameters reported in Table D.4) in the control group (left), and RIT group with 8 Gy$\times$3 and αCTLA4 at days 2, 5 and 8 (right), for different time steps, ranging from $\Delta t = 1$ days to $\Delta t = 0.001$ days. The solution for the lowest time step is considered as a reference and the best approximation to the exact solution.

Figure C.2 presents the absolute error made when calculating the volume with each time step against the reference solution at day 10. The error shows a linear dependence on the discretization time step, as expected for the Euler method in well-conditioned problems. $\Delta t = 0.05$ days was selected as a good trade-off between reducing time execution and obtaining accurate approximations of the exact solution (especially when considering the uncertainties of the experimental data).

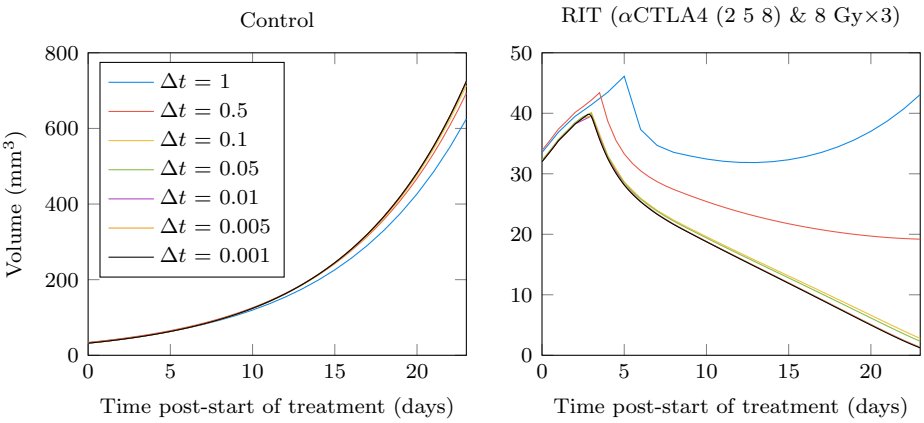

Figure C.1: Tumor volume evolution with different time steps, Δt (days), using the parameters summarized in Table D.4. In the left panel, curves for $\Delta t \in \{0.05, 0.01, 0.005, 0.001\}$ overlap, while in the right panel, curves for $\Delta t \in \{0.01, 0.005, 0.001\}$ overlap.

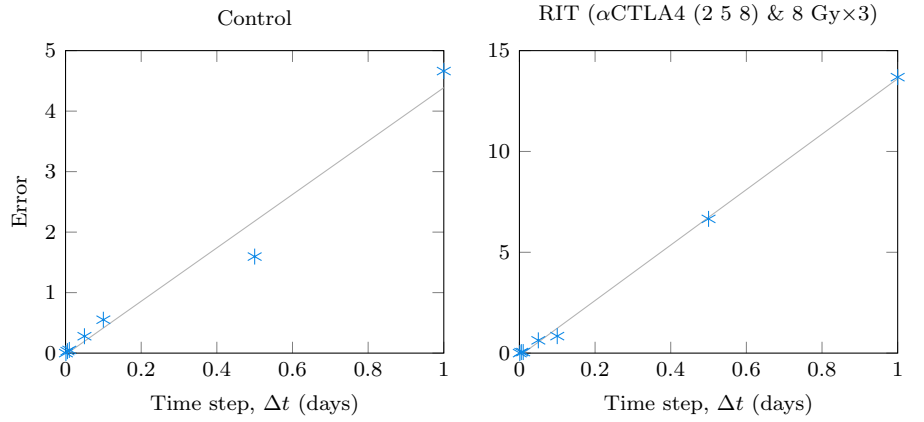

Figure C.2: Absolute error when calculating the volume (at day 10 post-start of treatment) with different time steps (asterisks), and linear fits of the obtained values (solid line). The solution with $\Delta t = 0.001$ days served as a reference to calculate the global error.

C.2 FLASH-RT model

Figure C.3 shows the evolution of tumor volumes (obtained with best-fitting parameters reported in the first column of Table E.1) in the control group (left), and FLASH-RT group (12 Gy × 1) (right) for different time steps, ranging from $\Delta t = 1$ days to $\Delta t = 0.001$ days. The solution for the lowest time step is considered as a reference and the best approximation to the exact solution.

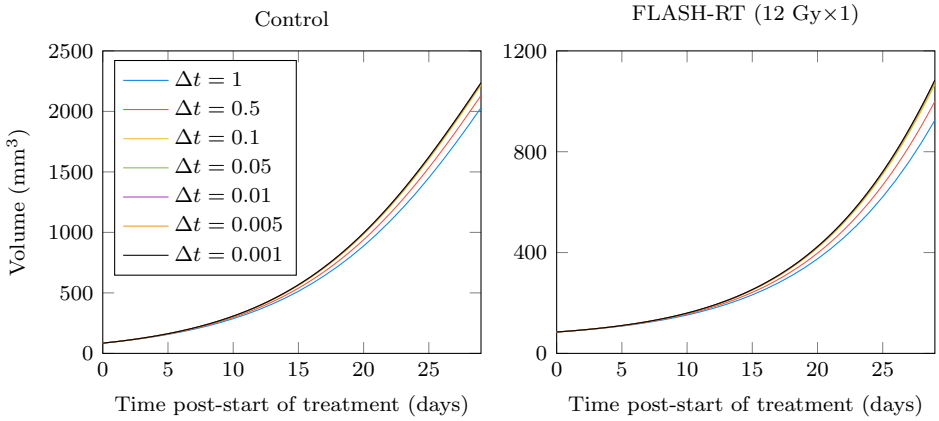

Figure C.3: Tumor volume evolution with different time steps, Δt (days), using the parameters summarized in Table E.1). In both panels, curves for $\Delta t \in \{0.05, 0.01, 0.005, 0.001\}$ overlap.

Figure C.4 presents the absolute error made when calculating the volume with each time step against the reference solution at day 10. The error shows a linear dependence on the discretization time step, as expected for the Euler method in well-conditioned problems. $\Delta t = 0.1$ days was selected as a good trade-off between reducing time execution and obtaining accurate approximations of the exact solution (especially when considering the uncertainties of the experimental data).

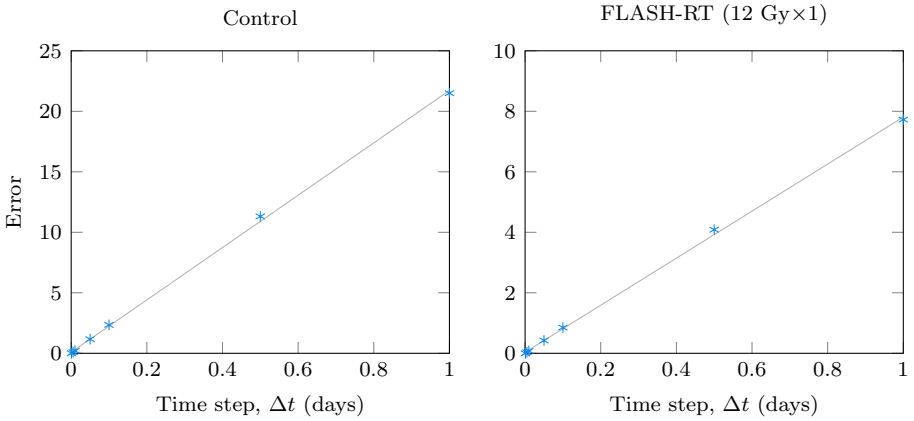

Figure C.4: Absolute error when calculating the volume (at day 10 post-start of treatment) with different time steps (asterisks), and linear fits of the obtained values (solid line). The solution with $\Delta t = 0.001$ days served as a reference to calculate the global error.

Appendix D

RIT tables and figures

Parameter	Description	Bound
α_{C}	Linear parameter for tumor cells (Gy^{-1})	$[0.0200, 0.3500]$
β_{C}	Quadratic parameter for tumor cells (Gy^{-2})	$[\alpha_{\mathrm{C}}/20, \alpha_{\mathrm{C}}/2]$
c	Modulation factor of β_{C} ($\mathrm{Gy}^{-1/2}$)	$[-0.2236, \infty)$
ϕ	Elimination rate of doomed tumor cells (days^{-1})	$[0.0300, 0.7000]$
q	Immune-mediated tumor cell death parameter	$[0, 1]$
τ_{A}	Antigen liberation to T-cell activation delay (days)	$[0, 5]$
σ	Natural elimination rate of antigens (days^{-1})	$[0.0300, 0.7000]$
a	Activation rate of T-cells (days^{-1})	$[0, 3 \times 10^{-7}]$
τ_{T}	Activated T-cell's time to reach the tumor (days)	$[0, 5]$
ι	Immune-mediated T-cells death rate (days^{-1})	$[0, 10^{-7}]$
η	Rate of natural elimination of T-cells (days^{-1})	$[0.0300, 0.7000]$
h	Rate of production of *blank* T-cells (days^{-1})	$[0.0500\hat{T}_0, \hat{T}_0]$

Table D.1: Parameter restrictions used for model fitting. Parameters not included in the table were constrained to be positive.

Parameter	Description	Best-fitting value
C_0	*Initial number of tumor cells	100
T_0	**Initial pool of *blank* T-cells	1.3188×10^6
λ_1	Proliferation rate of tumor cells (days^{-1})	0.1367 [Dewan] 0.1217 [Deng]
λ_2	Saturation of proliferation	0 [Dewan] 4.5320×10^{-10} [Deng]
α_C	Linear parameter for tumor cells (Gy^{-1})	0.0200 [Dewan] 0.0299 [Deng]
β_C	Quadratic parameter for tumor cells (Gy^{-2})	0.0068 [Dewan] 0.0030 [Deng*]
c	Modulation factor of β_C (Gy$^{-1/2}$)	−0.2001 [Dewan] 0 [Deng*]
ϕ	**Elimination rate of doomed tumor cells (days^{-1})	0.0484
τ_{d1}	*Mitotic delay (plateau duration time) (days)	1
τ_{d2}	*Mitotic delay (end) (days)	1.5000
p	**Immune-mediated tumor cell death rate (days^{-1})	24.4339
q	**Immune-mediated tumor cell death parameter	0.6925
s	**Slope of the immune-mediated tumor death curve	7.5013
i_{p_1}	Dose of αPDL1 per administration time	19.0387 (if αPDL1) 0 (otherwise)
μ	*Elimination rate of αPDL1 (days^{-1})	0.5000
ρ	**Rate of natural production of antigens (days^{-1})	1.0222×10^{-19}
ψ	**Release rate of antigens	267.2069
τ_A	**Antigen liberation to T-cell activation delay (days)	0.9894
σ	**Natural elimination rate of antigens (days^{-1})	0.0300
a	**Activation rate of T-cells (days^{-1})	8.8379×10^{-8}
r	*Activation/inactivation ratio	5
i_{c_4}	Dose of αCTLA4 per administration time	5.0564 (if αCTLA4) 0 (otherwise)
ν	*Elimination rate of αCTLA4 (days^{-1})	0.1000
τ_T	**Activated T-cell's time to reach the tumor (days)	0.4561
α_T	*Linear parameter for T-cells (Gy^{-1})	0.1000
β_T	*Quadratic parameter for T-cells (Gy^{-2})	0.0100
ι	**Immune-mediated T-cells death rate (days^{-1})	1.9847×10^{-8}
η	**Rate of natural elimination of T-cells (days^{-1})	0.0328
h	**Rate of production of *blank* T-cells (days^{-1})	1.7391×10^5
V_C	*Volume of tumor cells (mm^3)	10^{-6}
V_T	*Volume of T-cells (mm^3)	2×10^{-7}

Table D.2: Best-fitting parameters of the model to experimental data reported by Dewan *et al.* [59] and Deng *et al.* [18]. The LQ_{mod} model, given by equation (3.2), was used to account for tumor cell radiosensitivity. The symbol * indicates that the parameter value was fixed and not included in the optimization; while ** indicates that the parameter was optimized, but the same value was used for αCTLA4 and αPDL1 fittings. Initial numbers/concentrations of variables not indicated in the table (C_d, $\hat{A}$, T_a, $\hat{T}_a$, $\hat{T}_b$, c_4, p_1) were set to zero. The parameter r is defined as $r = 1 + b/a$ [34].

Parameter	Description	Best-fitting value
C_0	*Initial number of tumor cells	100
T_0	Initial pool of *blank* T-cells	1.8784×10^{6}
λ_1	Proliferation rate of tumor cells (days^{-1})	0.1356
λ_2	Saturation of proliferation	9.1172×10^{-118}
α_{C}	Linear parameter for tumor cells (Gy^{-1})	0.0442
β_{C}	Quadratic parameter for tumor cells (Gy^{-2})	0.0167
γ	Modulation factor of β_{C} (Gy^{-1})	8.4298
ϕ	Elimination rate of doomed tumor cells (days^{-1})	0.0312
$\tau_{\mathrm{d}1}$	*Mitotic delay (start) (days)	1
$\tau_{\mathrm{d}2}$	*Mitotic delay (end) (days)	1.5000
p	Immune-mediated tumor cell death rate (days^{-1})	23.3045
q	Immune-mediated tumor cell death parameter	0.7212
s	Slope of the immune-mediated tumor death curve	8.8282
ρ	Rate of natural production of antigens (days^{-1})	1.6009×10^{-31}
ψ	Rate of release of antigens	9.7669×10^{3}
τ_{A}	Antigen liberation to T-cell activation delay (days)	2.5494
σ	Natural elimination rate of antigens (days^{-1})	0.2905
a	Activation rate of T-cells (days^{-1})	2.8156×10^{-7}
r	*Activation/inactivation rates ratio	5
i_{c_4}	Dose of αCTLA4 per administration time	1.0865×10^{3}
ν	*Elimination rate of αCTLA4 (days^{-1})	0.1000
τ_{T}	Activated T-cell's time to reach the tumor (days)	0.2257
α_{T}	*Linear parameter for T-cells (Gy^{-1})	0.1000
β_{T}	*Quadratic parameter for T-cells (Gy^{-2})	0.0100
ι	Immune-mediated T-cells death rate (days^{-1})	2.2922×10^{-8}
η	Rate of natural elimination of T-cells (days^{-1})	0.2191
h	Rate of production of *blank* T-cells (days^{-1})	2.9738×10^{5}
V_{C}	*Volume of tumor cells (mm^3)	10^{-6}
V_{T}	*Volume of T-cells (mm^3)	2×10^{-7}

Table D.3: List of best-fitting parameters of the model to experimental data reported by Dewan *et al.* [59]. The LQL model (equation (1.7)) was used to account for tumor cell radiosensitivity. The symbol * indicates that the parameter value was fixed and not included in the optimization. Initial numbers/concentrations of variables not indicated in the table (C_{d}, $\hat{A}$, T_{a}, $\hat{T}_{\mathrm{a}}$, $\hat{T}_{\mathrm{b}}$, c_4, p_1) were set to zero. The parameter r is defined as $r = 1 + b/a$ [34].

Parameter	Description	Best-fitting value
C_0	*Initial number of tumor cells	100
T_0	Initial pool of *blank* T-cells	1.1679×10^{6}
λ_1	Proliferation rate of tumor cells (days^{-1})	0.1357
λ_2	Saturation of proliferation	3.3764×10^{-109}
α_{C}	Linear parameter for tumor cells (Gy^{-1})	0.0200
β_{C}	Quadratic parameter for tumor cells (Gy^{-1})	0.0022
ϕ	Elimination rate of doomed tumor cells (days^{-1})	0.0300
$\tau_{\text{d}1}$	*Mitotic delay (start) (days)	1
$\tau_{\text{d}2}$	*Mitotic delay (end) (days)	1.5000
p	Immune-mediated tumor cell death rate (days^{-1})	24.9382
q	Immune-mediated tumor cell death parameter	0.6886
s	Slope of the immune-mediated tumor death curve	5.7249
ρ	Rate of natural production of antigens (days^{-1})	1.3746×10^{-27}
ψ	Rate of release of antigens	3.4596×10^{7}
τ_{A}	Antigen liberation to T-cell activation delay (days)	1.0806
σ	Natural elimination rate of antigens (days^{-1})	0.1356
a	Activation rate of T-cells (days^{-1})	6.8010×10^{-12}
r	*Activation/inactivation rates ratio	5
i_{c_4}	Dose of αCTLA4 per administration time	7.4987
ν	*Elimination rate of αCTLA4 (days^{-1})	0.1000
τ_{T}	Activated T-cell's time to reach the tumor (days)	0.6077
α_{T}	*Linear parameter for T-cells (Gy^{-1})	0.100
β_{T}	*Quadratic parameter for T-cells (Gy^{-2})	0.0100
ι	Immune-mediated T-cells death rate (days^{-1})	6.2472×10^{-9}
η	Rate of natural elimination of T-cells (days^{-1})	0.5031
h	Rate of production of *blank* T-cells (days^{-1})	1.3358×10^{5}
V_{C}	*Volume of tumor cells (mm^3)	10^{-6}
V_{T}	*Volume of T-cells (mm^3)	2×10^{-7}
ine		

Table D.4: List of best-fitting parameters of the model to experimental data reported by Dewan *et al.* [59]. The LQ model (equation (1.1)) was used to account for tumor cell radiosensitivity, and limited T-cell infiltration was assumed for 20 Gy irradiation due to vascular damage (equation (3.13)). The symbol * indicates that the parameter value was fixed and not included in the optimization. Initial numbers/concentrations of variables not indicated in the table (C_{d}, $\hat{A}$, T_{a}, $\hat{T}_{\text{a}}$, $\hat{T}_{\text{b}}$, c_4, p_1) were set to zero. The parameter r is defined as $r = 1 + b/a$ [34].

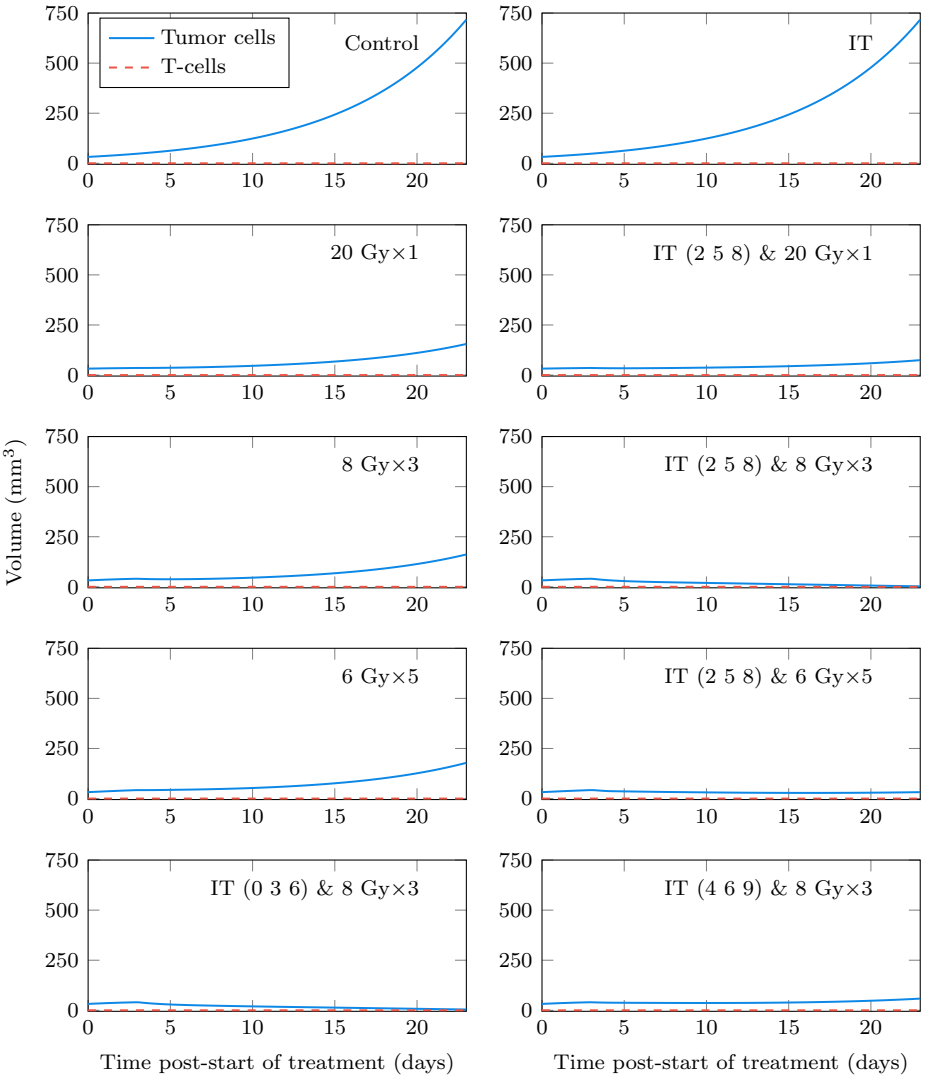

Figure D.1: Contribution of tumor cells and T-cells to tumor volumes in fits of the biomathematical model to experimental data of RIT with αCTLA4 reported by Dewan *et al.* [59]. These curves were obtained from fits reported in Figure 3.8, where the classical LQ model accounts for direct cell death, and the effect of vascular damage was taken into account. Tumor volumes are dominated by tumor cells, as expected. Numbers within parentheses indicate the delivery times of αCTLA4, if any.

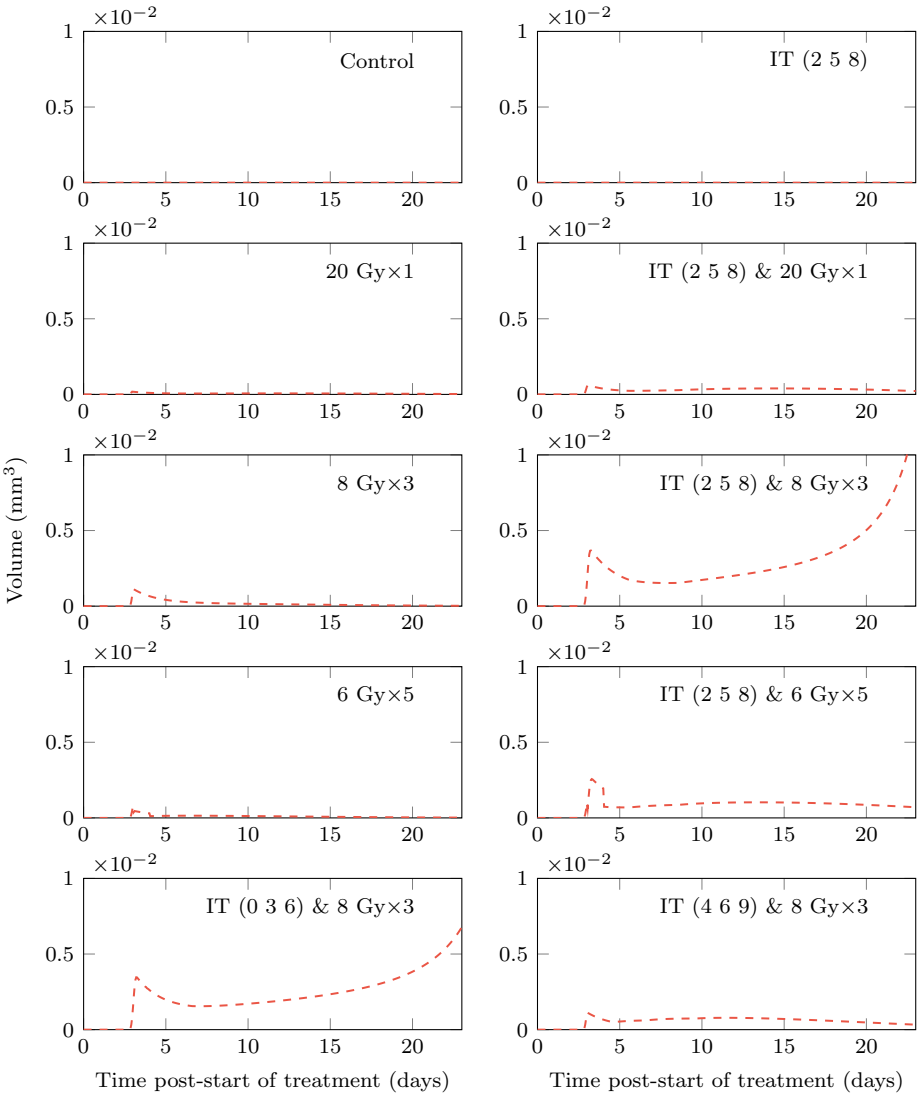

Figure D.2: Relative contribution of T-cells (dashed lines) to tumor volumes in fits of the biomathematical model to experimental data of RIT with αCTLA4 reported by Dewan *et al.* [59]. These curves were obtained from fits reported in Figure 3.8, where the classical LQ model accounts for direct cell death, and the effect of vascular damage was taken into account. Tumor volumes are dominated by tumor cells, and only when the tumor is close to remission, the T-cell fraction becomes large. Numbers within parentheses indicate the delivery times of αCTLA4, if any.

Appendix E

FLASH-RT tables and figures

	Diffenderfer *et al.* (a) & (b)	Zhu *et al.* (c)	Zhu *et al.* (d)
α_{ox} (Gy^{-1})	0.083	0.012	0.163
λ ($days^{-1}$)	0.134	0.120	0.068
K (mm^3)	4.800×10^{3}	7.861×10^{3}	0.877×10^{3}
ϕ ($days^{-1}$)	2.941×10^{-29}	1.921×10^{-11}	2.712×10^{-18}
V_0 (mm^3)	84.871	449.981 (control)	20.537
		359.417 (conv-RT)	
		255.000 (FLASH-RT)	

Table E.1: Best-fitting parameters for the tumor growth curves reported by Diffenderfer *et al.* [72] and Zhu *et al.* [140]. The characteristics of the experiments are summarized in Table 4.2 ((a) MH641905 12 Gy, (b) MH641905 18 Gy, (c) Py8119 9.5 Gy, (d) Py230 9.5 Gy).

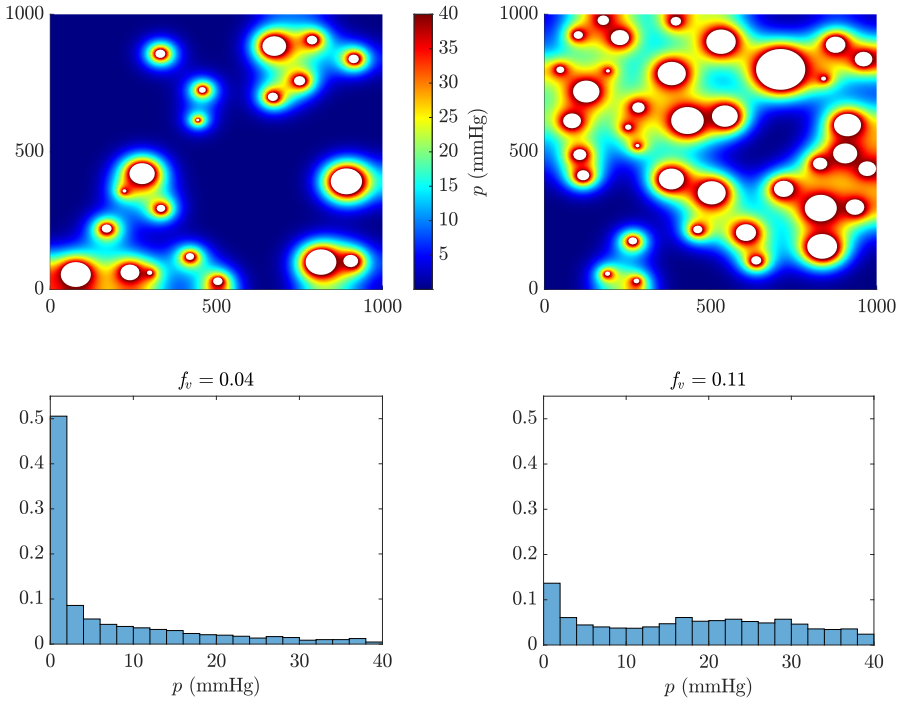

Figure E.1: Example of solutions to Problem 2.4 on a squared domain of 1 mm^2 [95] for two Vascular Fractions (VFs), f_v, leading to different oxygen distributions. The top panels show the spatial distribution of the oxygenation and capillaries, while the bottom panels show the associated histograms.

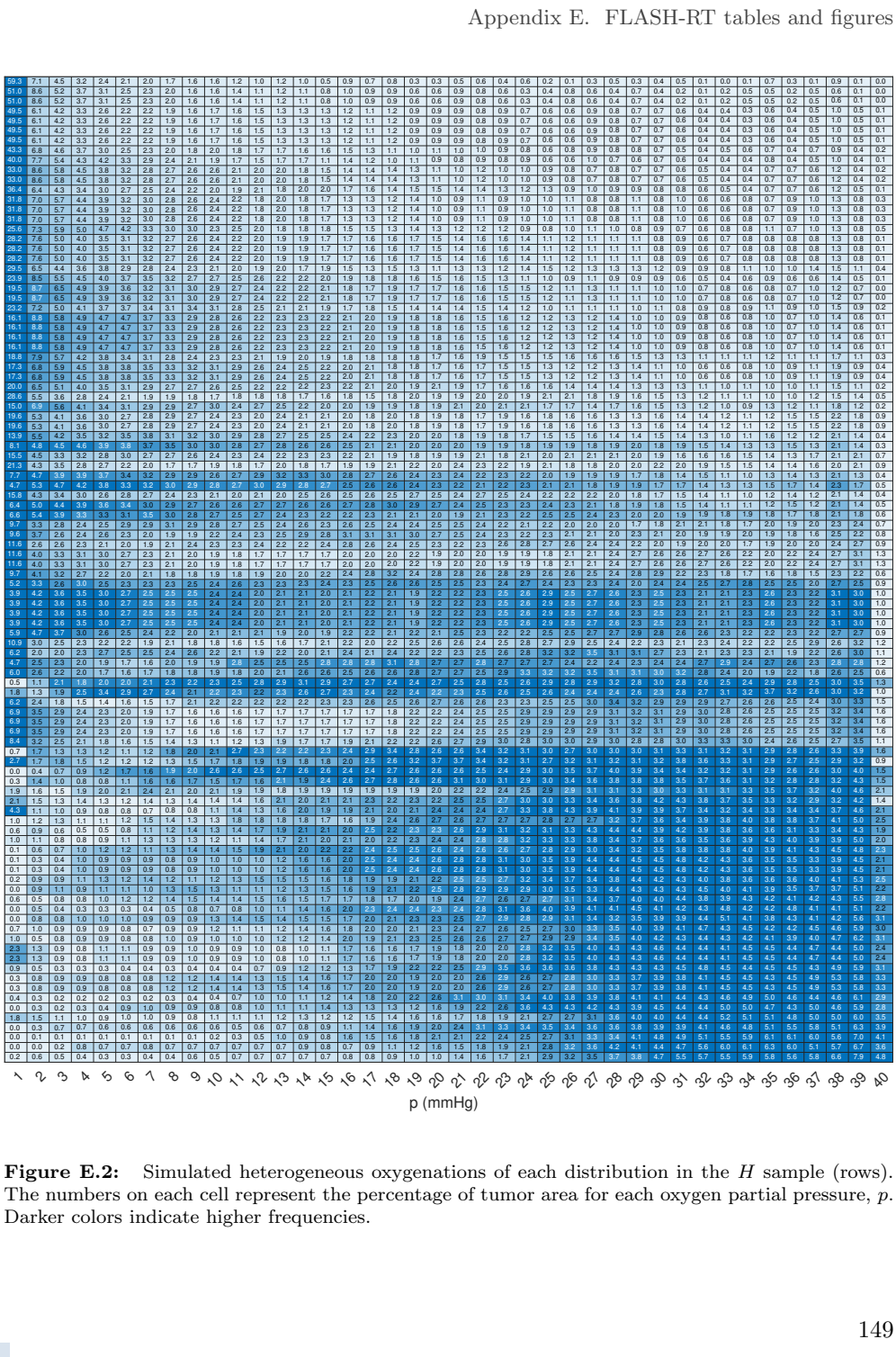

Figure E.2: Simulated heterogeneous oxygenations of each distribution in the H sample (rows). The numbers on each cell represent the percentage of tumor area for each oxygen partial pressure, p. Darker colors indicate higher frequencies.

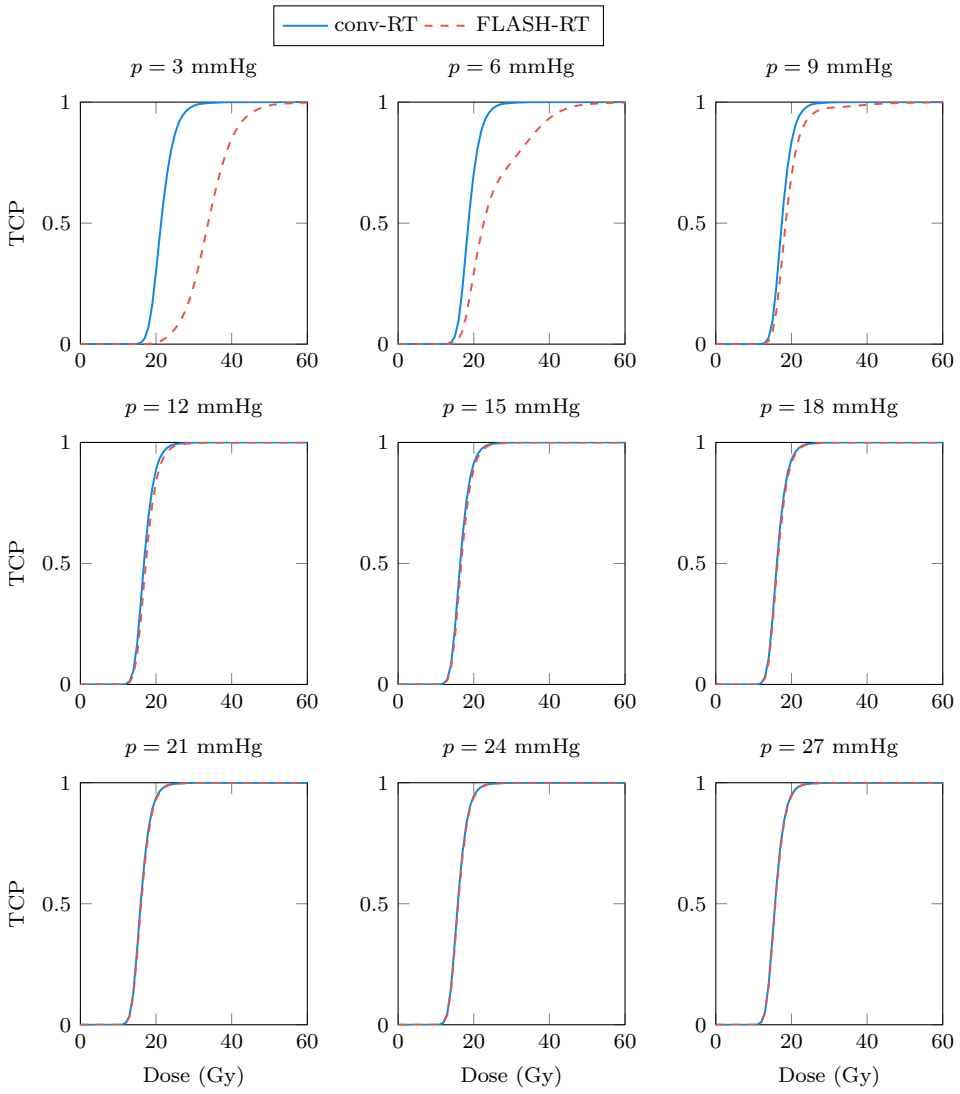

Figure E.3: Comparison of Tumor Control Probability (TCP)-dose curves between conv-RT and FLASH-RT for homogeneously oxygenated tumors with $\alpha_{ox}/\beta_{ox} = 10$ Gy and oxygen partial pressure ranging from 3 mmHg to 27 mmHg.

Appendix F

Copyright and permissions

- I. González-Crespo, A. Gómez-Caamaño, Ó. López Pouso, J. D. Fenwick, and J. Pardo-Montero, "A biomathematical model of tumor response to radioimmunotherapy with αPDL1 and αCTLA4," *IEEE/ACM Transactions on Computational Biology and Bioinformatics*, vol. 20, no. 2, pp. 808–21, 2023. DOI: 10.1109/TCBB.2022.3174454.

> The IEEE does not require individuals working on a thesis to obtain a formal reuse license. Copyright terms: https://www.ieee.org/publications/rights/copyright-policy.html.

- I. González-Crespo, F. Gómez, Ó. López Pouso, and J. Pardo-Montero, "An in-silico study of conventional and FLASH radiotherapy iso-effectiveness: potential impact of radiolytic oxygen depletion on tumor growth curves and tumor control probability," *Physics in Medicine & Biology*, vol. 69, p. 215016, 2024. DOI: 10.1088/1361-6560/ad8291.

> Original content from this work may be used under the terms of the Creative Commons Attribution 4.0 license (CC BY 4.0). Copyright terms: https://creativecommons.org/licenses/by/4.0/.

- BioRender Basic License Terms.

> BioRender does not require a license to include its content in: an unpublished thesis or dissertation; presentations which include Completed Graphics that are solely for academic or educational purposes or personal use cases. If the thesis is going to be uploaded to a University database or library, BioRender does not consider this as a published thesis. Copyright terms: https://www.biorender.com/basic-license.

A Biomathematical Model of Tumor Response to Radioimmunotherapy With αPDL1 and αCTLA4

Author: Isabel González-Crespo

Publication: IEEE/ACM Transactions on Computational Biology and Bioinformatics

Publisher: IEEE

Date: 01 March-April 2023

Thesis / Dissertation Reuse

The IEEE does not require individuals working on a thesis to obtain a formal reuse license, however, you may print out this statement to be used as a permission grant:

Requirements to be followed when using any portion (e.g., figure, graph, table, or textual material) of an IEEE copyrighted paper in a thesis:

1) In the case of textual material (e.g., using short quotes or referring to the work within these papers) users must give full credit to the original source (author, paper, publication) followed by the IEEE copyright line © 2011 IEEE.
2) In the case of illustrations or tabular material, we require that the copyright line © [Year of original publication] IEEE appear prominently with each reprinted figure and/or table.
3) If a substantial portion of the original paper is to be used, and if you are not the senior author, also obtain the senior author's approval.

Requirements to be followed when using an entire IEEE copyrighted paper in a thesis:

1) The following IEEE copyright/ credit notice should be placed prominently in the references: © [year of original publication] IEEE. Reprinted, with permission, from [author names, paper title, IEEE publication title, and month/year of publication]
2) Only the accepted version of an IEEE copyrighted paper can be used when posting the paper or your thesis on-line.
3) In placing the thesis on the author's university website, please display the following message in a prominent place on the website: In reference to IEEE copyrighted material which is used with permission in this thesis, the IEEE does not endorse any of [university/educational entity's name goes here]'s products or services. Internal or personal use of this material is permitted. If interested in reprinting/republishing IEEE copyrighted material for advertising or promotional purposes or for creating new collective works for resale or redistribution, please go to http://www.ieee.org/publications_standards/publications/rights/rights_link.html to learn how to obtain a License from RightsLink.

If applicable, University Microfilms and/or ProQuest Library, or the Archives of Canada may supply single copies of the dissertation.

BACK CLOSE WINDOW

Radiotherapy is a cancer treatment that consists of irradiating tumors to eliminate tumor cells while maintaining the dose on neighbor organs/tissues within tolerance levels. Mathematical models predict the efficacy and toxicity of radiotherapy, assisting in designing more effective and less toxic treatments. This thesis aims to design mathematical models of tumor response to advanced radiotherapies by using ordinary (ODEs), partial (PDEs), delay (DDEs), and impulsive differential equations (IDEs). The focus is on radioimmunotherapy and FLASH radiotherapy, which involve biological mechanisms that require the development of novel mathematical models, as the existing ones for conventional radiotherapy are not directly applicable.